PhD Dissertation

International Doctorate School in Information and Communication Technologies

DISI - University of Trento

Landslide Monitoring Using Radar Interferometry in the Alps

Mehdi Darvishi

Advisor:
Prof. Lorenzo Bruzzone
University of Trento

Co-advisor:
Dr. Giovanni Cuozzo, Dr. Romy Schlögel, Dr. Benni Thiebes
Institute for Earth Observation, Eurac Research

2019

Abstract

Active natural processes, such as landslides, that can induce damages and casualties, recurrently affect mountainous areas. In order to reduce the risks, the careful assessment and monitoring of landslides is highly needed. Interferometric Synthetic Aperture Radar (InSAR) is a powerful tool that can extract useful information to monitor natural hazards. Over the past two decades, several studies have demonstrated the potential of synthetic aperture radar interferometry for detecting and quantifying land surface deformation. Despite the advantages of InSAR methods for quantifying landslide deformation, some limitations remain. The temporal and spatial decorrelation, the presence of atmospheric artifacts, the 1-D Line Of Sight (LOS) observation restriction, the possible high velocity rate and the multi-directional movement properties make it difficult to monitor accurately complex landslides in areas covered by vegetation. Therefore, complementary and integrated approaches, such as offset tracking-based techniques, and sophisticated atmospheric artifacts estimation are needed to overcome these limitations for monitoring ground surface deformations. These critical issues are particularly challenging in mountain environments, due to the SAR properties, the stronger spatial variations of the local atmospheric conditions and the scattering characteristics of the ground surface, leading to spatial and temporal decorrelation of the SAR signal. Hence, the performance evaluation of the offset tracking and atmospheric corrections techniques is important in order to assess their potentials, robustness and limitations. In this thesis, we aim at improving estimation accuracy of offset tracking and InSAR atmospheric phase delay estimation. To this end, the Corvara landslide, located in the Alpine region of South Tyrol, is used as a pilot site to implement and test the offset tracking and atmospheric correction techniques. This area is monitored with GPS periodic campaigns and permanent stations and over there a set of corner reflectors have been installed. This thesis aims at improving accuracy of offset tracking and phase delay estimation of SAR images through the following two approaches:

i) An offset tracking feature-based approach for the velocity estimation of the X-band Corner Reflectors (CRs) installed on the complex and vegetated landslide. The approach is based on the using the combination of the corner and blob-based detectors and descriptors driven from computer vision filed. The aforementioned algorithms are applied to COSMO-SkyMed data to estimate the high velocity rate and non-LOS movement of the CRs and the results are validated by GPS measurements executed closer to the satellite acquisitions.

ii) An approach for estimation and improvement of InSAR atmospheric phase delay correction using numerical weather data. The approach is based on the use of the new-released ERA5 data to estimate turbulent stratified delays on the Sentinel-1 data. The performance of phase and weather-based data are analyzed and validated using the GPS and external reference data.

For each of the above-mentioned topics a comprehensive state of the art is addressed, the limitations and challenges of existing methods are mentioned and the proposed solutions to the considered problems are described in detail. Experimental results conducted using real SAR data are provided in order to present and confirm the validity and accuracy of each one of the used methods.

Keywords:
Landslide, corner reflector, InSAR, Persistent Scatterer Interferometry (PSI), Multi-Aperture Interferometry (MAI), offset tracking, computer vision, SAR, remote sensing, Phase and weather-based models, atmospheric correction, GPS, phase delay, Small BAseline Subset (SBAS)

Acknowledgments

First, I would like to thank Prof. Lorenzo Bruzzone for the privilege of having him as my supervisor during these three years.

I would like to acknowledge the kind and constant support of my co-supervisors at the EURAC including Dr. Giovanni Cuozzo, Dr. Romy Schlögel and Dr. Benni Thiebes.

I would like to thank the administrative members of the EURAC for their management and financial support involving Dr. Stefan Schneiderbauer, Dr. Claudia Notarnicola and Dr. Marc Zebisch.

I would also like to thank everyone who was involved in fieldwork, i.e., B. Thiebes, R. Schlögel, Christian Kofler and M. Mulas for the organization of GPS surveys/data processing, and V. Mair for the design of the study and the coordination of the research and Nuccio Di Sclafani from Bolzano province (South Tyrolean POsitioning (STPOS)) for providing the raw GPS stations data.

Finally, massive thank you to everyone who has been a part of my PhD, and helped to make this happen.

Contents

List of Figures

List of Tables

List of Symbols

B	Baseline separation
B_c	Chirp bandwidth
B_{perp}	Perpendicular baseline
B_s	Sub-bandwidth
c	Velocity of light (in a vacuum) 299.792x$\times10^6$ ms^{-1}
cc	Coherence threshold
D_A	Normalized amplitude dispersion
e	Partial pressure of water vapor
F	Fourier Transformation
f	Frequency
f_0	Radar operating (or carrier) frequency
f_{dc}	Doppler frequency
f_s	Sampling frequency
h	Topographic elevation
h_0	An altitude where phase delays converged to zero
I	Matrix of the image
K_a	Command band filter
K_1	Empirical coefficient $K_1=77.6$
K_2	Empirical coefficient $K_2=23.2$
K_3	Empirical coefficient $K_3=3.75\times10_5$
l_a	Antenna length in the azimuth direction
L_a	Length of synthetic antenna (aperture)
m	Geopotential
N	Number of independent samples
N_{hydro}	Hydrostatic or dry delay
N_{wet}	Wet delay
N_{iono}	Ionospheric delay
N_{liquid}	Liquid delay
N_l	Number of looks
N_r	Multi-looking factor in range direction
N_a	Multi-looking factor in azimuth direction
n	Normalized squint
n_e	Electron number density per cubic meter
r_r	Spatial slant resolution
r_g	Ground range resolution
r_1	Slant rage distance corresponding to the first pass/acquisition
r_2	Slant rage distance corresponding to the second pass/acquisition
P	Pressure
P_a	A pair of respective fields in the images
PDE	Phase Delay Estimation
PS	Pixel spacing
$P_{x,y}$	Error of the extracted offsets
PhU	Phase unwrapping

sp	Pixel size of the SAR image
SCR	Signal to Clutter Ratio
S_{trop}	One-way tropospheric delay
sgn	Sign function
t	Time
t_o	Time zero
U_n	Northern component
U_u	Vertical component
U_e	Eastern component
T	Temperature
W	Liquid water content
W_s	Adaptive filtering
ZTD	Zenith total delay
ZWD	Zenith wet delay
ZHD	Zenith hydrostatic delay
Θ	Beamwidth of antenna
θ_1	Incident angle corresponding to the first pass/acquisition
θ_2	Incident angle corresponding to the second pass/acquisition
λ	Wavelength
$\lambda_1, \lambda_2, \lambda_{th}$	Eigenvalues
γ	Coherence
γ_t	Total correlation
τ	Width of radar ranging pulse
$\Delta\varphi$	Phase differential
Δx	Cross track displacement
Δr	Along track displacement
$\Delta\beta$	Antenna angular beam width
ΔT	Time interval of two successive acquisitions
φ_{base}	Baseline phase
φ_{topo}	Topography phase
φ_{dis}	Displacement phase
φ_{atm}	Atmosphere phase
φ_{noise}	Noise phase
φ_{trop}	Two-ways tropospheric phase delay
φ_u	Upper sub-band differential
φ	Phase
φ_l	Lower sub-band differential
φ_{SD}	Differential spectral diversity
$\varphi_{InSAR,\,f}$	Forward interferometric phase
$\varphi_{InSAR,\,b}$	Backward interferometric phase
σ_A	Standard deviation
μ_A	Mean amplitude
ψ	Squint angle
α	Baseline orientation
α_h	Azimuthal angle
α_d	Power law decay component
$H(x,\sigma)$	Hessian matrix

Chapter 1

1. INTRODUCTION

1.1 Introduction and Motivations of the Thesis

Natural disasters induced by gravitational mass movements are widespread phenomena of various magnitude caused by geological and climatic conditions or induced by anthropogenic factors [1]. Slope displacement can be detected and monitored by several Earth observation techniques [2], while the selection of an adequate monitoring concept depends on the scope of the study, the type and scale of phenomena, the data available, and the skills of the investigators [3][4]. The kinematics and spatial and temporal evolution of landslides using InSAR-based techniques have been analyzed in a large number of scientific studies [5][6][7][8]. New generations of satellites, such as the Copernicus Sentinel-1 (S1), open up new perspectives for continuous ground surface monitoring, being characterized by enhancements in terms of revisit time, coverage, timeliness, and reliability of service [9]. Indeed, the C-band S1 synthetic aperture radar (SAR) instrument is specifically designed to carry out interferometric analyses over land [10], and recent studies have confirmed that S1 data allows analyzing Earth's surface displacements using differential SAR interferometry (DInSAR) techniques [11][12][13]. DInSAR has the capability to precisely monitor surface displacements over time (temporal sampling rate up to 6 days for Sentinel-1A/B) with a wide coverage in a labour-saving, time-, and cost-efficient manner [14].

Despite the capabilities of DInSAR techniques, those suffer several drawbacks including spatial and temporal decorrelations [15], a possible inaccurate estimation of the phase ambiguity in the unwrapping phase step [16], atmospheric artifacts [17] and the capability to only measure 1D displacement components limited to the line of sight (LOS) direction of the satellite path. Regarding the latter one, should note that the design and the launch of non-polar SAR space borne satellites cannot be currently achieved. Therefore, numerous attempts have been done to develop new techniques to extract the along-track components using available SAR data. From this perspective, InSAR techniques generally are divided into two groups: along-track and LOS-based SAR processing techniques. For this purpose, several advanced DInSAR methods can be used to extract 3D displacement components from LOS-based detection techniques such as permanent scatterer and Small BAseline Subset, and along-track-based techniques multi-aperture interferometry (MAI) and pixel offset tracking. The methods based on time series analysis of SAR data are also characterized by the separation between atmospheric delay and deformation phase. All decomposition methods that isolate the phase of atmospheric delay assume that the atmospheric delay is uncorrelated in time, and therefore, the expected value of the differential atmospheric delay is zero.

Different techniques can be used to reduce the effect of atmospheric delay on the time series stack, such as averaging of various interferograms [17] [18][19], separating atmospheric phase in the single master on the stack [20], stochastic models [21] and a sequence of high-pass and low-pass filters in time and space [22][23]. To benefit from the advantages of the last two ones, a combination of both methods can be used [24]. In cases of sharp topography, the assumption of no correlation between atmospheric delay and time may not be valid. In this case, in addition to the atmospheric delay, heterogeneity in pressure, temperature and humidity will affect the consecutive SAR data [15] and can lead to the temporal decorrelation. Different approaches such as using numerical weather models [25] can be used to estimate the vertical stratification and mitigate its effects on the interferograms.

1.2 Contributions of the Thesis

On the basis of the analysis of the problems related to the monitoring of complex and vegetated landslides in mountainous areas, this thesis generally focuses on how phase and intensity-based offset tracking and InSAR atmospheric correction can contribute in the estimation of the related terrain deformation.
More in details, the two topics are analyzed as follows:

- Comprehensive assessment of the literature on offset estimation methods;
- Definition of hybrid techniques based on the combination of different feature-based and area-based matching algorithms for improving accuracy in offset estimation in SAR data in vegetated terrains characterized by high velocity rates;
- Comprehensive performance evaluation of the InSAR atmospheric corrections methods;
- Improvement of InSAR phase delay estimation using the new-released numerical weather model ERA5.

In the next sub-sections the main objectives and novelties are more elaborated.

Accuracy improvement of offset estimation using computer vision-driven techniques applied to SAR data

We analyzed phase and intensity-based offset-tracking techniques to improve the accuracy of offset estimation (related to movement of the CRs on the area of study). To this end, the goal is how we can overcome or mitigate the geometrical distortions caused by the tilting of the CRs installed in the area characterized by fast movements on the SAR data, which are the main problems in offset estimation. In the phase-based part, PSI and MAI techniques, and in in the feature-based part, area and feature-based matching algorithms are used for extracting

LOS and azimuthal displacement components. In the area-based algorithms section, phase and orientation correlation in the frequency domain, and intensity-based cross correlation in the spatial domain are apples to SAR data. In the feature-based algorithms section, the local feature detectors and descriptors in the spatial domain are applied. Four well-known area-based and five feature-based matching algorithms (taken from the computer vision) are applied to 16 X-band corner reflectors and the results are validated with ground GPS measurements. The accuracy of the amplitude offset tracking technique have been empirically reported by researcher between about 1/10 to 1/30 of the pixel size for typical SAR systems, corresponding to 10% and 3.3% of the pixel size of CSK data. Our results presented that offset accuracy from 0% of the pixel size (i.e., correct estimation) using a combination of the feature-based algorithms up to 1% of the pixel size using the phase correlation.

Performance evaluation of phase and numerical weather models in InSAR atmospheric correction

Performances of phase and numerical weather models in InSAR atmospheric correction are evaluated in order to assess their potentials, robustness and limitations. This section analyzes and evaluates the performance of four numerical weather models, two phase-based models (i.e., linear and non-liner) and multispectral data to estimate phase delay using Sentinel-1A/B data over the Corvara landslide. The GPS data and external product are used to validate the results. Three statistical parameters and two different metrics are utilized as performance indicators to evaluate the model’s performance for the zenith and InSAR phase delay estimation. We generally found that ERA5 outperformed among the current and conventional models with a phase standard deviation reduction of 77.7%, correlation coefficient of 0.86 and a less significant error in the velocity estimation of the landslide.

1.3 Structure of the Thesis

The thesis is organized in six chapters. The current chapter addressed the motivations of the research and highlighted the objectives and the main contributions.

Chapter 2 provides the fundamentals about the basic and state of the art of the offset tracking techniques, and SAR, InSAR, multi-temporal DInSAR and InSAR atmospheric correction methods.

Chapter 3 starts with a brief presentation of the test site, the equipment installed and the datasets, as well as some metrics used for the quality assessment. The method section illustrates the techniques, including PSI, MAI, and phase and intensity-based sub-pixel offset tracking, used in the study and some data processing tasks. The effectiveness of the methods has been validated on COSMO-SkyMed data over the set of X-band CRs. The results of

InSAR and offset tracking techniques applied to the CRs are presented in the following section. Finally, the performance assessment results, downsides and advantages of each technique are addressed in the discussion and conclusion sections.

Chapter 4 deals with the assessment of the performance of 2D and 3D phase unwrapping methods in a vegetated landslide and evaluates the application of DInSAR using Sentinel-1 data and DGNSS to continuously monitor the Corvara landslide. The ground-based and remote sensing data as well as the methodological workflow are also presented. Afterwards, DInSAR results are analyzed and compared with DGNSS data in order to discuss the potential and limitations of the new S1 mission for the continuous spatial monitoring of complex and vegetated landslides.

Chapter 5 presents the use of phase-based models, including linear and non-linear (power law) models, Numerical Weather Models (NWM), multi-spectral data and GPS data, to estimate phase delay on Sentinel-1A/B data and evaluate their performance. Three steps are carried out: 1) cross-comparison between the ZTD, ZWD and TWD derived by GPS with its counterparts obtained by NWM-based models, 2) cross-comparison between the InSAR tropospheric phase delays estimated by phase and NWM-based models in a regional scale and 3) cross-comparison between the GPS stations velocity and the velocity corrected by the phase and NWM-based models in a local scale (i.e., the active Corvara landslide). For this purpose, in addition to the GPS data, we used the GACOS product as reference to cross validate the results in all steps.

Finally, chapter 6 provides the conclusion of the results of the chapters 3, 4 and 5 and a brief summary on the possible further development.

Chapter 2

2. FUNDAMENTALS ON SAR AND OFFSET TRACKING TECHNIQUES

The aim of this chapter is to provide the readers with the basic knowledge about synthetic aperture radars and the state of the art on InSAR and offset tracking techniques on SAR images. The chapter is organized in three sections. In the first section, the basic principles of SAR, InSAR, multi-temporal DInSAR (including PSI and SBAS) and atmospheric correction are reviewed. In the second section, InSAR-based offset tracking methods including split-bandwidth-based techniques (i.e., Spectral Diversity and Multiple Aperture Interferometry) and offset tracking-based techniques are described. In the last section, a brief summary of InSAR atmospheric correction methods are discussed.

2.1 Synthetic Aperture Radar (SAR) system

Radar satellite systems utilize a side-looking antenna to illuminate a footprint on Earth surface (swath) using signal pulses (see Figure 2.1). The amplitude of the pulse is constant while its frequency is linearly varied in time (chirp pulse) (see Figure 2.2).

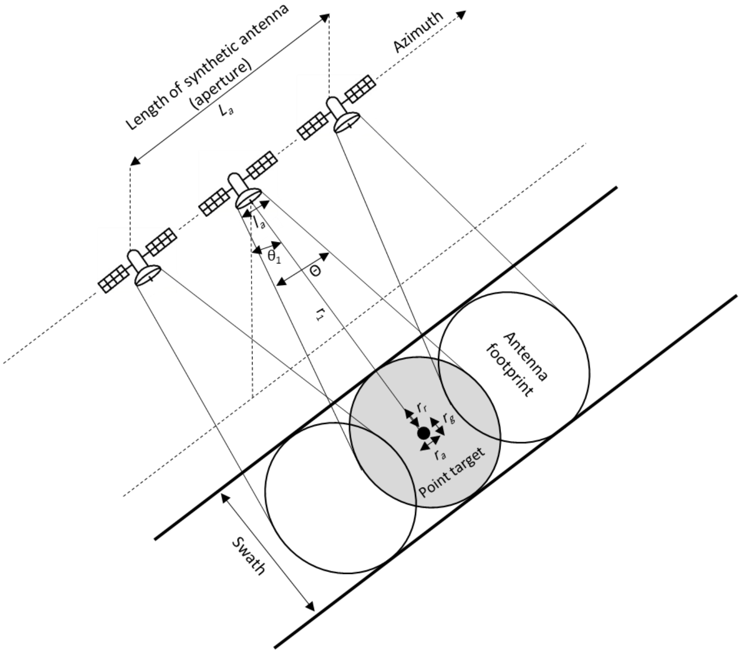

Figure 2.1 : SAR geometry imaging

The transmitted chirped pulses are repeated at a rate called Pulse Repetition Frequency (PRF):

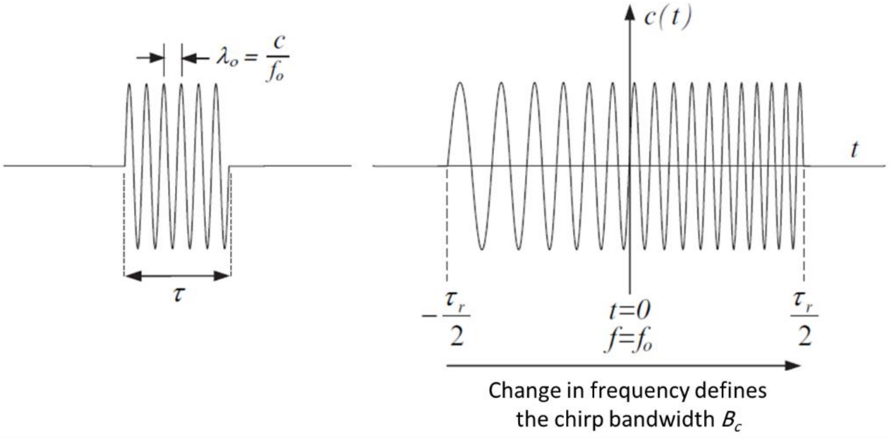

Figure 2.2 : A simple sinusoidal pulse (left) and chirped pulse (right) [26].

According to Figure 2.1and Figure 2.2, the slant range resolution (r_r) and ground range resolution (r_g) of a real SAR system are defined as follows:

$$r_a = \frac{c}{2B_c} \tag{2.1}$$

$$r_g = \frac{c}{2B_c \sin\theta_1} \tag{2.2}$$

Where B_c and θ are bandwidth chirp and incident angle, respectively. From theory of antenna, the angular beamwidth of an antenna (Θ) with a length of l_a along the azimuth direction is defined as:

$$\Theta_a = \frac{\lambda}{l_a} \tag{2.3}$$

Thus, the azimuthal spatial resolution considering the footprint of antenna beam is given by:

$$r_a = \frac{\lambda}{l_a} r_1 \tag{2.4}$$

where r_1 is the slant range distance (i.e., the distance from satellite to the ground target point) which is a height-dependent variable. As one can see from (2.4), a larger antenna can provide a better azimuthal resolution. In the SAR approach, a larger antenna is synthesized by using signal processing techniques so that the azimuthal resolution is no longer either height or range-dependent and only depends on antenna length. The maximum azimuth resolution obtaines with a synthetic antenna (aperture) is given by:

$$r_a = \frac{l_a}{2} \tag{2.5}$$

Therefore, contrary to real antenna aperture where the azimuth resolution has an inverse dependence on the antenna length (see (2.4)). In a SAR system (2.5), the azimuth resolution directly depends on the physical length of antenna. This means that a fine azimuth resolution can be achieved by using a short antenna in a SAR system [26].

2.2 Synthetic aperture radar interferometry (InSAR)

InSAR relays on multiplicative interference, which can be used either for DEM or deformation extraction. Two SAR images (called master and slave) usually captured at two different times and from a different position are needed to make an interferogram. After the co-registration step, the interferometric phase is obtained by multiplying the master with the complex conjugate of the co-registered slave. The resulted interferometric phase is attributed to the different distances between satellite and target in the Line Of Sight (LOS) direction (see Figure 2.3):

$$\Delta\varphi = \frac{4\pi\Delta r_r}{\lambda} \tag{2.6}$$

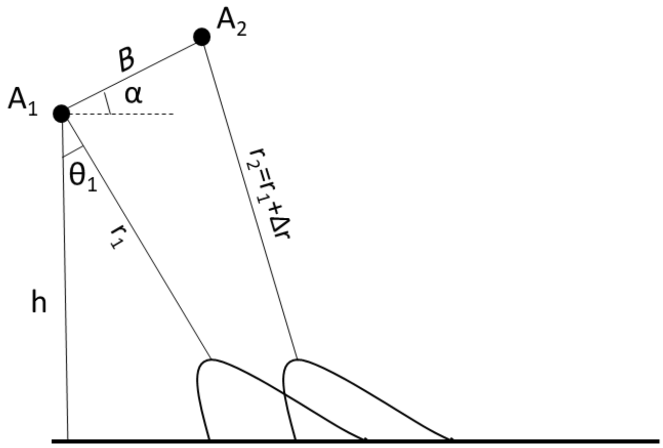

Figure 2.3 : Repeat pass interferometry. The relationship between phase difference and shift in slant range.

where r_1 and r_2 indicate the range between the SAR platform and ground object on the earth and B refers to the separation baseline between A_1 and A_2. Interferometric phase is composed of the different phase contributions as follows:

$$\Delta\varphi = \varphi_{base} + \varphi_{topo} + \varphi_{disp} + \varphi_{atm} + \varphi_{noise} \tag{2.7}$$

$$\varphi_{base} + \varphi_{topo} = -\frac{4\pi}{\lambda} B_{perp} \sin(\theta - \alpha) \tag{2.8}$$

where φ_{base} is the phase induced by the baseline between the location of two platforms, φ_{topo} is due to topography, φ_{disp} is due to ground displacement, φ_{atm} is due to atmospheric phase delay, and φ_{noise} is related to external and internal noises sources such as ionospheric and system noise. Since the interferometric phase is wrapped into 2π, to achieve a continuous deformation map the differential phase between adjacent pixels must be integrated using a procedure called phase unwrapping. Conventional InSAR encounters several limitations such as temporal and geometric decorrelation [27] and phase variability due to the atmospheric phase screen mainly correlated with topography [15]. Multi-temporal InSAR can potentially mitigate or overcome the aforementioned drawbacks.

Displacement component derived by InSAR can be decomposed and projected to the geographical components on the Earth. The sensitivity decomposition can be obtained using unit vector, as a function of range and azimuth changes for LOS (cross-track) [15] and along-track deformation, as follows:

$$U_{Cross\,track\,(LOS)} = [U_u, U_n, U_e]^T \left[\cos(\theta_1), \sin(\theta_1).\sin(\alpha_h), -\sin(\theta_1).\cos(\alpha_h)\right] \tag{2.9}$$

$$U_{Along\,track} = [0, U_n, U_e]^T \left[0, -\cos(\alpha_h), -\sin(\alpha_h)\right] \tag{2.10}$$

The sensitivity decomposition of LOS deformation obtained by substituting θ_1 and α_h in (2.9), is $[0.697, -0.185, 0.692][U_u, U_n, U_e]^T$.

2.3 Multi-temporal DInSAR

2.3.1 Persistent scatterer Interferometry (PSI)

PSI as an extension to the conventional InSAR has been developed to address decorrelation problems and atmospheric delays using multiple SAR acquisitions to estimate spatial-temporal characteristics of a surface deformation[28]. Generally, PSI technique relies on the main following steps: 1) interferogram generation, 2) Computation of the differential interferograms using a digital elevation model (DEM), 3) preliminary estimation of PS pixels, which can be based on phase stability, amplitude and correlation, at a coarse grid, and 4) Atmospheric Phase Screen (APS) removal. In the third step, we need to identify the pixels whose phase information is less contaminated by noise as much as possible. Changes in the singles scatterers contributing to a pixel over time (temporal decorrelation) and viewing angles (geometric decorrelation) lead to phase and amplitude variation of the pixel. Hence, two types of pixels types could be defined: (1) the pixels with scattering objects that dominate the radar backscattering in comparison to the background (i.e. high coherence over time), named permanent scatterers (PS), (2) pixels with strong backscattering coming from small scattering objects, named distributed scatterer (DS) (see Figure 2.4). If the phase of a pixel appears as a point scatterer on the image (a stable phase history over time), the decorrelation problem is mitigated. For example, manmade structures such building in urban areas or tree trunks in natural terrain produce a point target response in SAR images that are potential measurement points in the PSI technique.

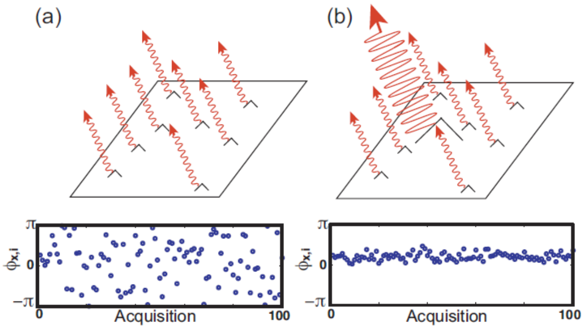

Figure 2.4 : Phase simulation for (a) a distributed scatterer pixel and (b) a persistent scatterer [29].

To select the pixels with a high phase stability, two selection approaches exist, including a-priori pixel and a-posteriori pixel selection. The main purpose of the a-priori pixel approach is to reduce the negative effect of the pixels at low coherence as well as the computational load. PS selection can be based on either the phase or the amplitude information. The main methods that are generally used to PS pixel selection are: 1) normalized amplitude dispersion (D_A) (2.11) [13], 2) amplitude thresholding [14], 3) signal-to-clutter ratio [15] and 4) supervised selection [16] (see Table 2.1). The normalized amplitude dispersion (D_A) is defined (Figure 2.5):

$$D_A = \frac{\sigma_A}{\mu_A} \tag{2.11}$$

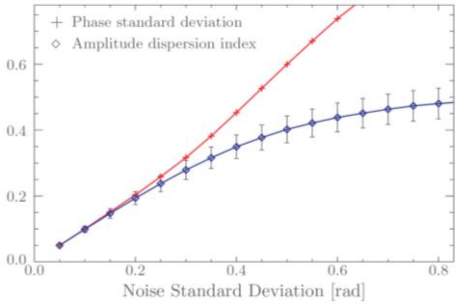

Figure 2.5 : Numerical simulation for the amplitude dispersion index [28].

where σ_A and μ_A are standard deviation and mean amplitude, respectively. In PSI technique, consistency of the amplitude is mainly used to estimate the phase stability in the stack. Therefore, a radiometric calibration of Single Look Complex (SLC) data, which are represented by a complex (I and Q) value containing both amplitude and phase information, should be carefully applied to the data. The reliability of the selected PS candidates will be specified using the a-posteriori pixel selection approach in order to remove unreliable pixels. Different quality indicators are used to select the PS, such as local ensemble coherence or variance factor and can be used along with a testing procedure based on the various key parameter such as phase ambiguities [17].

Table 2.1: Summary of main methods for the pixel selection

Methods	A-priori selection	A-posteriori selection	Atmospheric signal
Stacking [18] [19] [20]	Coherence	-	Averaging
Phase gradient approach [27]	Coherence and phase gradient	-	Weighted averaging
Permanent Scatterers [13] [21]	Amplitude dispersion	Temporal coherence	High-pass/low-pass filtering
SBAS [23]	Mean spatial coherence	-	High-pass/low-pass filtering
STUN [22] [28]	Amplitude dispersion/SCR	Parameter testing	Stochastic model
StaMPS [25]	Amplitude dispersion	PS probability (temporal coherence+ amplitude dispersion)	High-pass/low-pass filtering (adapted)
SqueeSAR [29]	Statistical homogeneity Test	Temporal coherence	High-pass/low-pass filtering

Generally, the initial pixel selection is performed within grid cells for reducing the computational load and a network is then created to link the PS pixels for displacement and DEM errors estimation, and APS residual removal (Figure 2.6). The pixels are selected as a PS pixel if the amplitude dispersion is below a threshold, typically between 0.25 and 0.4 [30][28]. The PS pixels density must be at least ~3 PS/km2, since otherwise the atmospheric signal cannot reliably be interpolated [30].

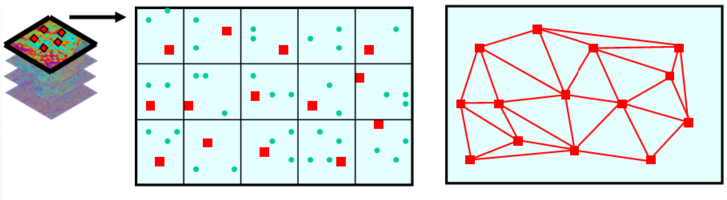

Figure 2.6 : Pixel selection and construct a network. On the left side, the best point-like scatterer (the red squares) is selected in each grid cells in the initial pixel selection step. On the right side, a network is created to estimate the displacement and DEM errors. The difference between nearby pixels also mitigates APS.

At the end, to isolate the deformational signal from interferogram, the atmospheric phase is removed and the uncorrelated component of the DEM error (Δh) is obtained and removed at the inversion step through the following equation:

$$\Delta\varphi = \frac{4\pi B_{perp} \sin(\theta_1)\Delta h}{\lambda} \tag{2.12}$$

B_{perp} indicates the perpendicular baseline. Indeed, pixel selection based on the phase stability provide more PSs than amplitude-based PSs selection. In the atmospheric phase removal step, as atmospheric signal is uncorrelated in time and correlated in space, hence, this can be isolated from the other components of the residual phase by low-pass filtering in the spatial domain and high-pass filtering in the temporal domain. The filtering can be performed on wrapped complex residual signal separately to estimate low wavelengths without need for unwrapping [20]. After the low wavelength part of the atmospheric delays, it is interpolated at the original resolution of the differential interferograms and the interpolated atmospheric delays are subtracted from the differential interferograms at full resolution. The Kriging interpolation can also be utilized instead of using moving averaging window in the interpolation step [30].

Instead of using a model of deformation in time, which is used in conventional PSI, StaMPS uses the spatial correlation to estimate displacement parameters. PSI technique, in its first versions, identifies PS pixels whose phase history match a pre-defined model (often a linear model). Thus, a priori knowledge of how displacement varies in time is essential for a correct displacement estimation. When a temporal pattern of deformation is not known a-priori, which is the case for natural terrain such as landslides and volcanos, specific techniques (e.g., StaMPS), have been developed. In StaMPS, first for the initial PS pixel selection, a high threshold of amplitude dispersion is applied. Then, spatial correlation of phase measurements, rather than a functional temporal model, is used to identify PS pixels. This is applicable in areas undergoing non-steady deformation with no prior knowledge of the variations in deformation rate. This is performed using low-pass filtering in the space domain.

In this way, the low frequency components of the predefined patches (by user), including correlated spatially of the first four phase contributions of the interferogram, will be passed and the noise component is filtered (see (2.7) and Table 2.2).

Table 2.2 : Spatial and temporal correlation status of the phase contributions in Eq. 2, where ↓ and ↑ symbols refer to low and high frequency, respectively [29].

Phase contribution	**Correlation**	**Frequency**
Deformation	Spatial ↓	Temporal ↓
Atmospheric phase screen	Spatial ↓	Temporal ↑
Orbit errors	Spatial ↓	Temporal ↑
Topo correction error	Spatial ↑	α Baseline ↑
Uncorrelated noise terms	Spatial ↑	Temporal ↑

Subsequently, the contribution of each pixel is weighted based on its estimated temporal coherence and the previous processing is iterated.

2.3.2 Small BAseline Subset (SBAS)

SBAS relies on the definition of a threshold on temporal and spatial baseline values. A shorter spatial baseline, which is characterized by a small orbital separation (baseline), can considerably reduce the spatial decorrelation phenomena. Let us assume N+1 SAR images corresponding to the same area and acquired between time t_0 to t_N exist leading to M interferograms with the following condition:

$$(\frac{N+1}{2} \leq M \leq N\left(\frac{N+1}{2}\right)) \tag{2.13}$$

For a given interferogram between times t_B and t_A we can write the relationship between deformation and phase:

$$\delta\varphi = \varphi(t_B) - \varphi(t_A) = 4\pi/\lambda(d_B - d_A) \tag{2.14}$$

The relationship between the N unknown phase values φ^Tassociated with the deformation and the vector of the M (known) phase values of interferograms can be defined as follows [23]:

$$\varphi^T = [\varphi(t_1), \dots, \varphi(t_N)\,] \qquad \delta\varphi^T = [\delta\varphi_1, \dots, \delta\varphi_M\,] \tag{2.15}$$

Therefore, the phase deferential for a given interferogram for a master (m) and a slave (s) can be written as:

$$\delta\varphi = \varphi(t_m) - \varphi(t_s) \tag{2.16}$$

Then a matrix representation of a system of M equations with N unknowns can be defined:

$$A\varphi = \delta\varphi \tag{2.17}$$

Where A is an M×N matrix, and for M=N and M>N the equation above can be solved by Least Square (LS) technique, which is limited to a single small baseline subset:

$$\hat{\varphi} = A^{\#}\delta\varphi \qquad with \qquad A^{\#} = (A^T A)^{-1} A^T \tag{2.18}$$

In case of increasing temporal sampling rate of the deformation signal, including probably different subset, the singular value decomposition method (SVD) (due to rank deficiency of the constructed matrix) is used to make a connection between independent acquisition datasets, especially for large baselines [23]. Decomposition of the vector A by SVD, characterized by minimum-norm constraint on the signal phase, forces the solution to be as close to zero as possible, probably leading to large discontinuities in the cumulative deformation [23]. As a result, mean phase velocity between time-adjacent acquisitions is replaced with the unknowns in equation (2.17) to overcome this problem. The block diagram in figure 2.7 represents the SBAS implementation.

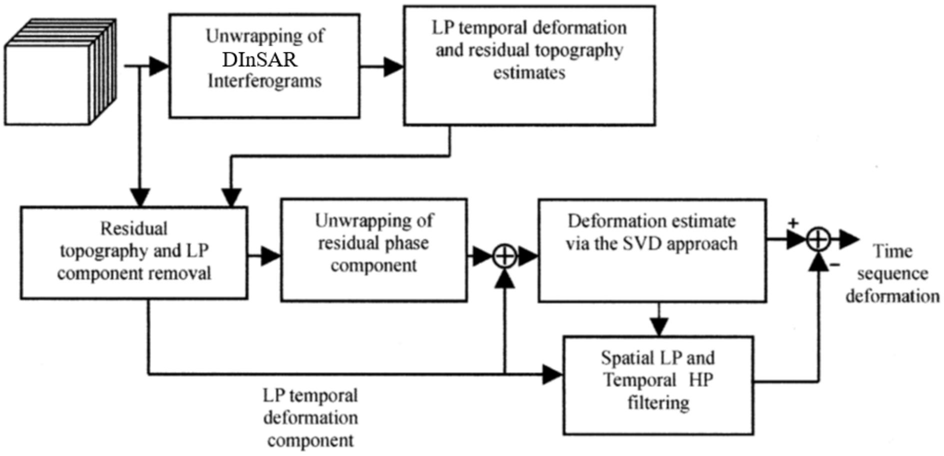

Figure 2.7 : Schematic diagram of SBAS implementation [23]. LP and HP refer to low and high pass filters, respectively.

The atmospheric phase artifacts are removed using the large number of available data (i.e. spatial and temporal information). SBAS is generally based on the three following steps: 1) looking for the high coherent pixels on the data where the noise can be considered negligible using following two main criteria; first, small spatial and temporal baseline; second, minimum frequency shift between the Doppler centroids [30], 2) separating the phase information results from deformation from the undesired phases including the topographic and atmospheric artifacts, 3) removing the artifacts from the interferometric phase and generating the deformation map. Two unwrapping algorithms can be generally used: (1) the minimum cost flow algorithm [31] and (2) the region growing procedure that is used to extend the unwrapping coverage to the low coherent areas. Finally, the atmospheric phase and any possible orbital ramps due to the shifts in satellite orbits are filtered out using the cascade of a low-pass filtering [32]. The main methods used in the baseline configurations of the SBAS algorithm are presented in Table 2.3.

Table 2.3: Summary of the main important baseline configurations

Method	Baseline Configuration	Characteristics
Ferretti [13]	Single master stack	Using only for PSs
Berardino [23]; Schmidt [34]	Short temporal and/or perpendicular	Minimizing the baselines and connection of clusters by (SVD)
van Leijen and Hanssen [35]	Minimal number of connections graph, a traveling salesman solution	Minimizing the baselines using all available SLC's
Perissin et al., [36]	Minimal spanning tree	Minimizing the baselines using all available SLC's

We can use SBAS at the local and regional scales. In the former case, we usually use single look data, to get best possible spatial resolution, and in the latter one, we need to apply multilooking processing [33]. The baseline configurations related to the large interferometric image pairs in the time series may also influence SBAS results. The optimal baseline configuration leads to minimize the noise and therefore the decorrelation. It is expressed in terms of either perpendicular baseline, acquisition temporal baseline or Doppler baseline. In stacking the InSAR time-series, the master should be selected based on the highest stack coherence (γ^m) according to the following equation [21] adopted for the CSK to maximizes the sum correlation of all the interferograms:

$$\gamma^m = \frac{1}{K}\sum_{K=0}^{K} g\left(B_{perp}^{k,m}, 5000\right)\times g\left(T^{k,m}, 1.5\right)\times g\left(f_{dc}^{k,m}, 1260\right) \tag{2.19}$$

where

$$g(x,c) = \begin{cases} 1-|x|/c & if\ |x|<c \\ 0 & otherwise \end{cases} \tag{2.20}$$

with $B_{perp}^{k,m}$ as perpendicular baseline between images m and k at the center of images, $T^{k,m}$ temporal baseline (in years), and $f_{dc}^{k,m}$ Doppler baseline.

2.4 InSAR atmospheric correction

According to (2.7), the fourth component of interferogram phase is related to the variation of signal delay as it travels through the atmosphere. The main source of this delay results in the variation of water vapor in the atmosphere. Water vapor is predominantly found in the troposphere (the lowest 10-12 km part of atmosphere) almost one-half of it is concentrated between sea level and 1.5 km, less than 5-6% above 5 km and less than 1% is within stratosphere (>12 km) (Figure 2.8). Water vapor is highly variable between 0-4% in temporal and spatial scale [31]. The atmospheric phase term (2.7) is locally correlated in space (topography-dependent) and in time on the scale of hours and days. In fact, considering revisit time of SAR satellites (in any case more than a couple of days), the atmospheric signal can be considered uncorrelated in time. The wet component of atmospheric refractivity gives rise excess path of radar signal propagating in the atmosphere [32]. It is usually modelled as a long wavelength component in the unwrapped phase [29]. Sensitivity of the tropospheric refractivity is highest for spatial variations in water vapor content (4-20 times greater than for temperature variation) [15]. Since the total signal delay could be up to several meters, this contribution can represent a very strong limitation for a correct unwrapping of the interferogram [15]. Consequently, atmospheric artifacts could introduce considerable errors to simple or multi-temporal InSAR measurements [33]. Delay measurements could be obtained by space-geodetic tools to estimate perceptible water vapor in the atmosphere [34] and GPS [35]. Generally, to mitigate the atmospheric artifact on InSAR measurements different approaches can be used: 1) InSAR phase model, 2) numerical weather models, 3) multispectral data and 4) GPS data. The first ones rely on linear or non-linear relationships between InSAR phase and topography [36]. The second one uses computation of the refractivity components of weather data to estimate the phase delay [37]. The third ones can provide only the wet component of refractivity [38]. Finally, the last one can yield a point-wise of zenith total delay (wet+ hydrostatic components) [39].

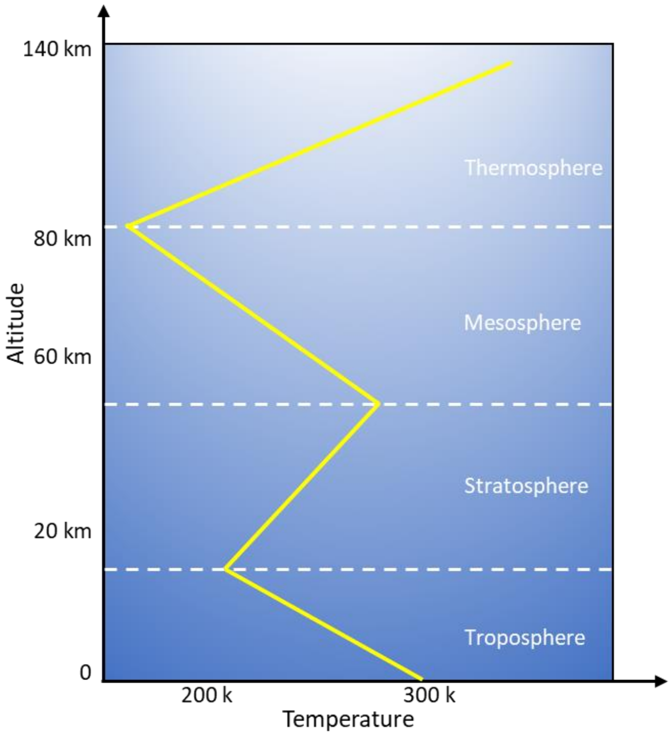

Figure 2.8 : Atmosphere layers (yellow dash line) with temperature (white line)

Generally, phase delay of radar signal induced by the atmosphere can be defined by the atmospheric refractivity N:

$$N = \underbrace{k_1 \frac{P}{T}}_{Hydro} + \underbrace{\left(k_2 \frac{e}{T} + k_3 \frac{e}{T^2} \right)}_{Wet} - \underbrace{\left(4.03\times10^7 \frac{n_e}{f^2} \right)}_{Iono} + \underbrace{1.4W}_{Liquid} \tag{2.21}$$

where T is the temperature (Kelvin), P is the pressure (hPa), e is the partial pressure of water vapor (hPa), n_e is electron number density per cubic meter, f is the radar center frequency and W is the liquid water content (g/m^3), while K_1=77.6, K_2=23.2 and K_3=3.75×10^5 are empirical coefficients [40]. The refractivity term is composed of four components (2.21): hydrostatic or dry N_{hydro} (the first term), wet N_{wet} (the second term), ionospheric N_{iono} (the third term) and liquid N_{liquid} (the forth term). Each component can partially cause some phase delay (i.e., N_{hydro}+ N_{wet}) or phase advance (N_{iono}) of the radar signal. The effect of N_{iono} is often significant for longer wavelengths (e.g., P and L-band), whereas for sensors with shorter wavelengths (e.g., X and C-band) is negligible. The liquid component affects the refractivity just in case of saturated atmosphere and for the InSAR application can be ignored [15]. Therefore, one-way tropospheric delay (S_{trop}) and two-ways tropospheric phase delay (φ_{trop}) can be characterized by integrating over the refractivity along radar line-of-sight at a given height (h) as:

$$S_{trop} = \frac{10^{-6}}{\cos\theta} \int_0^h \left(N_{hydro} + N_{wet} \right) dh \tag{2.22}$$

$$\varphi_{trop} = \frac{-4\pi}{\lambda} S_{trop} \tag{2.23}$$

where -4π/λ is a factor to convert from pseudo-range increase to phase delay [15]. Generally, tropospheric delays vary both vertically and laterally and can be considered as the sum of two components, i) a turbulent component (wet delay) and ii) a vertically stratified component (hydro or dry delay). The former is considered as a short-scale (few km) signal and is highly correlated with topography results from troposphere dynamics. The latter is known as a large-scale (10s of km) signal highly varied in space and time and is related to variations in pressure, temperature, and relative humidity.

Stratified tropospheric delay can cause a long-term bias in estimates of the deformation signal where stacking-based methods are used especially when seasonal variations have not properly been sampled in time [41]. Different methods have been proposed to correct the tropospheric phase delay in SAR data, which can be generally split into two groups: i) phase-based methods (or empirical methods), relying on the correlation between interferometric phase and topography in either a non-deforming area [36][42] or a deforming area (power law) [43], ii) weather-based models (or predictive methods) relying on weather parameters (e.g., pressure, temperature, and relative humidity) of (NWM)[44][37][45] such as ERA-

Interim [37] and ERA5 provided by ECMWF (European Center for Medium-Range Weather Forecasts), Generic Atmospheric Correction Online Service for InSAR (GACOS) (based on HRES-ECMWF)[46], Global Forecast System (GFS) data using Weather Research and Forecast (WRF) model [47][48], Modern-Era Retrospective analysis for Research and Applications (MERRA-2). Satellite spectrometers, utilizing observations of atmospheric water vapor, could also be used to estimate wet delay such as Moderate Resolution Imaging Spectroradiometer (MODIS) [38] and Medium-Resolution Imaging Spectrometer on board Envisat (MERIS)[49]. In addition to that, point-wise GPS measurements can be used to estimate Zenith Total Delay (ZTD), Zenith Wet Delay (ZWD) and Zenith Hydrostatic Delay (ZHD) [50][51][52] alone or in combination with spectrometer data [39].

Each method has its own drawbacks and advantages. For instance, linear methods have two main limitations: i) the requirement to have a non-deforming area (this could be overcome by applying a spatial-band filtering sensitive to deformation [53] or using a deformation model [54]), ii) the simple hypothesis of dependency between phase and elevation does not take into account the spatial variation of atmospheric characteristics. The power law technique [43] was proposed to either operate on a deforming region or consider the spatial variation between phase and elevation.

The efficiency of the atmospheric correction methods is restricted by different variables. For example, Generally, NWM models have a low spatial and temporal resolution and might not be available at the time of SAR data acquisition. Therefore, interpolating in time and resampling in space could potentially lead to an unwanted uncertainty [47]. GPS data are known as accurate pointwise measurements but are not available everywhere. Multi-spectral data can only be used in cloud-free and daylight conditions.

Atmospheric correction methods

Phase delay of radar signal induced by the atmosphere can be defined by the atmospheric refractivity N using (2.21) and one-way tropospheric delay (S_{trop}) and two-ways tropospheric phase delay (φ_{trop}) can be characterized by integrating over the refractivity along radar line-of-sight at a given height (h) by (2.22) and (2.23).

Phase-based tropospheric delay estimation (linear)

Tropospheric phase delay based on the linear model assumes that a linear relation between the interferometric tropospheric delay and the topography exists. This phase delay is estimated from data in a non-deforming region:

$$\Delta\varphi_{trop\_linear} = k_{\Delta\varphi} h + \Delta\varphi_0 \tag{2.24}$$

where the coefficient $k_{\Delta\varphi}$ indicates a constant relating the interferometric tropospheric phase to topography, h the altitude and $\Delta\varphi_0$ is related to a constant shift applied to the whole interferogram that can be therefore neglected [43].

Phase-based tropospheric delay estimation (non-linear)

Since tropospheric phase decreases by decreasing the height and relative delays between different acquisitions are only significant up to a certain altitude h_0 (where phase delays converged to zero), the relationship between phase and topography can be empirically approximated by the following power law function [43]:

$$\varphi_{trop} = k_{\varphi}\left(h_0 - h\right)^{\alpha_d} + \Delta\varphi_0 \quad h < h_0 \tag{2.25}$$

where k_φ is an unknown coefficient relating to phase and topography, which varies spatially in each acquisition. The parameters α_d and $\Delta\varphi_0$ are the power law decay component and the phase delay at the reference height, respectively. The interferometric phase delay (i.e., difference between phase delay of master and slaves acquisitions ($\Delta\varphi_{trop} = \varphi_{trop}^{m} - \varphi_{trop}^{s}$) is obtained according to:

$$\Delta\varphi_{trop} = (k_{\varphi m} - k_{\varphi s})(h_0 - h)^{\alpha_d} \quad , \; k_{\Delta\varphi} = (k_{\varphi m} - k_{\varphi s}) \tag{2.26}$$

where $k_{\Delta\varphi}$ can be estimated by applying band-filtered phase and topography to (2.26) due to the fact that the tropospheric phase is present in all wavelength scales and the spatial frequency band is relatively not sensitive to other signals such as incorrect orbit and ionospheric delay [43][53].

NWM-based tropospheric delay estimation

The second type of the correction method exploits the availability of external data sets. NWM has a great potential in phase delay estimation in InSAR applications as an external data. In this approach, atmospheric variables are used to estimate the refractivity components (2.21) These NWM models are various in terms of spatio-temporal resolution and data provider. Therefore, the use of each model to estimate spatiotemporal variations of both water vapor and temperature (wet delay) and pressure (hydrostatic or dry delay) might lead to a different accuracy and precision in phase delay estimation. To determine the robustness and weakness of each NWM model we use ERA-Interim, ERA5, MERRA2 and WRF models for phase delay estimation and GACOS and GPS data for purpose of the results accuracy assessment.

Multi-spectral data

The MODIS data can be used to estimate the wet component of refractivity under cloud-free and daylight conditions. Five near-infrared (IR) MODIS channels including three water vapor absorption and two non-absorption are usually used to estimate water vapor. MODIS could retrieve water vapor using observations of water vapor attenuation of reflected solar radiation in the near-IR channels up to an accuracy of 5-10% [39] [55]. Comparison of water vapor estimated by MODIS data to GPS and radiosonde are pointed out that MODIS overestimates water vapor by a scale factor of 1.07-1.2. Therefore, MODIS-driven wet delay should be calibrated before using it in InSAR atmospheric correction [56].

2.5 Offset tracking techniques

Generally, offset could be estimated through following techniques:

1) Relying on azimuth split-bandwidth of master and slave images into forward and backward including i) spectral diversity and ii) multi-aperture interferometry techniques;
2) Relying on Coherence using complex multiplication between master and slave images and based on intensity information of master and slave images (hereafter called Incoherent Cross Correlation (ICC)) offset estimation;
3) Offset estimation-driven from image processing techniques including template-based matching.

Each approach is addressed in detail in the following sub-sections.

2.6 Spectral Diversity (SD) and Multi-Aperture Interferometry (MAI)

The SD method was initially developed to specify absolute phase [57]. It was then used to improve co-registration accuracy between two SAR images [58]. SD extracts phase difference from an interferogram by a band-pass filter. It utilizes a linear phase element of the demodulated Impulse Response Function (IRF) in azimuth direction for master $A_m(t)$ and slave $A_s(t)$ data (see Figure 2.99). The amplitude of an azimuth IRF is modulated by the position of the reflected signal in the azimuth antenna and then the real signal is obtained by removing the modulation through matched filtering [58]. A reference signal created by the Doppler history of satellite pulses can be defined as follows:

$$A_m(t) = e^{j\varphi_1} e^{j2\pi f_{dc1}(t-t_0)} \operatorname{sin}c\left(\pi K_{a_1}(t-t_0)\right) \tag{2.27}$$

$$A_s(t) = e^{j\varphi_2} e^{j2\pi f_{dc2}(t-t_0-\Delta t)} \operatorname{sin}c\left(\pi K_{a_2}(t-t_0-\Delta t)\right) \tag{2.28}$$

where *t* and *t₀* indicate time variable and zero Doppler frequency position (D_{f1}), respectively. φ_1 and φ_2 refer to signal phases, the *sinc(t)* function is given by *sin(x)/x* and K_a is the Doppler bandwidth covered by both master and slave. All the following parameters become equal when a command band filter (K_a) is applied (see Figure 2.9):

$$K_a = K_{a1} = K_{a2} \tag{2.29}$$

$$f_{dc} = f_{dc1} = f_{dc2} \tag{2.30}$$

In case of misregistration, an additional phase φ_{misreg} will be add to the interferogram:

$$\phi_{misreg} = 2\pi f_{Dc} \Delta t \tag{2,31}$$

The estimation of Δt can be used to retrieve a misregistration of pixel offset, as it includes the amplitude and linear phase information of IRF.

The timing shift Δt is specified by the principle of a linearly varying Doppler centroid. In order to specify the timing shift Δt the bandwidth is split into two equal sections and forming four sub-images ($f_1^A, f_1^B, f_2^A \; and \; f_2^B$), where *A* and *B* refer to the sub-band one and two (see Figure 2.9), respectively. For each sub-look we will have:

$$c_1^A(t) = e^{j\varphi_1} e^{j2\pi f_{dc}^A (t-t_0)} \sin c\left(\pi K_a \left(t - t_0\right)\right) \tag{2,32a}$$

$$c_1^B(t) = e^{j\varphi_1} e^{j2\pi f_{dc}^B (t-t_0)} \sin c\left(\pi K_a \left(t - t_0\right)\right) \tag{2, 32b}$$

$$c_2^A(t) = e^{j\varphi_2} e^{j2\pi f_{dc}^A (t-t_0-\Delta t)} \sin c\left(\pi K_a \left(t - t_0 - \Delta t\right)\right) \tag{2, 32c}$$

$$c_2^B(t) = e^{j\varphi_2} e^{j2\pi f_{dc}^B (t-t_0-\Delta t)} \sin c\left(\pi K_a \left(t - t_0 - \Delta t\right)\right) \tag{2, 32d}$$

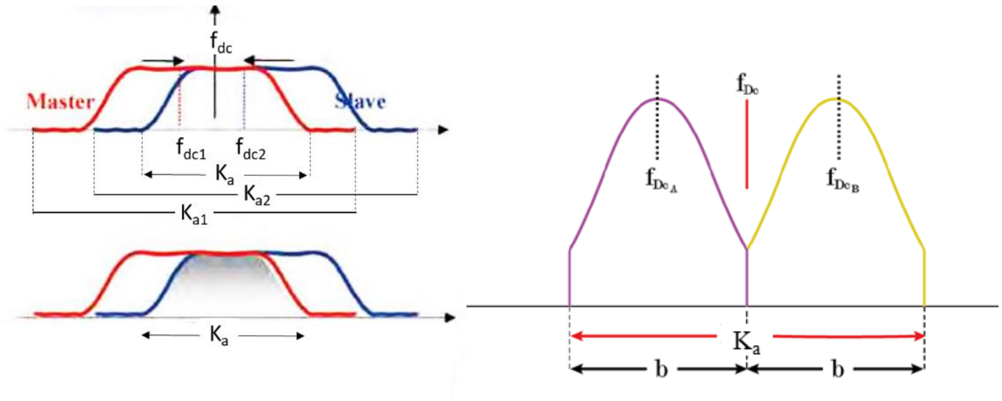

Figure 2.9 : (a) band command filter implementation to achieve K_a on a master and slave (the modified figure was taken from the training manual (TM-19_ptB) of the European Space Agency (ESA))) and (b) Gaussian weighted sub band filter to divide bandwidth SD interferogram [58].

A complex multiplication is applied to sub-bands (i.e., upper sub-band of ‘a’ and lower sub-band of ‘b’) of master and its conjugative slave [58]:

$$v_l = c_1^A c_2^{A*} = \left|c_1^A\right|\left|c_2^A\right| e^{j\phi_1^A - \phi_2^A} \qquad (2,33a)$$

$$v_u = c_1^B c_2^{B*} = \left|c_1^B\right|\left|c_2^B\right| e^{j\phi_1^B - \phi_2^B} \qquad (2,33b)$$

Phase differential of upper $(\varphi_u = \varphi_1^A - \varphi_2^A)$ and lower $(\varphi_l = \varphi_1^B - \varphi_2^B)$ sub-bands of interferograms yields differential SD:

$$\varphi_{SD} = \varphi_l - \varphi_u \qquad (2.34)$$

After that, the SD phase is converted to timing error (2.35) and then to spatial misalignment in pixel offsets by means of azimuth Ka (2.36)

(2.34). Finally, the azimuth offset is obtained by multiplying by Pixels Pacing (PS) (2.37)[59]:

$$\Delta t = \frac{\varphi_{SD}}{2\pi\left(f_{dc}^{a} - f_{dc}^{b}\right)} \qquad (2.35)$$

$$\Delta\hat{x} = \Delta t . K_a \qquad (2.36)$$

$$\Delta x_{azimuth} = \Delta\hat{x} . PS \qquad (2.37)$$

The accuracy equation for the SD method is defined [60] as:

$$\sigma_{SD} = \frac{1}{2\sqrt{2}} \frac{B_c}{B_c - B_s} \sqrt{\frac{B_c}{b_s}} \frac{1}{\sqrt{N}} \frac{\sqrt{1-\gamma^2}}{\pi\gamma} \tag{2.38}$$

where γ, N, B_c and B_s refers to coherence, number of independent samples, bandwidth, and sub-bandwidth, respectively.

MAI is a SD-based technique that is used to extract along-track displacements from InSAR data [61]. The MAI technique is based on an azimuth sub-aperture processing including splitting the SLC images into forward and backward looks and reducing the Doppler band by one-half. Then, MAI interferograms are made using multiplying complex conjugate multiplication of the forward and backward sub-bands [61] (see Figure 2.10).

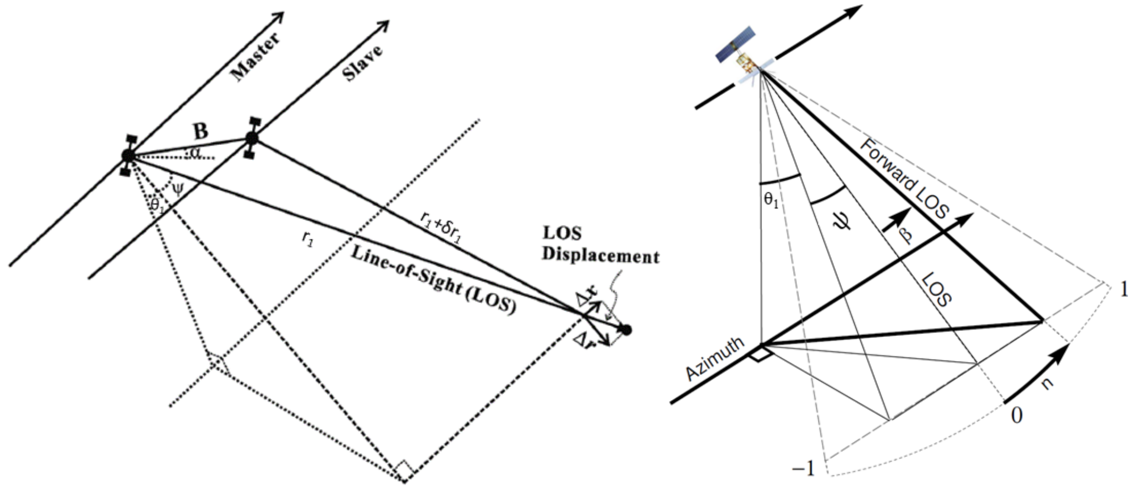

Figure 2.10 : InSAR imaging geometry for one and two satellites. The parameters Δr and Δx indicate cross and along track displacement, respectively. δr_1 refers to slant range variation between master and slave images.

As shown in the Figure 2.10, the InSAR phase of Line Of Sight (LOS) displacement is defined as:

$$\varphi_{InSAR} = \frac{4\pi}{\lambda}\left(\delta r_1 + \Delta r \cos\psi + \Delta r \sin\psi\right) \tag{2.39}$$

where ψ is the squint angle and δr_1 can be approximately by $\delta r_1 \approx -B\sin(\theta_1 - \alpha)$[62] and α is baseline orientation. Due to the zero Doppler geometry (ψ=0), the InSAR phase can be rewritten:

$$\varphi_{InSAR} = \frac{4\pi}{\lambda} B \times \sin\left(\theta_1 - \alpha\right) + \frac{4\pi}{\lambda}\Delta r \tag{2.40}$$

The forward and backward interferometric phase ($\varphi_{InSAR,f}$ and $\varphi_{InSAR,f}$) are defined as follows:

$$\varphi_{InSAR,f} = -\frac{4\pi}{\lambda}\left(B - \frac{\Delta B}{2}\right) \times \sin\left(\theta_1 - \alpha - \frac{\Delta\theta_1 - \Delta\alpha}{2}\right) + \frac{4\pi}{\lambda}\left[\Delta r \cos\left(\psi + \frac{\Delta\beta}{2}\right) + \Delta x \sin\left(\psi + \frac{\Delta\beta}{2}\right)\right] \quad (2.41)$$

$$\varphi_{InSAR,b} = -\frac{4\pi}{\lambda}\left(B + \frac{\Delta B}{2}\right) \times \sin\left(\theta_1 - \alpha + \frac{\Delta\theta_1 - \Delta\alpha}{2}\right) + \frac{4\pi}{\lambda}\left[\Delta r \cos\left(\psi - \frac{\Delta\beta}{2}\right) + \Delta x \sin\left(\psi - \frac{\Delta\beta}{2}\right)\right] \quad (2.42)$$

where ΔB is the baseline separation, $\Delta\beta$ antenna angular beam width, $\Delta\alpha$ is baseline orientation [62]. The MAI interferometric phase is achieved by forward and backward phases using approximation of $\psi \approx 0$ and $|\Delta\theta - \Delta\alpha| \approx 0$ [63]:

$$\varphi_{MAI} = \varphi_{InSAR,f} - \varphi_{InSAR,b} \approx \frac{4\pi}{\lambda}\Delta B \times \sin\left(\theta_1 - \alpha\right) + \frac{4\pi}{\lambda}\Delta\beta\Delta x \quad (2.43)$$

$$\Delta\beta = n.\beta = n\,\frac{\lambda}{l_a} \quad (2.44)$$

where n indicates a normalized squint (which is a fraction of the whole aperture) and l_a is the length of azimuth antenna. By substituting (2.44) in (2.7), the MAI phase is obtained:

$$\varphi_{MAI} = \frac{4\pi}{\lambda}\Delta B \times \sin\left(\theta_1 - \alpha\right) + \frac{4\pi}{l_a} n \Delta x \quad (2.45)$$

After removing the flat-Earth and topographic phase, the MAI interferogrm is obtained and along track displacement of MAI phase can be derived:

$$\Delta x = \frac{\varphi_{MAI}}{4\pi}\frac{l_a}{n} \quad (2.46)$$

According to (2.46), the along track displacement is directly related to the azimuth antenna length. For instance, the l_a=10m antenna length of ERS satellite and $\Delta x = 1$m along track displacement give 0.6 radians of phase difference.

2.7 Coherence and intensity SAR-based Offset tracking techniques

Coherent Cross Correlation (CCC) and Incoherent Cross Correlation (ICC) are two common methods to estimate the offset of an object on a pair of SAR. The former relies on complex of data (i.e., amplitude and phase), while the later operates on intensity information only (i.e., amplitude squared). Image patch cross correlation-based methods can be used as alternative solution for ICC to estimate offset with a procedure similar to ICC.

2.7.1 Coherent Cross Correlation (CCC)

The optimum (maximum-likelihood) estimator (MLE) for differential shift of partially correlated circular Gaussian signals can be used as a cross-correlation operation on a complex image. In this method, the systematic (non-noise) phase difference between two data , such as spectral shift filtering and removal of topographic fringes, must be omitted prior to cross correlation [64]. The obtainable accuracy with ICC is defined in terms of error standard deviation as a function of the coherence and the number of independent samples (resolution cells) [60][65]:

$$\sigma_{CCC} = \sqrt{\frac{3}{2N}}\frac{\sqrt{1-\gamma^2}}{\pi\gamma} \tag{2.47}$$

2.7.2 Incoherent Cross Correlation (ICC)

In contrast with CCC, ICC uses amplitude or intensity of SAR data (which is also known as speckle tracking). In the ICC method, SAR data are generally oversampled by a factor of two. The result is highly dependent on neighboring pixels. It is argued that since ICC utilizes only half of the available information, thus its error could be larger by $\sqrt{2}$. It is reported that the cross correlation performance of amplitude signal is worse than that of the intensity signal for low coherence cases, as amplitude signal needs more oversampling due to the non-linearity of square root [66]. Accuracy of incoherent cross correlation (or incoherent speckle tracking) for circular Gaussian signals is defined as follows:

$$\sigma_{ICC} = \sqrt{\frac{3}{10N}}\frac{\sqrt{2+5\gamma^2-7\gamma^4}}{\pi\gamma^2} \tag{2.48}$$

where N is the number of independent samples (for the original complex images) and γ is the coherence. The equation (2.48) plotted as function of γ in Figure 2.11.

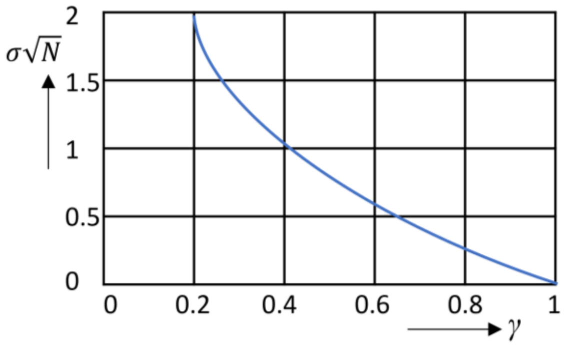

Figure 2.11 : Normalized shift estimation error $\sigma\sqrt{N}$ versus γ.

A comparison of CCC, ICC and SD methods in the SAR domain is provided in the following. The precision equations of the coherent (CCC) (2.33), incoherent (ICC) (2.34) and spectral diversity (SD) (2.25) can be analyzed. By assuming $\gamma\rightarrow1$, the variance comparison ratio shows that σ_{ICC}^2 is 1.8 times larger than σ_{CCC}^2 ($\sigma_{ICC}^2/\sigma_{CCC}^2 = 9/5 = 1.8$) [66]. It means that ICC will provide a better precision than CCC when we have good coherence. In the same way, the accuracy ratio ($\sigma_{SD}^2/\sigma_{CCC}^2$) of SD and CCC are equal to 1.06 and 1.15 (assuming 6% difference in accuracy is neglectable), respectively, for the bandwidth gap of 1/3 and 1/5 [59].

In summary, SAR-based Offset Tracking (OT) has been proposed to overcome the LOS displacement detection limit of the DInSAR technique. OT uses the cross-correlation to estimate relative shifts between two pixels, and to compute filters that shape one signal to match another (fast local). Two of the most important advantages of this technique are the mapping of 2-D displacements (azimuth and range directions), and the fact that there is no need for complex phase unwrapping algorithms which could give wrong results or fail in case of decorrelation or fast ground deformations. As sub-pixel offset tracking is highly sensitive to the spatial resolution of the data, latest generations of SAR sensors such as TerraSAR-X and COSMO-SkyMed providing high resolution data (up to 1m) have great potential to become established methods in the field of ground deformation monitoring. The performance of OT and MAI techniques to extract the along-tack displacement component are presented for several sensors in Table 2.4.

Table 2.4: Comparison of the empirical accuracies of MAI and Pixel-offset tracking [37], [38], [39], [40].

Methods	**Accuracy**	**Azimuth resolution %**
pixel-offset for ERS	12 to 15 cm	2.4%–3.0%
pixel-offset for PALSAR	7.1 cm	1.6%
MAI for PALSAR	6.3 cm - 3.57 cm	1.3%

2.8 Template matching-based offset tracking techniques

Template matching algorithms are widely used in digital image processing to find and match objects in an image with a template image, which is placed under category of area-based algorithms). Template matching algorithms are used for image registration and feature matching. Generally, template matching algorithms can be classified into three groups [67]:

1) featured-based algorithms, while are well suited to extract the features using their spatial relations or descriptors;
2) patch or area-based algorithms, while consider the intensity of the pixel values obtained after cross-correlation-based similarity;
3) optical-flow or motion tracking algorithms.

The first group is mainly appropriate to match structural information (i.e., features), the second one fits for intensity information and the third one is based on the relation between photometric correspondence vectors and spatiotemporal derivatives of luminance in an image sequence [68]. Template matching relies on either intensity (area-based algorithms) or phase information (e.g., phase correlation (PC)) of images. In the following, we will briefly review basic of cross correlation, and then address normalized cross correlation (NCC) phase correlation (PC) and orientation correlation (OC) methods.

The principle of template matching-based methods of area-based algorithms relies on a predefined template with a given window size that is moved within the search window area to find the highest similarity to match a feature. The template matching-based estimator principle is illustrated in Figure 2.12. The theory behind each method that has been used in this manuscript and some implementation details related to the data processing are briefly described in the following.

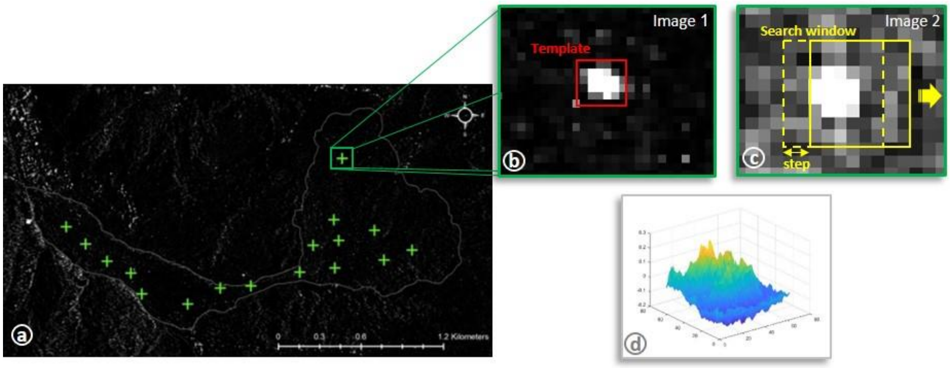

Figure 2.12 : Principle of a template matching-based estimator. (a) First acquisition of the geocoded CSK data; (b) a selected template including the distinctive CR footprint; (c) search within the moving window on the image with a given step and (d) typical example of CC values using NCC (vertical axis represents the correlation coefficient values).

Normalized Cross Correlation (NCC) is a robust and simple method to seek for a particular pattern that has probably been shifted in two subsequent (in time) images to find the related offset. Generally, NCC is following steps: 1) Calculate cross-correlation in the spatial or the frequency domain, depending on size of images, 2) Calculate local sums by precomputing running sums, and 3) Use local sums to normalize the cross-correlation to get correlation coefficients. In NCC-based offset tracking, a template with function $I_2(x,y)$ and size $N_x \times N_y$ is moved across an image with the function $I_1(x,y)$ and size of $M_x \times M_y$ by u step in x-direction and v step in y-direction pixel-by-pixel. All cross-correlation coefficients are stored in the correlation matrix as follows:

$$CC(u,v) = \frac{\sum_{x,y}\left(I(x,y)-I_{u,v}\right)\left(t(x-u,y-v)-\bar{t}\right)}{\sqrt{\sum_{x,y}\left(I(x,y)-I_{u,v}\right)^2\left(t(x-u,y-v)-\bar{t}\right)^2}} \tag{2.49}$$

where $u \in \{0,1,2,\ldots,M_x-N_x\}, v \in \{0,1,2,\ldots,M_y-N_y\}$, and $\bar{f}_{u,v}$ and $\bar{t}$ indicate the average value of the search $f_1(x,y)$ and $f_2(x,y)$ template windows shifting with (u,v) steps. Computation of Equation (2.49), especially for a large image, is intensive and needs a number of operations in order of $(N_x \times N_y) \times (M_x - N_x) \times (M_y - N_y)$ [69]. For instance, the computational load for an NCC calculation with a template and search windows size of 64 × 64 and 128 × 128 pixels, respectively, is more than 10^6 operations. NCC is invariant to linear brightness and contrast variations, and its easy hardware implementation. However, traditional correlation-based image matching methods will fail when intense changes in rotation or scale occur between the two images, as NCC is sensitive to rotation and scale changes. A sub pixel accuracy is achievable by interpolation in NCC.

The Phase Correlation (PC) method is a frequency domain technique used to estimate the delay or shift between two copies of the same signal [70]. Phase correlation-based methods can generally be split into two classes. In the first class, the relative images' shift is recovered by explicitly estimating the linear phase of the images' cross-spectrum [71]. In the second class, the relative displacement is calculated by determining the exact location of the correlation peak [26]. In the phase correlation method, $f_1(x,y)$ and $f_2(x,y)$ are two signals corresponding to windows of the first and second images at the time of t_1 and t_2 that are supposed to be matched. The offset (Δx and Δy) presented in the second image (f_2) is defined by:

$$f_2(x,y) = f_1(x-\Delta x, y-\Delta y) \tag{2.50}$$

By applying the Fourier transformation, the normalized phase correlation (known as the cross-power spectrum) can be obtained as follows:

$$CC(u,v) = \frac{F_2(u,v)F_1(u,v)^*}{\left|F_2(u,v)F_1(u,v)^*\right|} = e^{-i(u\Delta x + v\Delta y)} \tag{2.51}$$

where F_1 and F_2 are the FFT of f_1 and f_2, respectively and * indicates the complex conjugate. The phase-only correlation (POC) function CC(u,v) is defined as the inverse Fourier transform of R(ω). The shift property of the Fourier transform can determine the offset by simply locating the maximum of CC(u,v) [72]. The main drawback of PC, at least in its basic form, is that the offset retrieval has pixel accuracy not sub-pixel accuracy. The robustness of phase correlation technique is usually evaluated with sensitivity to additive white noise and blur, and images phase difference.

Two PC versions were applied to the intensity-based SAR images: (i) the standard PC; and (ii) a modified version of PC (MPC). MPC minimizes the weighted residual matrix between the computed normalized cross-spectrum and the theoretical one to both reach more flexibility on the frequency weighting and to solve the phase wrapping ambiguity. It uses an iterative process (re-computing times of frequency mask adaptively) to increase the robustness and accuracy, and frequency masking to obtain a bias-free correlation [73]. The robustness iteration and mask threshold parameters are firstly set to 2 and 0.9, respectively. To investigate the role of the robustness iteration parameter in accuracy improvement of the offset estimation, its value is then increased to 4 by a resampling process.

Orientation correlation (OC) is an algorithm that has been proposed for translational image registration, operating on correlating orientation images. Although OC is considered as a feature-based matching algorithm, its matching procedure is based on feature of gradient orientation not extracting of available features an image such as corner, line and junction. Therefore, in OC algorithm, each pixel in an orientation image is a complex number that represents the orientation of intensity gradient., which is invariant to illumination change. Angles of gradient orientation are used for matching, Andrews robust kernel function is applied to angle differences and correlation computed by Fast Fourier Transforms [74].
OC initiates with indexing images using (*x*,*y*), where *x* and *y* are integers, two images I_1 and I_2 are matched. The Orientation Intensity Of Gradient (OIOG) of the images I_1 and I_2 are computed according to [74]:

$$I_1(x,y)=\operatorname{sgn}\left(\frac{\partial I_1(x,y)}{\partial x}+i\,\frac{\partial I_1(x,y)}{\partial y}\right) \tag{2.52}$$

$$I_2(x,y)=\operatorname{sgn}\left(\frac{\partial I_2(x,y)}{\partial x}+i\,\frac{\partial I_2(x,y)}{\partial y}\right) \tag{2.53}$$

$$\operatorname{sgn}(x)=\begin{cases}0 & if\ |x|=0\\ \dfrac{x}{|x|} & otherwise\end{cases} \tag{2.54}$$

sgn(*x*) and *i* indicate the sign function and complex imaginary unit, respectively. The orientation images are then matched using inverse FFT-based correlation. Since OIOG on the images has no gradient (i.e., 0 + 0*i*) for uniform regions and is equal to 1, hence, OC is invariant to offset illumination changes. The registration of I_1 and I_2 is measured from the position of the maximum taken from Inverse Fast Fourier Transform function of the orientation correlation matching surface. According to the OC performance analysis [74], it is invariant to both scale and offset illumination changes, statistically robust to images containing a higher level of noise, low computational complexity (mainly due to two forward and one backward FFTs of complex value images) with respect to its counterparts.

2.8.1. Featured-tracking based algorithms (corner-based detector and descriptors)

A Featured-based algorithm is appropriate when both reference and template images contain distinctive features such as points and curves. A pair-wise link is set and matched between the two aforementioned images using a feature detectors and descriptors based on spatial relations. The feature detectors identify an intended object while feature descriptors match the corresponding objects found in the two images. Generally, both approaches use decomposing an image into local regions of interest or features to reduce complexity utilizing local appearance characteristics [75]. A robust keypoint detector must be able to detect distinctive regions despite changes of viewpoint and potential transformations occurred in an image (repeatable property), likewise a powerful keypoint descriptor should manage to extract the most significant information within the detected instinctive regions (recognizable ability). In terms of nature of an object in an image, featured-based detectors and descriptors algorithms can be classified into two main categories: corner-based feature including BRISK, MEIGEN, HARRIS, FREAK and FAST, and blob-based including SURF.

Binary Robust Invariant Scalable Keypoints (BRISK)

Effective and efficient generation of keypoints is a significant challenge in of numerous Computer Vision applications. BRISK is a novel method for keypoint detection, description and matching, which is BRISK aims to meet two competing objectives: high quality description and low computational requirements. BRISK uses scale-space FAST-based detector in combination with the assembly of a bit-string descriptor from intensity comparisons retrieved by dedicated sampling of each keypoint neighborhood [75]. BRISK operates through two main steps: (i) scale-space keypoint detection and scale dimensions in the image, and (ii) relying on applying a sampling pattern of the detected keypoints. The former uses a saliency criterion (keypoints detection is done by means of octave layers of the image pyramid (one-fourth of original area) and the layers in between (see Figure 2.13). The latter is based on appropriately scaled concentric circles at the neighborhood of each keypoint to retrieve gray values [75] (see Figure 2.14).

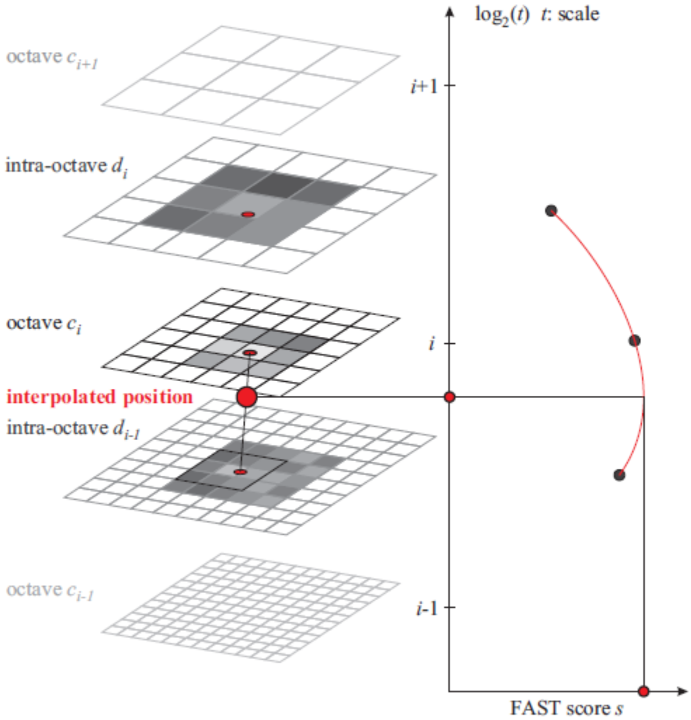

Figure 2.13 : Scale-space point detection. A keypoint is detected at octave c_i, analyzing the eight neighboring saliency scores in c_i [75].

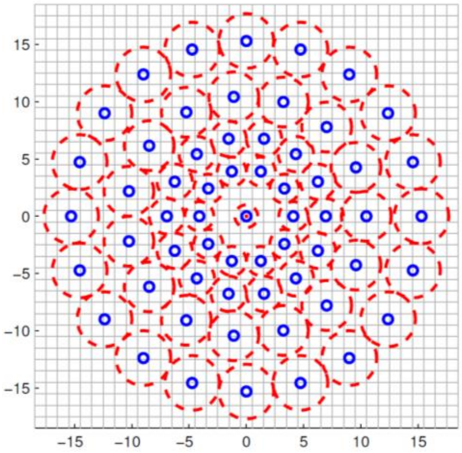

Figure 2.14 : The BRISK sampling pattern with N = 60 points: the small blue circles denote the sampling locations; the bigger, red dashed circles are drawn at a radius σ corresponding to the standard deviation of the Gaussian kernel used to smooth the intensity values at the sampling points. The pattern shown applies to a scale of t = 1[75].

The Hamming distance can be used to match two BRISK descriptors, which is based on that the dissimilarity measure of the number of bits different in the two descriptors. The results of experimental test proved that BRISK provides a dramatically faster alternative at comparable matching performance in comparison with well-known Speeded Up Robust Features (SURF) and Scale-Invariant Feature Transform (SIFT) [75]. An example of the BRISK detection in two images of the Boat sequence is shown up-close in Figure 2.15.

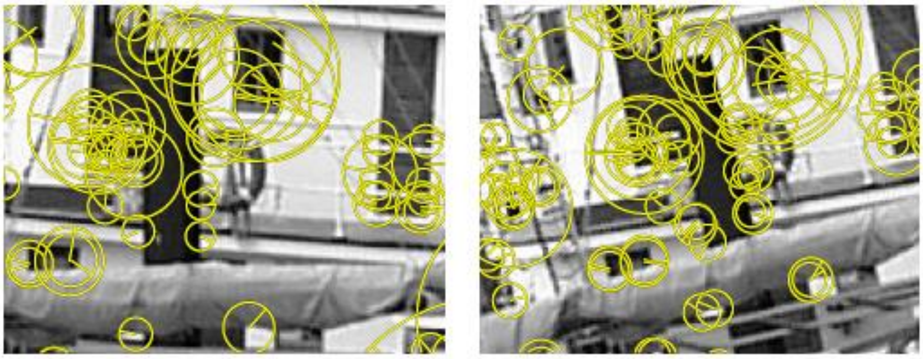

Figure 2.15 : An example of BRISK detection function. The images show two boats with slight changes in scale and rotation. The size of the circles and the corresponding radii o indicate the scale and orientation of the detected keypoints [75].

In comparison with available algorithms with proven high performance, such as SIFT and SURF, the method at hand offers a dramatically faster alternative at comparable matching performance – a statement which we base on an extensive evaluation using an established framework. BRISK works an easily configurable circular sampling pattern from which it computes brightness comparisons to form a binary descriptor string [75].

Minimum Eigenvalue (MEIGEN) proposes a feature selection criterion that is optimal by construction, since it relies on how a tracker works. Actually, MEIGEN is a tracking algorithm that extends previous Newton-Raphson style search methods to work under affine image transformation [76]. MEIGEN monitors the quality of image feature during tracking by using a measure of feature dissimilarity that quantifies the change of appearance of the feature between the first and the current one. The dissimilarity is the feature's rms residue between the first and the current frame, and when dissimilarity grows too large the feature should be abandoned [76]. This method defines a term for feature quality in the sense that a good feature is one that can be tracked well. The selection criterion is yielded in the following. Let us consider an image *I(x)* and a matrix *G* defined as follows:

$$G = \begin{bmatrix} I_x^2 & I_x I_y \\ I_x I_y & I_y^2 \end{bmatrix} \quad , \quad I_x = \partial I / \partial x \quad \text{and} \quad I_x = \partial I / \partial y \tag{2.55}$$

A good feature can be detected by analyzing the eigenvalues of G [77]. Three states can happen in terms of eigenvalues magnitude: (i) if both eigenvalues are small, the considered window has a little intensity variation, (ii) if one eigenvalue is small and the other one is large, this can be treated as a one dimensional horizontal and vertical edge, and (iii) if both eigenvalues are large, the feature can be identified as corner [78][77]. A window provides a good feature through eigenvalues of *G* (i.e., I_1 and I_2) if:

$$\lambda_1, \lambda_2 \quad > \lambda_{th} \tag{2.56}$$

where λ_{th} is a predefined threshold. Since many windows can fulfill the above condition such as a slanted edge, thus, optimal image window sizes selection is challenging task. MEIGEN is a feature selection that maximize the quality of tracking. Feature monitoring is computationally expensive and helps discriminating between good and bad feature based on a measure of dissimilarity that uses affine motion as the underlying image change model. A good discrimination at the beginning of the processing chain can reduce the remaining bad feature to a few outliers, rather than leaving them an overwhelming majority [76].

Combined Corner and Edge Detector (HARRIS)

The HARRIS algorithm [79] relies on recognizing keypoint is by looking through a small window in the sense that shifting window in any direction should provide a large change in intensity. In his respect, three regions can be defined. “Flat region” means no change in all directions, “edge” refers no change along the edge direction and “corner” provides significant change in all direction. (Figure 2.16). The mathematical form of intensity difference for displacement of (u, v) in all directions defines as:

$$E(u,v) = \sum_{x,y} \underbrace{w(x,y)}_{\text{window function}} \left[\underbrace{I(x+u, y+v)}_{\text{shifted intensity}} - \underbrace{I(x,y)}_{\text{intensity}} \right]^2 \tag{2.57}$$

Rectangular and Gaussian windows can be used as base functions in the above formula (Figure 2.16).

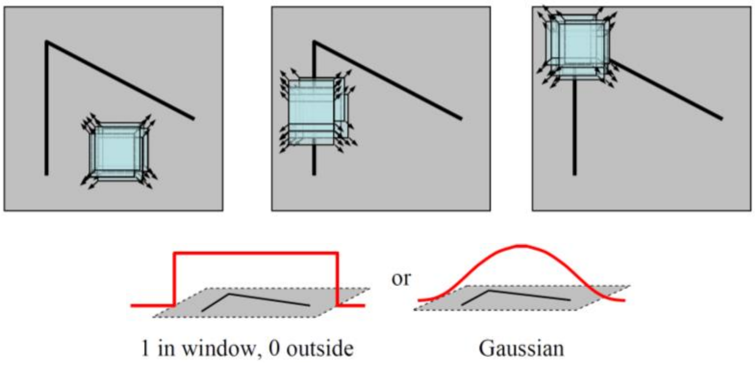

Figure 2.16 : Three statues recognized by HARRIS and Rectangular and Gaussian window functions. On the top from left to right, the figures refer to flat, edge and corner regions.

By applying Taylor expansion, we can obtain [79]:

$$E(u,v) \approx \begin{bmatrix} u & v \end{bmatrix} M \begin{bmatrix} u \\ v \end{bmatrix} \quad , \quad M = \sum_{x,y} w(x,y) \begin{bmatrix} I_x I_x & I_x I_y \\ I_x I_y & I_y I_y \end{bmatrix} \tag{2.58}$$

As in (2.55), I_x and I_y are image derivatives. The score variable R can be used to understand if the window contains a corner feature or not:

$$R = \det(M) - k\left(trace(M)\right)^2 \tag{2.59}$$

where λ_1 and λ_2 are eigenvalues of M, *det(M)* equals multiplication of λ_1 and λ_2 and *trace(M)* is sum of λ_1 and λ_2. The decision making whether a region is corner, edge or flat is based on the following conditions (Figure 2.17):

- **Flat:** when $|R|$ is small, i.e., is when λ_1 and λ_2 are small.
- **Edge:** when $R<0$, i.e., when $\lambda_1 >> \lambda_2$ or $\lambda_2 >> \lambda_1$.
- **Corner:** when R is large, i.e., when λ_1 and λ_2 are large and with similar values $\lambda_1 \sim \lambda_2$.

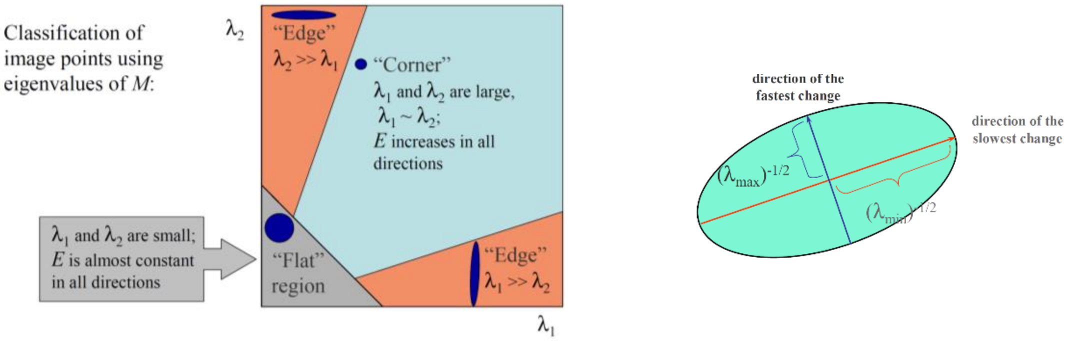

Figure 2.17 : Intensity change in shifting window and eigenvalue analysis

Fast Retina Keypoint (FREAK)

FREAK is a keypoint descriptor inspired by the human visual system. In FREAK, a cascade of binary strings (i.e., 0 and 1) is computed by efficiently comparing image intensities over a retinal sampling pattern. FREAK uses a retinal sampling grid that is circular like BRISK with a higher density close the center which exponentially declines toward the circular edge [80] (see Figure 2.18).

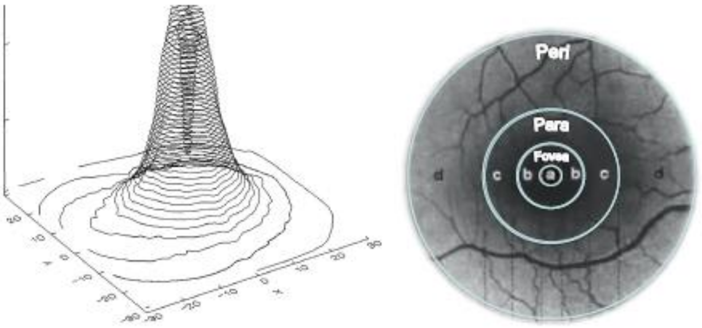

Figure 2.18 : Density of ganglion cells over the retina (on the left) and retina areas (on the right) [80].

FREAK operates in four following steps [80]:

- **Retinal sampling pattern:** using different kernels size for every sample point similar to BRISK with the difference in using exponential change in size and the overlapping receptive fields.

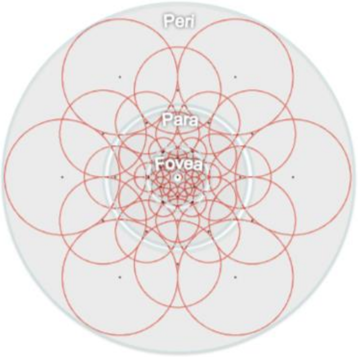

Figure 2.19 : Illustration of the FREAK sampling pattern similar to the retinal ganglion cells distribution with their corresponding receptive fields. Each circle represents a receptive field where the image is smoothed with its corresponding Gaussian kernel [80].

- **Coarse-to-fine descriptor:**
  The FREAK is defined as a binary descriptor F that is a binary string created by a sequence of one-bit Difference of Gaussian (DOG):

$$F = \sum_{0<a<N} 2^a T\left(P_a\right) \quad , \quad T\left(P_a\right) = \begin{cases} 1 & if \quad \left(I\left(P_a^{r1}\right) - I\left(P_a^{r2}\right)\right) > 0 \\ 0 & otherwise \end{cases} \qquad (2.60)$$

where P_a, N and $I\left(P_a^{r1}\right)$ are a pair of respective fields, the desired size of the descriptor and the smoothed of the first receptive field of the pair P_a, respectively (Figure 2.20).

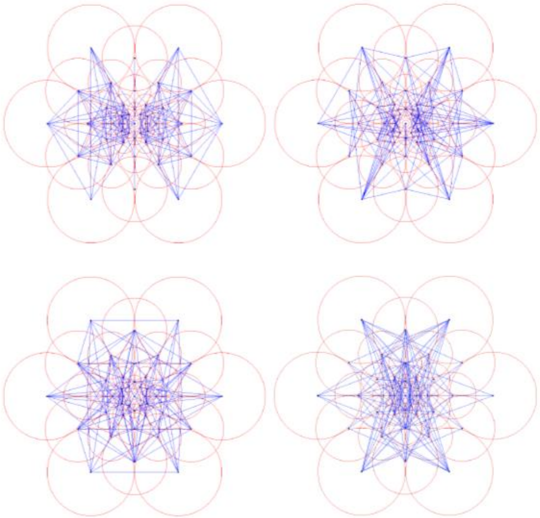

Figure 2.20 : Illustration of the coarse-to-fine analysis. The first cluster involves mainly perifoveal receptive fields and the last one's fovea [80].

- **Saccadic search:** initiating to mimic the saccadic search by parsing our descriptor in several steps. We start by searching with the first 16 bytes of the FREAK descriptor representing coarse information.
- **Orientation:** estimating the rotation of our keypoint using summation of the estimated local gradients over selected pairs similar to BRISK. The latter is using long pairs to compute the global orientation whereas we mainly select pairs with symmetric receptive fields with respect to the center (see Figure 2.21) [80].

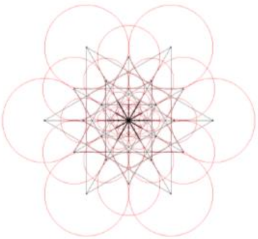

Figure 2.21 : Illustration of the pairs selected to computed the orientation [80].

In terms of performance evaluation, FREAK is even faster than BRISK, and it is faster of two orders of magnitude than SIFT and SURF with [80].

Features from Accelerated Segment Test (FAST)

FAST is a high-performance tracking system based on the combination of two different tracking systems with complementary behavior and very different statistics. FAST is a feature detector relying on five main steps as follows [81][82]:

- Selecting a pixel (P) on an image with intensity I_p ,

- Threshold selection (*t*),
- Consider a circle of 16 pixels around the considered pixel (see Figure 2.22),
- Pixel *P* is a corner if *n* adjacent pixels (usually 12 pixels) in the circle are brighter than I_p+t or darker than I_p-t,
- Apply a high-speed test to remove non-corners based on the pixels at 1, 9, 5 and 13

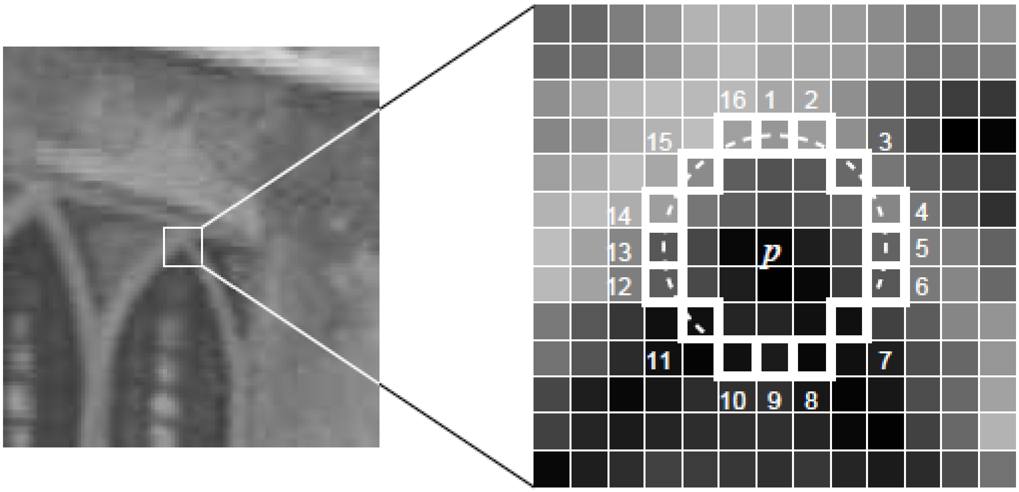

Figure 2.22 : Test corner detection using 12 points for the *P* pixel candidate. The highlighted pixel crossed covered by the circle is used for the corner detection [82].

The three first bullet points are addressed by using a machine-learning algorithm, and the last one by Non-maximal suppression. Although FAST is faster than the other algorithms, its counterparts are threshold-dependent and sensitivity to noise [82].

2.8.2. Featured-tracking based algorithms (blob-based feature detector and descriptor)

Speeded Up Robust Features (SURF)

SURF is a novel scale- and rotation-invariant interest point detector and descriptor. operates integral images at (x,y) (2.61) for image convolution based on the strengths of sophisticated existing detectors and descriptors. SURF uses the Hessian matrix as detector due to its good performance in terms of computation time and accuracy to determine the location and scale. Taking a point x=(x, y) in an image *I*, the Hessian matrix $H(x,\sigma)$ in x at scale σ is given by [83]:

$$I_{\Sigma}(x,y)=\sum_{i=0}^{i\le x}\sum_{j=0}^{j\le y} I(i,j) \tag{2.61}$$

$$H(x,\sigma) = \begin{bmatrix} L_{xx}(x,\sigma) & L_{xy}(x,\sigma) \\ L_{xy}(x,\sigma) & L_{yy}(x,\sigma) \end{bmatrix} \tag{2.62}$$

where $L_{xx}(x, \sigma)$ is the convolution of the Gaussian second order derivative. SURF then approximates Laplacian of Gaussian (LoG) with a Box filter (see Figure 2.23).

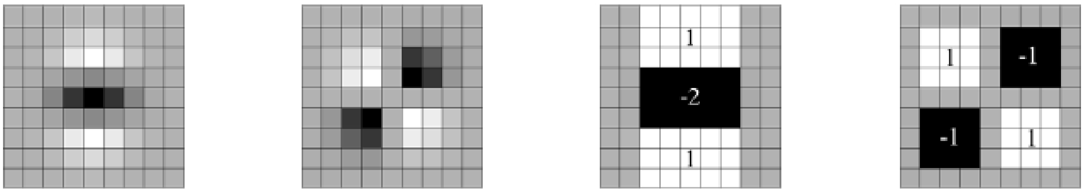

Figure 2.23 : Gaussian second order partial derivatives in y-direction and xy-direction, and the approximations using box filters (the grey parts are zero) [83].

SURF relies on two main steps: i) orientation assignment and ii) SURF descriptor. The first step is defined a reproducible orientation based on information from a circular region around the interest point using wavelet responses in horizontal and vertical direction for a contiguous of size 6s. The SURF descriptor uses the same orientation assignment with a contiguous of size 20s×20s surrounding the keypoint divided into 4×4 sub-regions and x-y wavelet response leads to vector of $v = (\sum dx, \sum dy, \sum|dx|, \sum|dy|)$ [83] (see Figure 2.24).

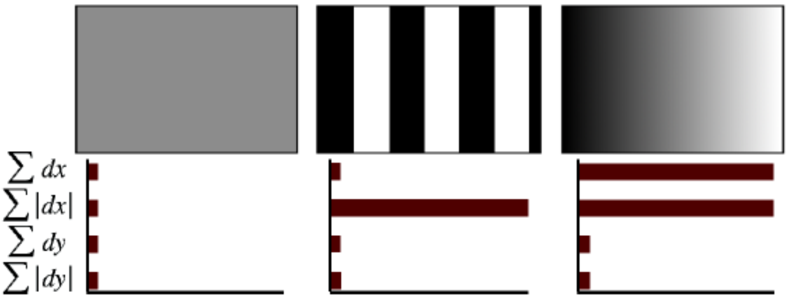

Figure 2.24 : Descriptor of sub-regions depicts the underlying intensity pattern. Left: homogeneous region (low values). Middle: spatial changes in x direction (the value of $\sum|dx|$ is high and the rest is low). If intensity is gradually rising up in x direction, both $\sum|dx|$ and $\sum dx$ are high. SURF performance in terms of repeatability, distinctiveness, and robustness, speed and accuracy outperforms other existing state-of the art methods [83].

FAST presents a fast and performant interest point detection-description scheme which outperforms the current state-of-the art, both in speed and accuracy. The descriptor is easily extendable for the description of affine invariant regions [83].

Chapter 3

3. ACCURACY IMPROVEMENT OF OFFSET TRACKING ESTIMATION ON SAR DATA

The aim of this chapter[1] *is to provide an analysis of the capability of DInSAR techniques (i.e., PSI), Multi-Aperture Interferometry (MAI) and offset tracking techniques to monitor landslides and improve displacement accuracy using COSMO-SkyMed data. 27 COSMO-SkyMed StripMap (HIMAGE) data were selected in the descending orbit mode, which cover a period of 464 days (i.e., between 5 April 2014 and 10 August 2015). All the phase and intensity-based techniques are applied to the 16 Corner Reflectors (CR) specifically designed for X-band and installed on the Corvara landslide which are used as reference points for DInSAR and sub-pixel offset tracking. Each CR has been equipped by a GPS antenna for validation purposes. Finally, a sensitivity analysis of these techniques applied to CSK data provides indications on advantages and disadvantages of each of them.*

3.1 Introduction

Mountainous areas are recurrently affected by active instability processes, such as debris flows or landslides that can induce damages and casualties. To reduce the risks, a careful assessment and monitoring of slope deformations is required. Over the past two decades, capabilities of synthetic aperture radar interferometry (InSAR) have been demonstrated to detect and quantify land surface deformations with a precision in the order of millimeters.

MAI technique, considered as a version of SD in azimuth, operates on the split-beam of InSAR using band pass filters into the forward- and backward-looking interferograms. It was developed for long-track deformation retrieval [61]. Since the forward- and backward-looking interferograms are geometrically symmetric, the range and troposphere components

---

[1] Part of this chapter appears in:

[138] M. Darvishi, R. Schlögel, L. Bruzzone, and G. Cuozzo, "Integration of PSI, MAI, and intensity-based sub-pixel offset tracking results for landslide monitoring with X-band corner reflectors-Italian Alps (Corvara)," *Remote Sens.*, vol. 10, no. 3, 2018.

will nearly appear the same. As a result, the tropospheric phase contribution can be removed from the interferograms.

In offset tracking-based methods, CCC relies on using the complex image patches and can be applied to coherent data even without any tangible and traceable scatterer. It uses cross-correlation operation as an optimum (maximum-likelihood) estimator (MLE) for offset determination of partially correlated circular Gaussian signals and some systematic (non-noise) phase differences such as topographic and flat-earth fringes [65]. CCC operates on the formation of small interferograms involving some changes in range and azimuth, the offsets is specified by detecting the peak average coherence [84]. Contrary to CCC, ICC only relies on amplitude information of image patches and attempts to find offset between traceable features (e.g., lines and rocks). It uses cross-correlation of intensity of SLC data and finds the peak location to estimate offset.

Template matching algorithms are widely used for image registration and feature matching. Generally, template matching algorithms can be classified into three groups [67]: (i) featured-based algorithms that are well suited to extract the features using their spatial relations or descriptors; (ii) patch or area-based algorithms that consider the intensity of the pixel values obtained after cross-correlation-based similarity; and (iii) optical-flow or motion tracking algorithms. The first group is mainly appropriate to match structural information (i.e., features), the second one fits for intensity information and the third one is based on the relation between photometric correspondence vectors and spatiotemporal derivatives of luminance in an image sequence [68].

Feature matching enables finding correspondences between two images based on the local interest points. It plays a key role in computer vision applications such as motion estimation, image registration, object detection and tracking. Feature-based matching procedures rely on local feature detection (mainly based on gradient or intensity variation) and corresponding feature descriptors (local image gradient). The local features are usually blobs, corners or edge pixels that are extracted by an appropriate feature detection algorithm. Efficiently matching features across images is the core of feature-based algorithms in computer vison. Repeatability, distinctiveness and localization of features are the three main characteristics of a good local feature under varying imaging condition and in the presence of noise [85]. Localization refers to how well a detector can locate the exact position of features. Binary Robust Invariant Scalable Keypoints (BRISK) [75], Minimum eigenvalue algorithm (MEIGEN) [76], Harris [79], Features from Accelerated Segment Test (FAST) [82] and Fast Retina Keypoint (FREAK) are often used as corner-based feature detection functions and descriptors. Speeded Up Robust Features (SUR) [83] and Scale Invariant Feature Transform (SIFT) [86] are the most significant blob-based features descriptors in computer vision field. The descriptors of the corner-based features are mainly based on pairs of local intensity differences (e.g., BRISK) while the descriptors of the blob-based features (e.g., SURF and SIFT) are based on local gradient. The use of computer vision-based algorithms has not been widely investigated with SAR data except for the task of image registration [33,34].

This research aims to improve the accuracy of offset estimation using computer vision techniques, and integrate the PSI, MAI, and offset tracking results to monitor a complex and vegetated landslide through X-band CRs. This allows us to overcome or mitigate the limitations of some methods. PSI is limited only to 1D LOS displacement detection and an upper limit for velocity estimation. Non-LOS displacements are not also retrievable by PSI, in such case; MAI could be considered as an alternative technique to overcome this limitation. High movement rate leads to phase aliasing in the CCC-based methods and dependency of offset estimation accuracy on data pixel size and changes in the features (e.g., geometrical distortions) are the main constraints of the ICC-based methods. Low coherence problem in vegetated areas, leading to phase unwrapping difficulty, can be tackled by using artificial CR.

3.2 Case Study and Dataset

Corvara Landslide

The case study is the active Corvara landslide, located in the Autonomous Province of Bolzano-South Tyrol, in the Italian Alps. It is described as a slow-moving complex earth slide-earth flow with annual displacement rates of up to 20 m [35,36] (see Figure 3.1c,d). The ongoing slope deformation is in the order of a few cm/year in the toe zone, and up to tens of meters per year in the most active track and source zones. Since the Corvara is among the most popular tourist attractions in the Italian Alps, the area has undergone an intense tourist development. The urban settlement has progressively increased since the late 1960s, and a dense network of facilities now serves most of the slopes. This development has significantly increased both the wealth of the area and risk to slope failures [91]. This landslide frequently causes damages to the national road SS 244, the ski infrastructures, and the nearby golf course.

The landslide behavior is characterized such as: retrogressive at the crown and flanks of the source areas; slightly enlarging at the sides of the accumulation area; slightly advancing at the turn of the landslide into the main valley; and potentially advancing at the toe [92]. The Corvara landslide has been monitored for several years with different close and far range imagery techniques such as Unmanned Aerial Vehicle (UAVs) [93], SAR data [90] and by multi-sensors data integration [94].

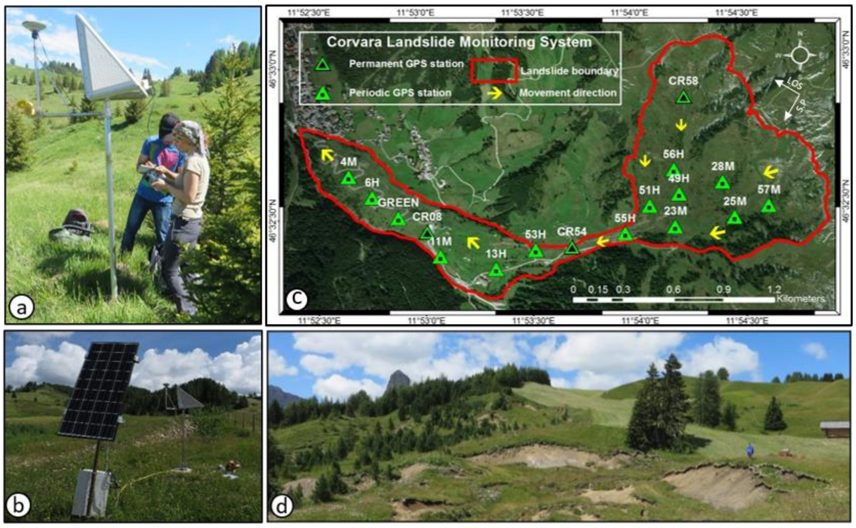

Figure 3.1: Corvara landslide monitoring system. (a) Periodic GPS measurements (monthly); (b) Permanent GPS station fed by solar panel; (c) Corvara landslide extent, its movement direction and CRs locations corresponding to the GPS network and (d) Active landslide depletion area (close to CR58).

3.3 Artificial Corner Reflectors

In 2013, 16 Corner Reflectors (CR) specifically designed [95] for X-band were installed on the landslide and used as reference points for InSAR and sub-pixel offset tracking (Figure 3.2). Each CR was equipped with an antenna stand with a GPS station to take monthly and hourly (Figure 3.2a) 3D measurements. The reflector consists of a trihedral built of aluminum plates with a side length of 56 cm. The plates are connected via screws resulting in a more accurate geometry than for welded plates. Each of the faces is perforated with evenly spaced 3 mm holes for reducing the weight, wind resistance and the tendency for water and snow accumulation (Figure 3.3b-c). The entire CR can be dissembled and carried by one person (Figure 3.3a). For installation in rock, concrete or ice, the single pole is screwed to the ground (Figure 3.3d); for soft ground and earth a concrete foundation ensures stable positioning (Figure 3.3h). Assembling the CR in the field requires basic tools, and orientation according to the satellite orbits can easily be obtained (Figure 3.3e). The extension behind the trihedral reflector can accommodate a GNSS antenna for validation measurements (Figure 3.3f illustrates a permanent GPS station on Corvara landslide). Other methods, e.g. total station measurements (Figure 3.3g) can also be facilitated. The CR have been built by a company in Bolzano and the cost per unit was approximately 1000 EUR. From the CRs distribution perspective over the landslide, due to the limitation in the number of the available CRs, the priority was dedicated to the active and semi-active part of the landslide with the movement directions aligned to LOS. Thereby, it was avoided installing the CRs on a landslide part where was not regarded as an active area (according to the GPS observations) with a non-

LOS movement (e.g., surrounding CR58). GPS measurements and SAR results show different motion behaviors in terms of direction and velocity rate. The PSI technique was not able to track the high velocity rate CRs and was not considered in past processing [90]. In this work, we analyze two different motion categories (i.e., high and low velocity rates) both in LOS and non-LOS directions. If the displacement of a CR is higher than 0.5 m (within the data time span), it is of “high velocity rate”, while CR displacements less than 0.5 m are of “low velocity rate” (see Table 3.1). If the azimuth displacement of a CR derived by GPS locates within the ±25° of the Azimuth LOS (ALOS) of the satellite (i.e., 280°), it is placed into the sub-group of “LOS direction”; otherwise it is labeled as non-LOS direction category. Table 3.1 shows the GPS measurements of 16 CRs corresponding to the satellite images. The high velocity rate CRs are processed and analyzed using offset tracking-based methods, while the low velocity rate CRs with displacements in the LOS alignment are processed using InSAR-based method (i.e., PSI). Since the CR58 displacement is less than 0.5 m according to nearly the North-South direction, it is processed using the MAI. The GPS data used here as ground truth for validating the results are described in [90].

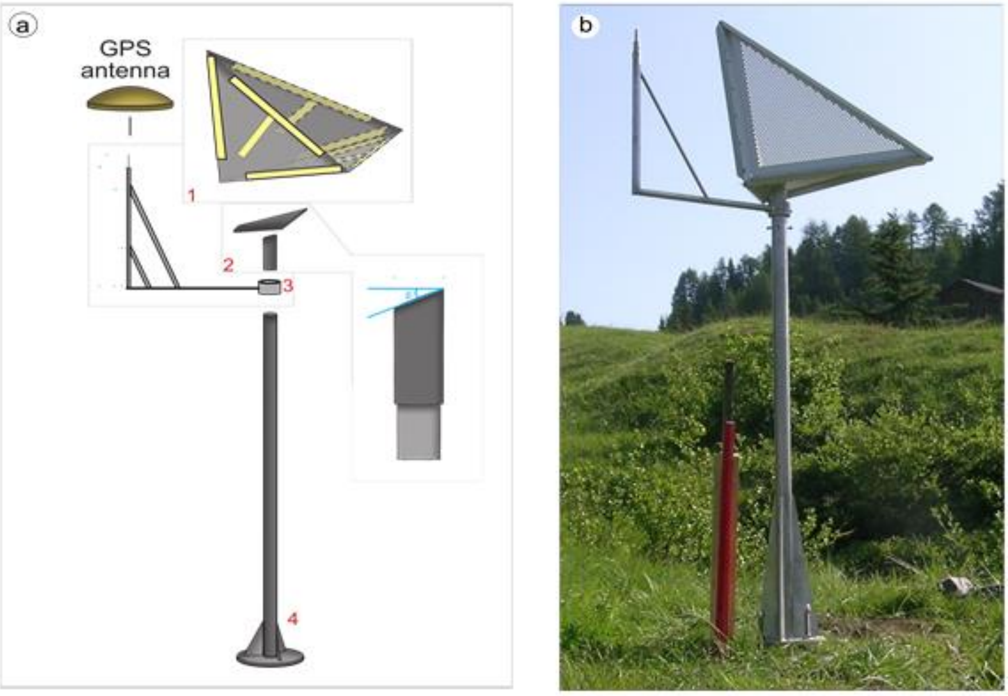

Figure 3.2 : Corner reflectors deployed on the Corvara landslide. (a) design and (b) photo from the field.

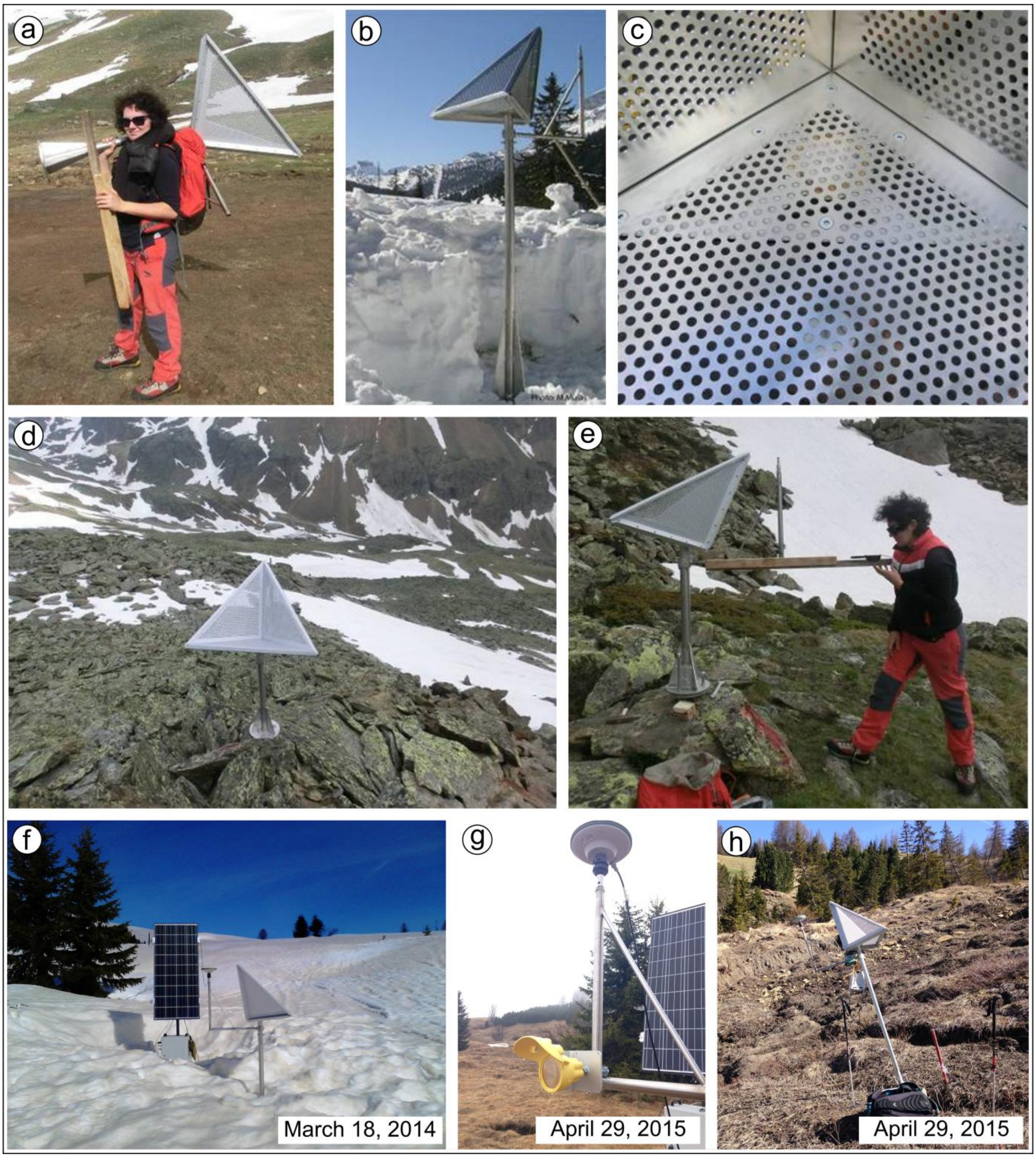

Figure 3.3 : Features of the CRs and field applications.

Table 3.1: High and low velocity rate CRs including both LOS and non-LOS directions.

Velocity Rate Type	Displacement Direction	CR No.	Magnitude of Displacement	Azimuth of Displacement
High velocity rate CRs	LOS direction	CR53	1.69 m	272°
		CR54	3.41 m	284°
	Non-LOS direction	CR51	39.95 m	171°
		CR55	46.17 m	250°
		CR56	3.57 m	167°
Low velocity rate CRs	LOS direction	CR4	12.5 cm	305°
		CR6	13.3 cm	303°
		CR8	32 cm	283°
		CR11	20.7 cm	298°
		CR13	39.1 cm	270°
		CR23	22.7 cm	260°
		CR25	20.1 cm	260°
		CR57	18.3 cm	265°
		CR28	39.1 cm	260°
		CR49	20.3 cm	265°
	Non-LOS direction	CR58	34 cm	177°

3.3.1 Dataset

The 27 COSMO-SkyMed data selected, whose charcteristics are described in Table 3.2, covering a time span of 464 days (i.e., between 5 April 2014 and 10 August 2015).

Table 3.2 Sentinel-1 data specification. The following acronyms were used in the table: polarization (Pol), incident (Inc), azimuth (track) (Az), revisit time (Rtime), range (Rg), and wavelength (W.L.).

Product Type	**Mode**	**Pass**	**Pol.**	**Inc/Az angle**	**Rtime**	**Rg × Az spacing**	**W.L.**
StripMap	HIMAGE	Descending	VV	42°/185°	16 day	1.5 m × 1.9 m	3.1 cm

Two DEMs were available for the Corvara area: (i) SRTM DEM (30 m) in 2000; and (ii) laser airborne DEM (2.5 m) acquired in 2006 by the autonomous Province of Bolzano. The airborne DEM was used in the InSAR processing, because it is more recent and has a finer resolution than SRTM DEM.

3.4 Maximum Detectable LOS Displacement

To estimate the CRs displacements several considerations must be considered in the InSAR processing. To have a reliable phase unwrapping, the unmolded phase such as atmospheric contribution must be smaller than 0.6 rad, meaning that PS pixels density must be more than 3–4 per km^2, for common atmospheric conditions [96]. To consider this PS range constraint, especially for vegetated landslides, artificial corner reflectors can be used as PSs to fill the gap between the PSs network. In addition to the above-mentioned limitations, the deformation phase cannot be retrieved unambiguously when the displacement phase between two successive acquisitions goes beyond $\pm\pi$ [21], which refers to the Maximum Detectable LOS Displacement (MDLD) (3.1). The MDLD of each adjacent pixel in a wrapped interferogram and during the phase unwrapping cannot exceed $\lambda/2$ and $\lambda/4$ (less than 0.5

interferometric fringes per pixel), respectively (3.2) [43,44]. Therefore, the maximum range of displacement rate can be theoretically defined either in terms of wavelength-revisit time or in terms of wavelength-pixel size of SAR data:

$$\Delta D_{\max} = \frac{\lambda/4}{\Delta T/365.25} \tag{3.1}$$

$$D_{\max} = \frac{\lambda}{2sp} \tag{3.2}$$

where ΔT, λ and sp indicate the time interval of two successive acquisitions, the sensor wavelength and the pixel size of the SAR image, respectively. Based on (3.1), the theoretical MDLD rates for TerraSAR-x with revisit time of 11 days, COSMO-SkyMed with the nominal repeat cycle of 16 days and Sentinel-1A/B with revisit of 6 days are 25.7 cm/year, 17.6 cm/year and 85.2 cm/year, respectively. According to (3.2), the MDLD for TerraSAR-X (pixel size: 1 m × 1 m with 1 look), COSMO-SkyMed (pixel size: 2 m × 2 m with 1 look) and Sentinel-1A/B (pixel size 13 m × 13 m with 1 × 4 looks) will be 1.55×10^{-2}, 7.75×10^{-3} and 2.1×10^{-3}, respectively. The MDLD upper limit does not consider the noise caused by the various decorrelation sources.

Data Pre-Processing

Before starting data processing, we first performed a quality assessment analysis on the CR footprints. In fact, knowing the quality and evolution of the CR signals over the time span is useful to interpret InSAR results. Then, we prepared the data for offset tracking processing.

3.5 CR Response Quality Assessment

When a SAR system response to a CR is reliable and stable (intensity and phase) in the time series, the CR orientation (i.e., azimuth and elevation angles) has been properly aligned toward the satellite. The Impulse Response Function (IRF) characteristic of a received signal is a significant indicator for data quality check. If a CR has been installed optimally, the footprint of a CR on a SAR image should show a cross-like shape and its IRF should be similar to an ideal IRF (i.e., a Sinc function, see Figure 3.4d). Several parameters can determine the quality of the SAR response to a CR including: (i) the Peak Side Lobe Ratio (PSLR) refers to the ratio between the peak elevation of the side lobe (I_s) and the peak elevation of the main lobe (I_m); and (ii) the Integrated Side Lobe Ratio (ISLR) indicates the ratio between the power in the main lobe and the total power in all the side lobes. In Figure 2d, the area below the 3 dB intensity points in the main lobe specifies Spatial Resolution (SR) of SAR data. Table 3.3 lists the PSLR in range and azimuth (i.e., RPLSR and APSLR) and the ISLR for each CR extracted. As an example, we show the IRF and intensity value of CR13 providing the highest backscattering signal (see Figure 3.4a–c). This quality check procedure helps in understanding whether the CRs have been tilted by the landslide movement or not. If so, the CR orientation changes could considerably influence InSAR and offset tracking results.

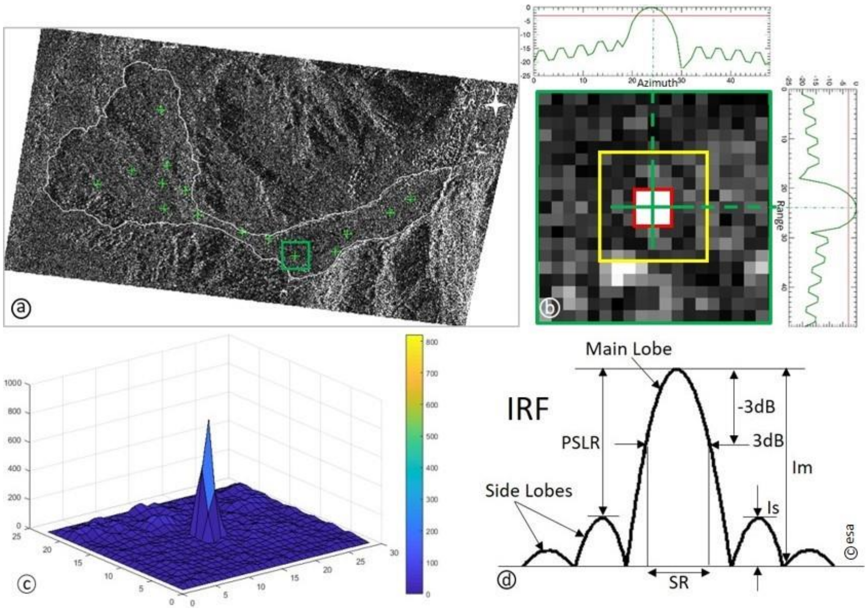

Figure 3.4: The SAR response to CR13 and IRF extraction. (a) Intensity of Single Look Complex (SLC) data in SAR geometry with the location of CRs (green crosses) and the CR13 position (green square); (b) Zoom view of the green box containing the CR13 footprint (red square) and its corresponding IRF (the red line refers to −3 dB value) in the range/azimuth direction (dB unit), the clutter region (the area between yellow and the red squares); (c) Intensity peak of the CR13 in 3D and (d) Ideal IRF with the related parameters.

Table 3.3: CRs impulse response changes from the first and the last acquisitions. The related IRF parameters of all CRs derived from 5 April 2014 and 8 October 2015. Backscattering (Bsc) values of the CRs were directly extracted from the center of CRs footprints on the SLC data.

CR No.	**CSK-05 April 2014**				**CSK-08 October 2015**			
	Bsc	RPSLR (dB)	APSLR (dB)	ISLR (dB)	Bsc	RPSLR (dB)	APSLR (dB)	ISLR (dB)
CR4	**502**	**−11**	**−11.1**	**0.72**	**743**	**−9.9**	**−10.6**	**1.67**
CR6	**473**	**−10.8**	**−9.9**	**0.54**	**654**	**−11.1**	**−10**	**1.55**
CR8	**574**	**−10.8**	**−10.2**	**1.4**	**677**	**−10.2**	**−9.9**	**1.52**
CR11	**462**	**−10.3**	**−10.8**	**0.39**	**475**	**−9.7**	**−10.7**	**1.51**
CR13	**453**	**−10.2**	**−12.2**	**0.47**	**821**	**−10.1**	**−12.1**	**1.44**
CR23	**435**	**−10.9**	**−10.2**	**0.46**	**668**	**−10.8**	**−10.1**	**1.57**
CR25	**518**	**−9.7**	**11.6**	**1.43**	**631**	**−10.4**	**−11.5**	**0.76**
CR28	**443**	**−9.8**	**−11**	**0.48**	**654**	**−9.7**	**−10.6**	**1.6**
CR49	**486**	**−11.2**	**−11.2**	**0.5**	**741**	**−10.2**	**−11.1**	**1.46**
CR51	**492**	**−11**	**−11**	**0.53**	**413**	**−12**	**−9.1**	**1.93**
CR53	**426**	**−10.4**	**−10.5**	**1.66**	**831**	**−10.3**	**−11.7**	**1.74**
CR54	**512**	**−10.8**	**−12.6**	**1.87**	**671**	**−11.9**	**−16.6**	**−0.52**
CR55	**464**	**−11.2**	**−11.5**	**0.51**	**635**	**−10.1**	**−10**	**1.69**
CR56	**499**	**−11.1**	**−10.1**	**1.44**	**580**	**−10.1**	**−11.1**	**1.18**
CR57	**525**	**−10.1**	**−11.2**	**1.35**	**600**	**−9.8**	**−10.1**	**1.6**
CR58	**476**	**−10.2**	**−11.1**	**0.37**	**746**	**−10.1**	**−10.6**	**1.67**

Data Pre-Processing

The data pre-processing was performed in two steps to use the intensity information of CSK data for offset tracking processing. First, the data were calibrated into the sigma naught (i.e., backscatter coefficients) and then georeferenced in the UTM coordinate system. To reduce the speckle, the Anisotropic Non-Linear Diffusion (ANLD) filter was applied to both images considering Gaussian blur kernel variance equal to 0.5, anisotropy equal to 5, and step size equal to 100. Attention was paid to avoid truncating high intensity values of the image pixels to a fixed value in the calibration step. Pixels with a high sigma naught are truncated to 5 in SARscape software [99]. If that happens, the CR footprints will have several pixels with identical values (i.e., 5) that affect offset estimation at the sub-pixel level. It should be noted that the aforementioned pre-processing has been applied only to the OT processing, whereas for the InSAR processing the SAR data were analyzed by the SAR geometry (slant range).

3.6 Methodology

The low velocity rate CRs corresponding to displacements in the MDLD range were processed using the PSI and MAI (only CR58) techniques over the time series. The high velocity rate CRs having displacements beyond the MDLD range were processed by offset tracking-based techniques. To investigate the performance of different offset tracking techniques several matching algorithms (i.e., area and feature-based matching methods) were applied to one CSK pair according to the first and last acquisition dates. This aims to estimate the CRs offsets between these two SAR images.

The area-based matching algorithms investigated in this study are (1) the Phase Correlation (PC); (2) the Modified PC (MPC) implemented by ImGRAFT [100] and COSI-Corr [47,48], respectively; (3) the Orientation Correlation (OC) implemented by ImGRAFT and CIAS [49,50], concurrently; and (4) the NCC and Statistical Correlation (SC) implemented by CIAS and COSI-Corr. In addition, the feature-based matching algorithms taken from computer vision are as follows: (1) BRISK (FREAK as descriptor); (2) HARRIS; (3) MEIGEN; (4) FAST; (5) SURF; (6) the combination of BRISK, HARRIS and MEIGEN detectors with SURF as a descriptor. All feature-based matching algorithms were implemented in MATLAB [104]. Although OC is practically a feature-based algorithm, we put it in the area-based matching category, because it uses a correlation operator for matching and a moving window-based approach. The methodology flowchart is divided into two branches according to the landslide velocity rate and the related methods for estimating it (see Figure 3.5).

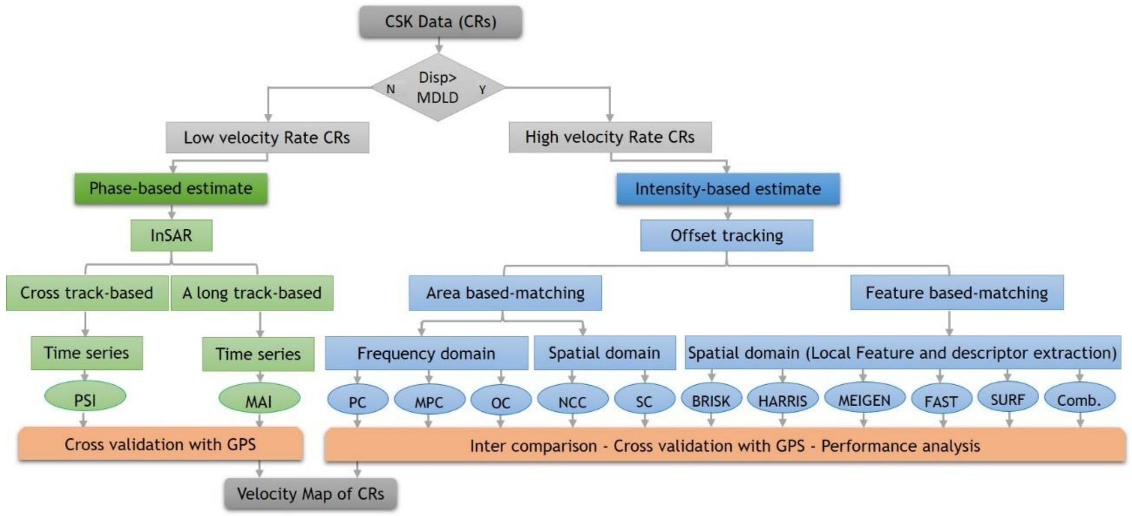

Figure 3.5 : Methodological flowchart including InSAR-based and offset tracking-based techniques in addition to the validation. Comb. refers to the combination of the corner-based feature detection functions (i.e., BRISK, HARRIS and MEIGEN) with the SURF descriptor.

3.6.1 Phase-Based Estimation (InSAR - PSI)

To overcome the decorrelation problem due to the vegetation observed on the Corvara landslide, the PSI technique has been applied to the installed CRs. The main goal of PSI processing is the extraction of the phase displacement component without any other residual phase components especially the noise. Figure 3.6 shows the SAR data pairs combination and connection graph with 27 CSK images as well as the rainfall data taken from the Piz la Ila station.

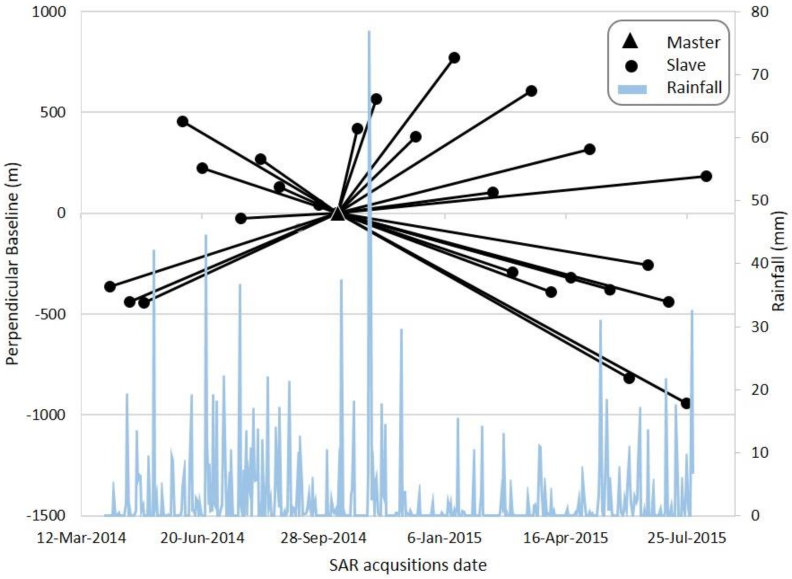

Figure 3.6 : Perpendicular and temporal baseline information of the CSK acquisitions according to the master image and daily precipitations measured at the Piz la Ila rain gauge station nearby Corvara.

The master and slaves chosen according to (2.17). The minimum and maximum perpendicular baselines are of 42 m and 976 m, respectively to the master image, which are smaller than the critical baseline.

The PSI processing [105] was run with the SARscape software following five steps: (1) single master connection network creation; (2) images co-registration, interferogram generation and flattening; (3) first inversion; (4) second inversion and (5) displacement geocoding. First, all slaves are co-registered to the master image with an oversampling factor of 4 in range to avoid aliasing. None of Doppler separation of each slave and master was beyond the critical f_{dc}, hence, no Doppler filtering was applied. Since the perpendicular baselines of all pairs are much lower than the critical baseline (45% of the critical baseline), the spatial decorrelation is very limited. No spectral filtering is applied in order to keep the data at the highest resolution possible and increasing pixel probability to be dominated by one scatterer [106]. Initial PS pixels selection was performed by using the ratio of the standard deviation to its intensity average, known as the amplitude dispersion index (D_{A}). In the first inversion step, the residual height and displacement velocity were obtained by considering the reliability of phase history of selected PS pixels using the linear model. The phase offset retrieved from the interferograms was removed using the highest coherent pixel selected within a predefined area (5 sqkm) as a reference point. The second inversion estimated the atmospheric phase components by using the previous model and the second linear model to fit the final displacement after removing the atmospheric phase. Low and high band pass filtering with window sizes of 1000 and 365 (days) were then applied to remove the spatial and temporal distributions of the atmospheric variations.

In the validation step, the GPS measurements have been projected into the LOS direction to be compared with PSI results.

3.6.2 Phase-Based Estimation (InSAR - MAI)

MAI is an advanced InSAR technique based on the split-beam of InSAR processing using a modification of the Doppler centroid into forward (φ_f) and backward (φ_b) looking interferograms [61]. The resultant phase difference between two SAR pairs can be used for estimating a long-track displacement. The MAI phase (3.7) and its accuracy (3.8) are defined as:

$$\varphi_{MAI} = \varphi_{InSAR,f} - \varphi_{InSAR,b} = \frac{4\pi n}{l} \Delta r \tag{3.7}$$

$$\sigma_{MAI} = \frac{4\pi n}{l} \sigma_{\Delta r} \tag{3.8}$$

where l is the length of the antenna, n is a normalized squint (fraction of the full aperture width), $\sigma_{\Delta r}$ and σ_{MAI} are the standard deviations of the phase and displacement measurements, respectively [20,21]. Since the movement direction of the CR58 is approximately aligned to the azimuthal direction (nearly N–S) with a magnitude of about 34 cm, for reducing the computational load of the data processing, MAI was applied to half of the SAR data over the full time series. Moreover, different multi-looking factors (4 × 4, 16 × 16 and 64 × 64) and n parameters (i.e., 1/2 and 1/4) were tested.

3.6.3 Intensity-Based Estimation (offset tracking - area-based)

Phase Correlation (PC)

Image matching can be performed in the frequency domain referring to phase correlation. Two PC versions were applied to the intensity-based SAR images: (i) the standard PC; and (ii) a modified version of PC (MPC). MPC minimizes the weighted residual matrix between the computed normalized cross-spectrum and the theoretical one to both reach more flexibility on the frequency weighting and to solve the phase wrapping ambiguity. It uses an iterative process (re-computing times of frequency mask adaptively) to increase the robustness and accuracy, and frequency masking to obtain a bias-free correlation [73]. The robustness iteration and mask threshold parameters are firstly set to 2 and 0.9, respectively. To investigate the role of the robustness iteration parameter in accuracy improvement of the offset estimation, its value is then increased to 4 by a resampling process.

Orientation Correlation (OC)

OC is a template-matching algorithm in the featured-based matching category and relies on orientation of image intensity gradients [74]. The orientation images are then matched using inverse FFT-based correlation. Since Orientation Intensity Of Gradient on the images has no gradient (i.e., 0 + 0*i*) for uniform regions and is equal to 1, hence, OC is invariant to offset illumination changes [74].

Normalized Cross Correlation (NCC)

NCC is a robust and simple method to seek for a particular pattern that has probably been shifted in two subsequent (in time) images to find the related offset. NCC algorithm was applied to one SAR pair using CIAS and COSI-Corr. SC in COSI-Corr uses the statistical approach based on the cross correlation. To evaluate the effect of using different templates and search windows on the accuracy of the offset estimation, several windows were defined based on an initial guess of the CRs displacements (i.e., with 64 × 64, 32 × 32 and 16 × 16 search windows, 16 × 16 and 8 × 8 template windows and according to 2, 4 and 8 pixels during the moving window step). This procedure is used for each area-based estimator.

3.6.4 Intensity-Based Estimation (offset tracking - feature-based)

Generally, the BRISK algorithm includes three main parts: (i) sampling pattern; (ii) orientation compensation; and (iii) sampling pairs [75]. The features in BRISK are extracted in octave layers and layers in-between of the image pyramid, and then the location and the scale of each feature is acquired in the continuous domain via quadratic function fitting [75]. The BRISK descriptor uses Hamming distance instead of Euclidean distance to match features utilizing the sum of XOR operation between two binary descriptors [75]. HARRIS operates on the second moment matrix (auto-correlation matrix) to detect the features using the gradient distribution in a local vicinity of a point-like target [79]. MEIGEN is a feature detector that extracts the point feature using a measure of feature dissimilarity to quantify the changes between two images [76]. FAST detector uses comparing of pixels where those have only been located on a circle of fixed radius around the point (i.e., 16 pixels) to consider the object as a corner candidate [82]. SURF detector considers integral images for image convolutions and Fast-Hessian matrix. The SURF descriptor is based on dividing the neighborhood region of each feature into sub-square regions (i.e., 4 × 4) and then calculating the response of a 2-dimenssions Haar wavelet for each sub-region [83]. FREAK, as a binary descriptor, was also used by the BRISK detector for describing the detected BRISK-based features. FREAK is a cascade of binary strings computed by efficiently comparing image intensities over a retinal sampling pattern [80]. To utilize the high capability of SURF in localization, four corner-based detectors (i.e., BRISK, HARRIS, MEIGEN FAST) were combined with the SURF descriptor in the feature matching step. In this way, the improvement potential of the offset estimation accuracy could be investigated and compared with the previous status (i.e., the corner-based algorithms as either detector or descriptor). The set of parameters for the feature detection function were presented in Table 3.4.

Table 3.4: Set of parameters used for the processing of the feature detection functions and descriptors.

Parameters	BRISK	HARRIS	MEIGEN	FAST	SURF
Minimum intensity *	0.2	-	-	-	0.2
Minimum quality	0.1	0.01	0.01	0.1	-
Gaussian filter size		5	5	-	-
Number of octaves	4	-	-	-	4
Number of scale **	-	-	-	-	4

* Minimum intensity difference between corner and surrounding region. ** Number of scale levels per octave.

3.7 Results

3.7.1 InSAR results (PSI and MAI)

The PSI accumulative displacement is represented in Figure 6. In the plots, the GPS measurements are projected to the LOS for the PSI results and to the satellite azimuth for the MAI results using (3.7) and (3.8), respectively. As GPS measurements were not acquired exactly at the same time (i.e., there were few days of difference) that the CSK acquisitions, the GPS measurements were approximated by a linear curve to make them comparable with the PSI results. The goodness of fit parameter (i.e., the R-square) for each fitted line is reported in Table 3.5. Figure 3.7 shows that the deviation of the PSI results from the GPS line varies for each CR. CR6, 23 and 57 present a variable agreement, CR4, 13, 28, 25 and 49 have a moderate agreement, and CR8 and 11 have a good agreement with the GPS measurements.

The PSI and MAI results (including comparison of the velocity rates between PS, MAI and GPS, and accuracy assessment) are presented in Table 3.5. The Multi-temporal coherence (M_c) parameter shows how well a CR displacement trend fits with the linear model that was already selected for PSI processing. More M_c is close to 1 value, more the related PSI results fit the linear model. According to Table 3.5, CR8 and 11 presented the lowest Standard deviation (Std) and RMSE among the other CRs, and CR28, 49, 25, 23 and 57 (which are in the most active part of the landslide with different displacements in azimuth with respect to the LOS) presented the highest Std and RMS. The CR6 and CR28 provided the minimum (8 cm/year) and maximum (28 cm/year) velocity rates, respectively. The displacement of CR58 was the only one derived by MAI and the displacements of the high velocity rate CRs cannot be estimated by MAI due to the MDLD restriction.

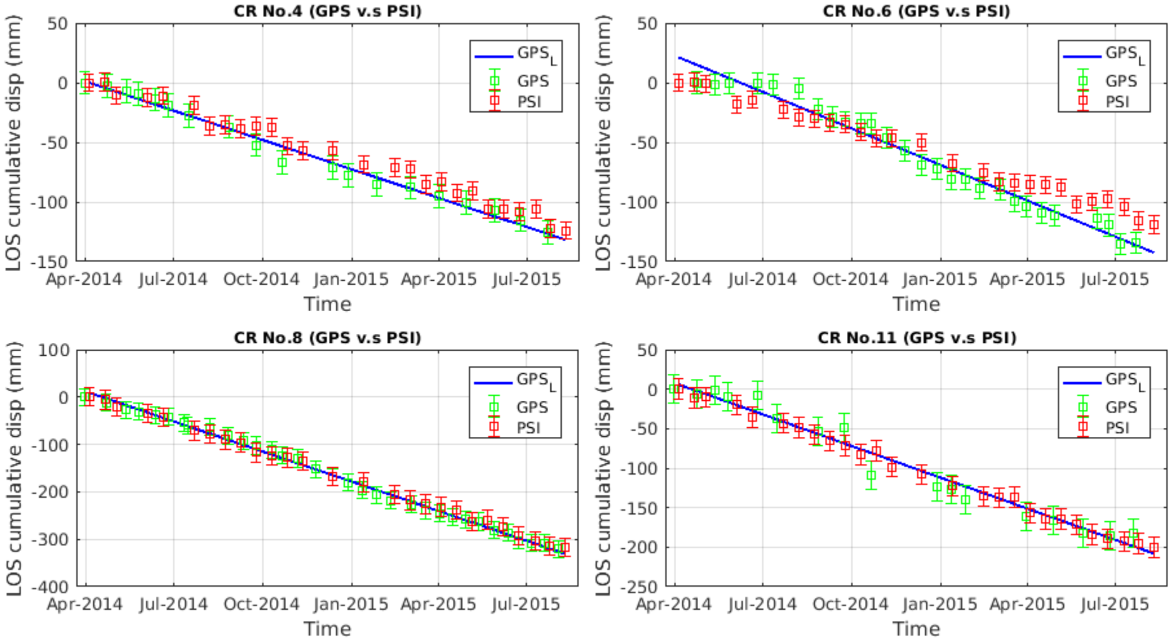

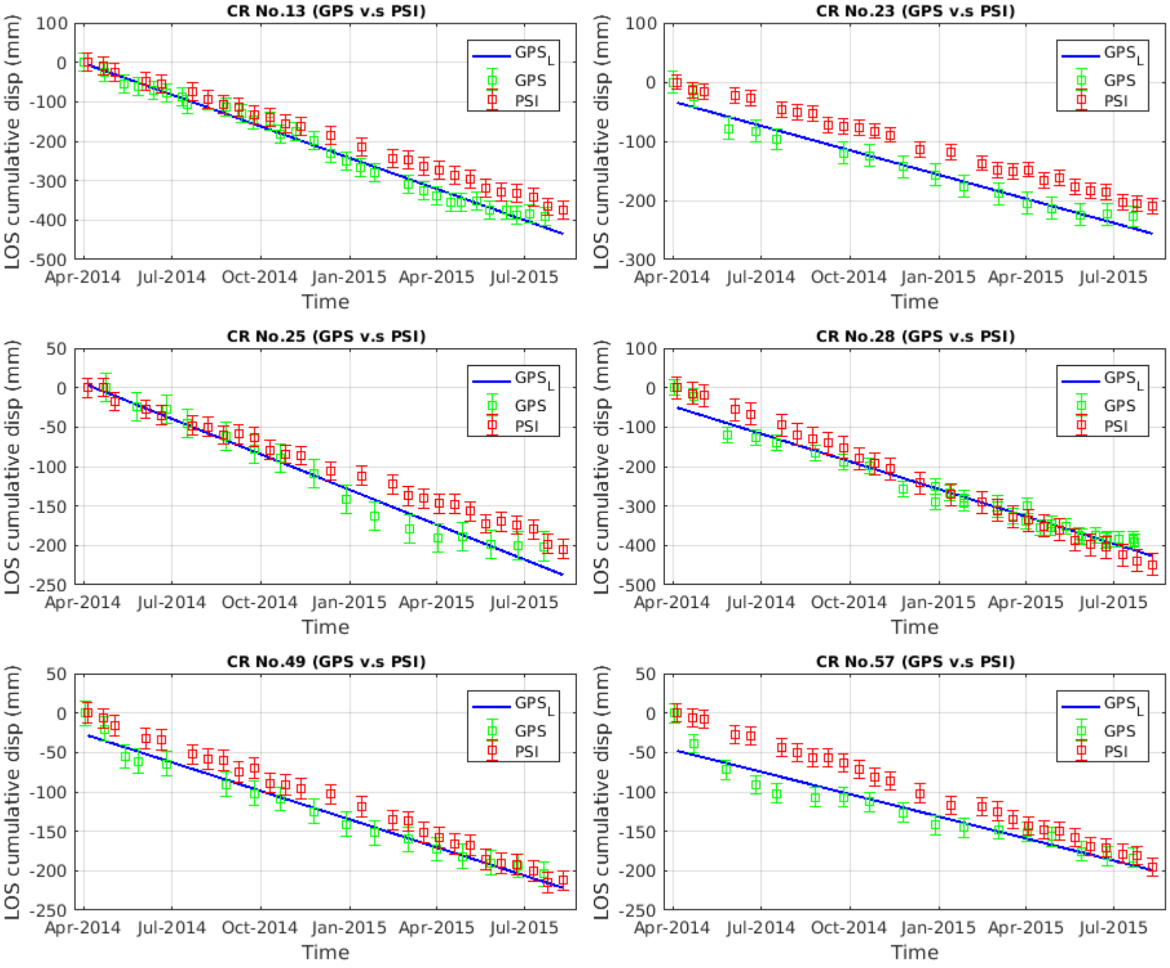

Figure 3.7 : Cumulative displacement plot for each CR. The CR labels are mentioned at the top of the plots and the blue lines are the fitted linear lines related to the GPS measurements (corresponding R^2 values for each fitted line are presented in Table 3.5).

Table 3.5: InSAR results summary in terms of: Amplitude Dispersion index ($D_A = \sigma/\mu$), Multitemporal coherence (M_c), Total Displacement of PSI and GPS measurements (TD_{PSI} and TD_{GPS}), Std of the PSI measurements and Root Mean Square Error ($RMSE_{TD}$) values between GPS and PSI and MAI measurements. V_R refers to the percentage ratio of GPS and PSI velocities and R^2 indicates R-squared values of the linear curve fitting to the GPS measurements (Figure 3.7).

CR No.	**D_a**	**M_c**	**Azimuth.**	**TD_{PSI} (cm)**	**TD_{GPS} (cm)**	**Std_{PSI} (cm)**	**$RMSE_d$ (cm)**	**V_{PSI} (cm/year)**	**V_{GPS} (cm/year)**	**R^2 (GPS)**
4	**0.12**	**0.61**	**305°**	**12.4**	**12.5**	**3.87**	**1.04**	**9.20**	**9.58**	**0.98**
6	**0.06**	**0.62**	**303°**	**11.8**	**13.3**	**3.75**	**1.62**	**8.83**	**10.77**	**0.97**
8	**0.13**	**0.56**	**283°**	**31.7**	**32**	**2.15**	**0.85**	**23.55**	**23.89**	**0.99**
11	**0.08**	**0.62**	**298°**	**20**	**20.7**	**2.20**	**0.50**	**15.45**	**15.9**	**0.96**
13	**0.19**	**0.57**	**270°**	**37.5**	**39.1**	**4.00**	**4.07**	**27.84**	**29.97**	**0.98**
28	**0.12**	**0.53**	**260°**	**44.8**	**39.1**	**6.00**	**2.68**	**28**	**30.03**	**0.96**
49	**0.21**	**0.51**	**265°**	**21.2**	**20.3**	**6.68**	**1.83**	**16.46**	**15.67**	**0.97**
25	**0.12**	**0.56**	**265°**	**20.3**	**20.1**	**6.23**	**2.47**	**17.74**	**16.21**	**0.96**
23	**0.19**	**0.52**	**260°**	**20.9**	**22.7**	**6.66**	**4.28**	**19.14**	**17.45**	**0.96**
57	**0.11**	**0.58**	**265°**	**19.5**	**18.3**	**5.99**	**3.16**	**14.50**	**14.15**	**0.89**
58 *	**0.14**	**-**	**177°**	**29**	**34**	**4.1**	**3.2**	**19**	**23.1**	**-**

* The displacement of CR58 is derived by MAI. The MAI and GPS measurements for CR58 are in the satellite azimuth geometry.

3.7.2 Offset Tracking Results (area and feature-based matching)

The displacements of the high velocity rate CRs were extracted by the offset tracking estimators. The displacements maps and the corresponding SNR are shown in Figure 3.8. The CRs offsets extracted by each estimator at the center of each CRs footprint (red points). The 2-dimension offset (dx and dy) and SNR values for each CRs are provided in Table 3.6. According to Table 3.6, the best-offset estimations are obtained by the PC (for CR53, 51 and 58) and the OC (for CR54, 56 and 55) with respect to the GPS measurements. As OC results derived from CIAS and ImGRAFT are similar, only OC result obtained by ImGRAFT are presented.

The accuracy assessment of the offset tracking results is given in Table 3.7. The error of the extracted offsets in x (i.e., $\%P_x = (dx_{GPS} - dx_{estimator})/2 \times 100$) and y (i.e., $\%P_y = (dy_{GPS} - dy_{estimator})/2 \times 100$) directions are given in terms of the percentage of the pixel size of the image (i.e., 2 m). For instance, $\%P_x$ of %0, %50 and %100 indicate a correct estimation, one and a half pixel and one-pixel size. The summation of x-y accuracy (i.e., $SP_{xy} = \%P_x + \%P_y$) is an index that shows the performance of each estimator with respect to its counterparts. A lower index (i.e., lower error) means that a higher accuracy has been achieved by the related estimator in *x* and *y* directions.

The accuracy obtained by the area-based matching (see Table 3.7) shows that all estimators can extract a sub-pixel accuracy in the estimation of displacement in the *x* and *y* directions in most cases. Based on SP_{xy} index, OC and PC presented the absolute highest accuracy among other estimators (i.e., OC for CR54, CR56, CR55, and PC for CR53 and CR51). Although the PC showed the highest accuracy for CR53 and CR51, MPC has generally better performance than PC for all CRs. Using a higher robustness iteration parameter (i.e., 4) and applying the resampling process, simultaneously, we observed a small increase of accuracy in the MPC results. Both the NCC-based estimators (i.e., SC by COSI-Corr and NCC by

CIAS) yielded similar results with a relative superiority of SC. Since both use the NCC function to estimate the offset, these results suggest differences in their algorithm implementation. For the CR51, NCC was not able to estimate the displacement.

Table 3.6: Comparison of dx and dy offsets (in meter) with the related SNR for four area-based offset tracking and OC algorithms.

CR No.	GPS		SC			NCC			MPC			OC			PC		
	dx	dy	dx	dy	SNR	dx	dy	SNR	dx	dy	SNR	dx	dy	SNR	dx	dy	SNR
53	1.6	0.3	0.3	0.2	0.89	0.2	0.3	0.96	0.5	0.06	0.99	0.5	1.2	0.79	2.06	0.16	0.47
54	3.2	1.1	2.4	1.3	0.87	1.2	2.7	0.92	2.4	0.6	0.99	2.2	1.2	0.77	3.02	2.8	0.41
56	0.7	3.4	2.2	3.7	0.92	2.2	3.7	0.98	2.1	3.7	0.98	2.2	3.7	0.96	1.9	4	0.7
51	6.1	39.4	7	39.3	0.78	-	-	-	6.8	39.5	0.78	7	39.2	7.9	6.12	39.9	0.5
55	40	14	40.7	14.8	0.8	40.7	14.7	0.85	40.7	14.4	0.97	40.2	14.2	0.81	39.7	15.8	0.41
58	0.016	0.35	0.45	0.12	0.9	0.5	0.25	0.98	0.43	0.06	0.99	0.25	0	0.9	0.09	0.19	0.8

Table 3.7: Accuracy of the extracted offsets (i.e., $\%P_x$ and $\%P_y$) in terms of the pixel size percentage. SP_{xy} is an indicator showing the total accuracy for each CR.

CR No.	SC			NCC			MPC			OC			PC		
	$\%P_x$	$\%P_y$	SP_{xy}	$\%P_x$	$\%P_y$	SP_{xy}	$\%P_x$	$\%P_y$	SP_{xy}	$\%P_x$	$\%P_x$	SP_{xy}	$\%P_x$	$\%P_x$	SP_{xy}
53	50	5	55	70	0	70	55	12	67	55	45	100	23	7	30
54	40	95	135	95	80	175	40	25	65	50	5	55	10	85	95
56	75	15	90	75	15	90	70	15	85	65	12	77	60	30	90
51	45	5	50	-	-	-	35	5	40	45	10	55	1	31	32
55	35	40	75	35	35	70	35	20	55	10	10	20	14	90	104

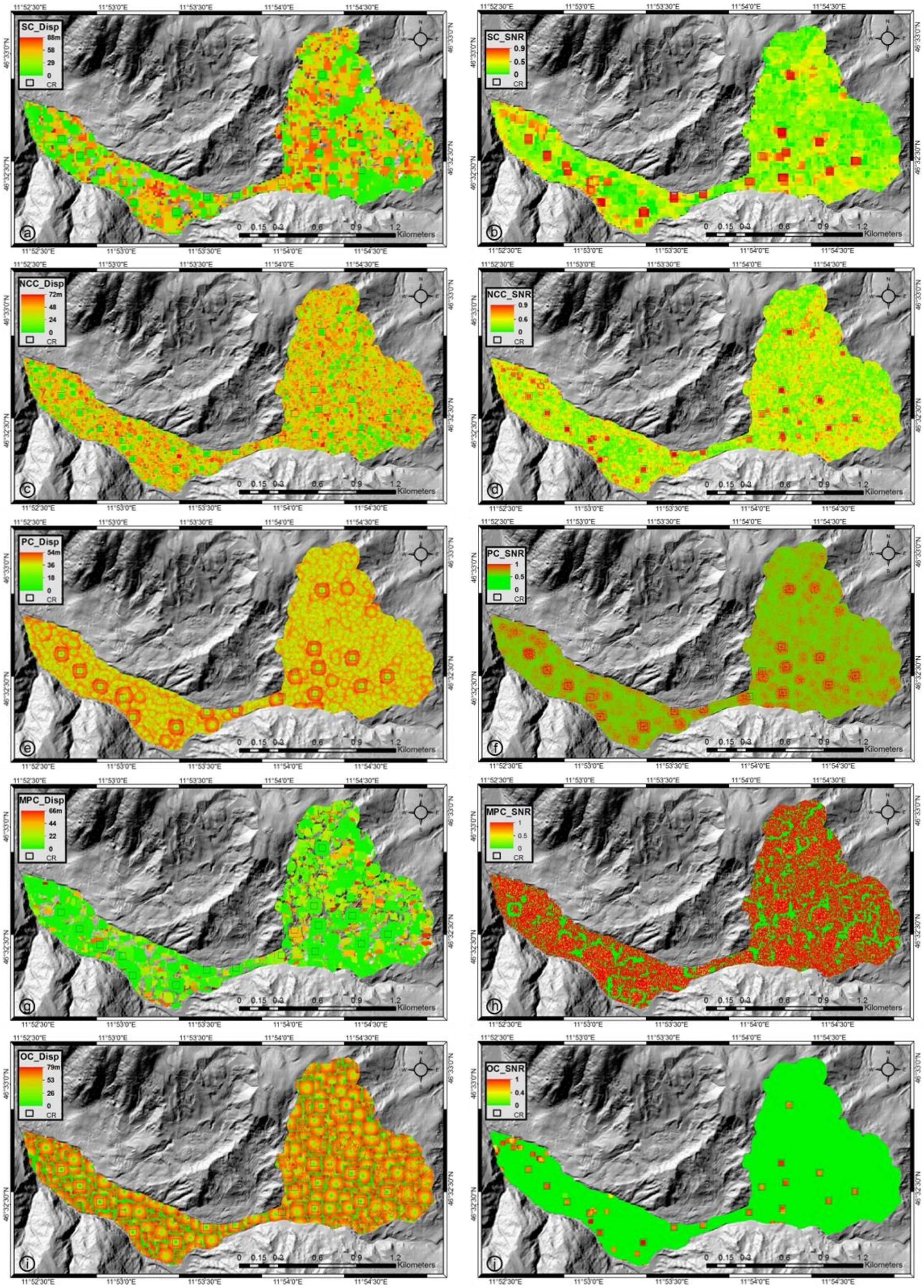

Figure 3.8 : Displacement maps of the CRs. The offsets derived by the offset tracking estimators are superimposed on the hill-shaded DEM of the Corvara. (a) SC displacements; (b) correlation coefficients (SNR) of SC measurements; (c) NCC displacements; (d) correlation coefficients (SNR) of NCC measurements; (e) PC displacements; (f) SNR of PC measurements; (g) MPC displacements; (h) SNR of MPC measurements: (i) OC displacements; and (j) SNR of OC measurements.

Feature-Based Matching Results

The results of the CRs offsets derived by the feature-based matching algorithms with respect to the GPS measurements are presented in Table 3.9. The best-offset estimations are obtained by: the BRISK for CR53, the HARRIS for CR54, the BRISK_S for CR54, the MEIGEN and MEIGEN_S for CR58, and, the HARRIS and MEIGEN (with SURF descriptor as well) for CR51 and 55 (see Table 3.9).

The corner-based detectors were completely able to find all CRs on the images (except using FAST for CR53, 51 and 58). After running the corner and blob-based algorithms on the SAR data, all corner-based detectors (except FAST for CR53, 51 and 58) could detect all the CRs positions properly (e.g., BRISK in Figure 3.9a), whereas the blob-based detector (i.e., SURF) was not able to detect none of the CRs positions (Figure 3.9b).

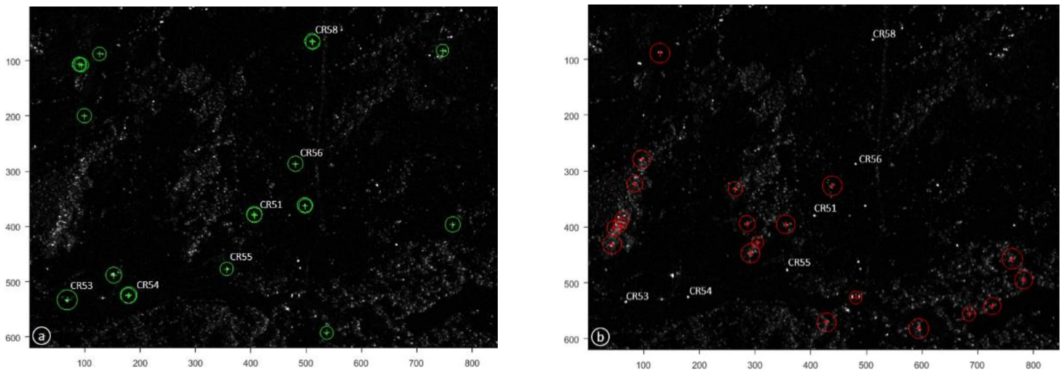

Figure 3.9: CRs detection. The high velocity rate CRs detected by (a) BRISK function as corner-based feature detector and (b) SURF function as blob-based feature detector. The detected features of both algorithms were superimposed on the SAR data in 5 April 2014 (only for the high velocity rate CRs region).

After finding the desired features (CRs), they have matched by the relevent descripors. For example, the CRs extrected by BRISK detector in Figure 3.9a have been matched using the FREAK descriptor to the pair of SAR data (see Figure 3.10). Random sample consensus (RANSAC) [107] was used to only keep the inlier matched connections and remove the outliers when the features matched wrongly.

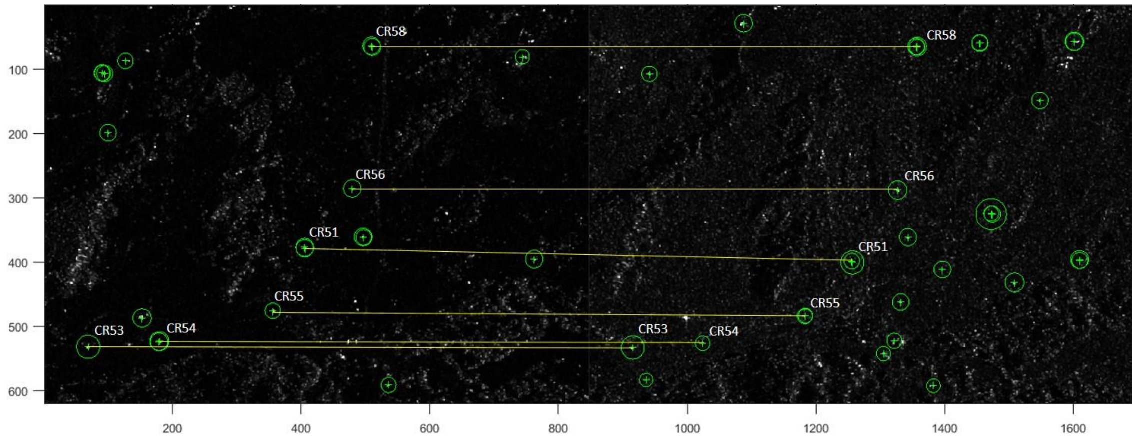

Figure 3.10 : Final feature-based matching results. The feature matching was performed by FREAK descriptor and all matched connections apart from the high velocity rate CRs were removed from the image.

The offset accuracies of the feature-based algorithms are shown in Table 3.9. Based on SP_{xy} index, BRISK, HARRIS, MEIGEN and their combination with SURF presented the absolute highest accuracy. HARRIS, BRISK and MEIGEN generally presented more accurate results, respectively, and the FAST showed the worst accuracy.

Table 3.8: The dx and dy offsets (in meter) for four corner-based feature matching algorithms and the combination of BRISK with FREAK, and HARRIS, MEIGEN and FAST with SURF.

CR No.	GPS		BRISK		HARRIS		MEIGEN		FAST		BRISK_S		HARRIS_S		MEIGEN_S	
	dx	dy	dx	dy	dx	dy	dx	dy	dx	dy	dx	dy	dx	dy	dx	dy
53	1.6	0.3	1.3	0.4	0.9	0	1.14	0.2	-	-	3.06	0.4	0.9	0	1.14	0.2
54	3.2	1.1	2.4	2.8	2.6	1.4	2.4	1.4	6	6	4.8	1.6	2.6	1.4	2.4	1.4
56	0.7	3.4	2.0	3.6	2.4	3.8	2.2	3.6	0	4	0.8	3.6	2.4	3.8	2.2	3.6
51	6.1	39.4	7.4	38.0	7	39.4	7	39.4	-	-	9	37	7	39.4	7	39.4
55	40	14	37.4	14.6	41	14.8	41	14.8	36	14	37.4	14.6	41	14.8	41	14.8
58	0.016	0.35	0.4	0.9	0.8	0	0.8	0.04	-	-	0.4	0.86	0.8	0	0.8	0.04

Table 3.9: Extracted offsets accuracy (i.e., $\%P_x$ and $\%P_y$) in terms of pixel size percentage. SP_{xy} is an indicator showing the total accuracy for each CR.

CR No.	BRISK			HARRIS			MEIGEN			FAST			BRISK_S			HARRIS_S			MEIGEN_S		
	$\%P_x$	$\%P_y$	SP_{xy}	$\%P_x$	$\%P_y$	SP_{xy}	$\%P_x$	$\%P_y$	SP_{xy}	$\%P_x$	$\%P_x$	SP_{xy}	$\%P_x$	$\%P_x$	SP_{xy}	$\%P_x$	$\%P_x$	SP_{xy}	$\%P_x$	$\%P_x$	SP_{xy}
53	15	4	19	35	16	51	23	6	29	-	-	-	73	4	77	35	16	51	23	6	29
54	40	82	122	30	12	42	40	12	52	140	242	382	80	22	102	30	12	42	40	12	52
56	65	6	71	85	16	101	75	6	81	35	26	61	5	6	11	85	16	101	75	6	81
51	65	70	135	44	0	44	44	0	44	-	-	-	145	120	265	44	0	44	45	0	44
55	130	30	160	50	40	90	50	40	90	200	0	200	130	30	160	50	40	90	50	40	90

3.8 Discussion

3.8.1 InSAR (Non-Linearity Effect in PSI)

According to the CR quality assessment results, we observed that the footprints of the CR13 (Figure 2.2b) and CR58 (Figure 2.4c) do not correspond to a cross-like shape, meaning that their IRFs are not the ideal ones (as presented in Figure 2.2d). A comparison of the RPSLR, APSLR and ISLR parameters between the first and last acquisitions (Table 2.2) clearly shows variations of the values. These changes indicate that CRs did not keep the optimal orientation during the data acquisition time span. This problem has probably occurred due to the landslide movement tilting the CRs. The tilts led to un-correlated signal in the clutter region (i.e., the grass surrounding the CRs) and induced a phase error. The probability density function (*pdf*) (3.15) of phase error (φ_e) (3.16) for a Point Scatterer (PS) shows that the amplitude of the phase error depends on the Signal to Clutter Ratio (*SCR*) (3.17) [108]:

$$pdf\left(\varphi\right)=\frac{\sqrt{SCR}.\left|\mathrm{Cos}\left(\varphi\right)\right|}{\sqrt{\pi}}.e^{SCR.\mathrm{Sin}^{2}\left(\varphi\right)} \tag{3.15}$$

$$\varphi_e=\frac{1}{\sqrt{2.SCR}} \tag{3.16}$$

$$SCR=\frac{\sigma_T}{\langle\sigma_C\rangle}=\frac{\sigma_T}{\langle\sigma^{\circ}\rangle A} \tag{3.17}$$

where σ_T, σ_C, σ° and A indicate *SCR* of PS, average of *SCR* clutter, sigma naught and surface around the PS, respectively [109]. Equations (3.15) and (3.16) imply that by increasing the *SCR* the width of the pdf of the phase error narrows and the phase error decreases. Some considerations are also inferred by investigating the PSI results accuracy assessment of each CR (Table 3.5). D_A of all CRs have values smaller than 0.25 leading to a high coherence of the SAR signals that indicates that CR backscattering values allow them to be considered as PS despite the accrued tilting. $\mathrm{M_c}$ values vary between 0.51 (the lowest for CR57) and 0.62 (the highest for the CR6 and CR11), which implies a deviation of CRs motion type from the linear behavior. The GPS measurements showed a not-steady status and some irregular patterns (i.e., sudden vertical changes for some given time) in the CRs movements. The vertical changes of CR6 and CR28 (measured by GPS) are here represented as examples of non-linear and linear CRs behaviors (see Figure 3.11). The effect of this non-linearity can be observed in PSI results. If we compare the cumulative displacements of CR28 with CR6 (Figure 3.7), CR28 shows clearly a better agreement than CR6 with the GPS line.

Figure 3.11 : Linear and non-linearity behaviors of CRs. Elevation changes of CR28 and CR6 are derived by the GPS measurements.

These sudden and irregular changes are mainly related to the landslide movement itself probably trigged by specific meteorological conditions. Since the conventional PSI technique is based on a predefined linear model, the effect of non-linearity appears as a bias in the precision assessment step (e.g., high RMSE value). Different quadratic, cubic and stepwise models can be used as pre-defined models to mitigate the effect of non-linearity. However, adapting a function that perfectly represents the motion type of natural phenomena (e.g., landslide) is not straightforward, due to their unpredictability and complexity. Therefore, non-predefined model-based techniques, which relies on spatial-correlation filtering, turn out more appropriate for monitoring complex natural terrain [106].

While deformation information derived by the PSI technique is limited to LOS direction, an increase of the uncertainty is expected for non-LOS displacements. However, a meaningful trend is generally observed by assessing the Std of PSI results and azimuth displacements of each CR (Table 3.5). The Std and RMSE decrease at the CRs with the displacement azimuth close to LOS in comparison to other CRs. Since the azimuth displacement of CR8 (i.e., 283°) is very close to the azimuth of LOS (i.e., 280°), we assume that the Std of its measurement equals LOS precision (corresponding to 3.17 cm displacement). Therefore, the precision of the vertical and horizontal displacements was calculated using (2.9) based on this assumption (Figure 3.12). The Std values increase (i.e., decrease in precision) by getting away from the LOS direction shown on the circle in Figure 3.12c.

Another key factor that could potentially lead to a bias in the GPS measurements, which in turn increases Std values in Table 3.5 is CR tilting. Since the phase center variation (PCV) of GPS antenna is computed in the horizontal position, any slight changes (e.g., tilting) in the antenna statues causes the PCV estimation are not valid anymore and the measurements are biased corresponding to the degree of the antenna tilting.

With respect to the InSAR-PSI results, a lower LOS Std for C-band CR displacement (i.e., 5 mm) has been reported with a related sensitivity analysis for urban areas [110] [111]. Several main reasons can justify the higher Std values of our results including lack of an optimal orientation of the CRs and the errors propagated in the measurement caused by the non-linearity behavior of CR motion type installed in the natural terrain. In summary, many error sources can contribute to PSI measurements leading to the increase of Std and RMSE. They can be categorized into three main categories: (i) CR-related error sources such as manufacturing, optimal size, and CR orientation; (ii) GPS measurement error (in the PCV computation due to the CRs tilting); (iii) performance of the used InSAR algorithm for the intended application (i.e., predefined model-based or non-model-based); and (iv) other external noise (e.g., atmosphere).

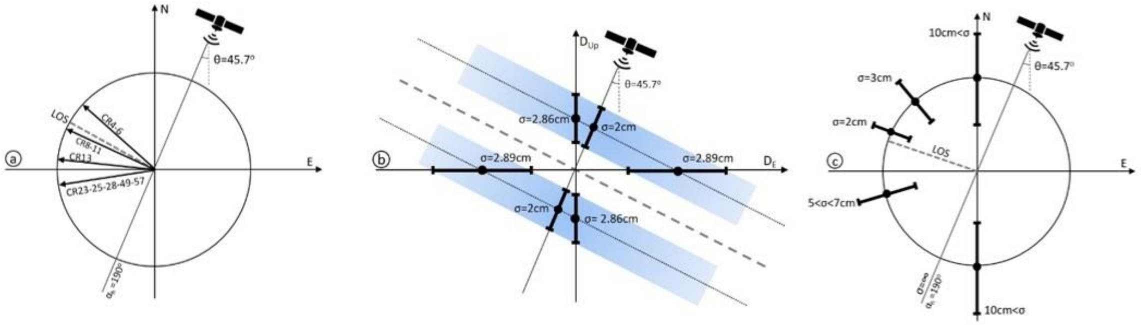

Figure 3.12: Sensitivity analysis of the CRs displacements. (a) Azimuth angles of CRs displacements (the low velocity rate category) with the vectors of the LOS and heading of the satellite; (b) Precision of CRs displacements in LOS direction for the vertical and horizontal displacements in the Zero-Doppler plane and (c) Precision of the CRs displacement measurements in the East and North plane.

3.8.2 InSAR (MAI Challenges and Limitations)

The precision of the MAI phase is a function of *n* (normalized squint) in (3.8) and MAI phase is determined by the following equation [112]:

$$\sigma_{MAI} \approx \frac{1}{\sqrt{2N_{L.MAI}}} \frac{\sqrt{1-\gamma^2}}{\gamma} \tag{3.18}$$

$$\gamma = \frac{\gamma_{f} + \gamma_{b}}{2} \tag{3.19}$$

$$N_{L.MAI} = N_a . N_r . (B_s . PRF) . (B_c . f_s) W_s \tag{3.20}$$

where N_l and γ refer to the effective number of looks and total correlation (forward γ_f and backward γ_b), respectively. The $N_{L.MAI}$ is determined by the system parameters: the multi-looking factor in azimuth (N_a) and range (N_r), the chirp bandwidth (B_c), the sub-aperture Doppler bandwidth (B_s), the sampling frequency (f_s), the pulse repetition frequency (PRF) and the noise reduction factor by an adaptive filtering (W_s) [112].

According to (3.8) and (3.18), the MAI phase precision can be improved by increasing *n* and $N_{L.MAI}$. When we increased N_a and N_r (i.e., 4 × 4, 8 × 8 and 16 × 16) the coherence considerably deceased. As CRs represent clusters of coherent pixels, surrounded by low coherence ones (i.e., vegetation), increasing the multi-looking factor spatially averages the coherence values decreasing the coherence. Therefore, this limitation does not make it possible to increase the MAI phase precision by increasing the multi-looking factor. Regarding increasing the "*n*" parameter, an increase of "*n*" did not improve the MAI results in terms of displacement precision. Since the satellite observes the CR as a point-like target, at least within a quite wide range of angles, it does not matter how much the separation width of the aperture is, in any case the CR will be viewed by satellite as a point target depart from any change in the squint angle. In the high velocity rate CRs category, only the CR58 displacement (about 34 cm) was in the range of MAI maximum detectable displacement and other CRs experienced a displacement of more than one meter in the time span. As the CR58 displacement azimuth (i.e., 177°) was nearly along the satellite azimuth (i.e., 190°), the displacement accuracy derived by the MAI technique provided higher accuracy (i.e., 2.5%-pixel size) than with offset tracking techniques (see Table 9).

Although MAI measurement precision up to approximately 1% of the azimuth resolution has been reported [112] in a high coherent region and applying a high multi-looking factor, the restriction of multi-looking factor (leading to a decrease in coherency) does not improve the precision for the CR displacement. Despite this limitation, the estimated displacement using the MAI technique outperformed the offset-based techniques in the azimuth direction.

3.8.3 Offset tracking (potentials of the area-based matching algorithms)

To evaluate the performance of each estimators in details, the evolution of the footprint of each CR and its pixel values must be investigated. For instance, the footprint of CR53 and CR55 (with related pixel values) show the slight and drastic pixel values changes between the first and last data acquisition, respectively (Figure 3.13). According to the PSLR and ISLR parameters of the CRs (Table 2.2), the tilts on the CRs triggered by the landslide movement caused some changes in those parameters. The CRs tilting have modified data pixel values leading difficulties for similarity-based or variant-sensitive estimators to find the exact position of the signal peak for an accurate offset estimation (see Figure 3.13).

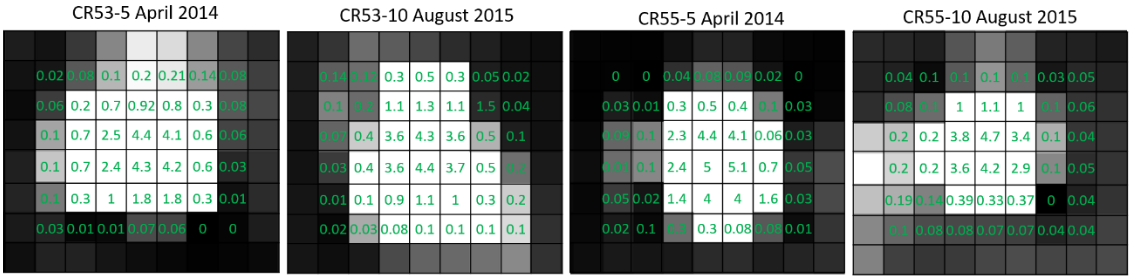

CR53-5 April 2014

0.02	0.08	0.1	0.2	0.21	0.14	0.08
0.06	0.2	0.7	0.92	0.8	0.3	0.08
0.1	0.7	2.5	4.4	4.1	0.6	0.06
0.1	0.7	2.4	4.3	4.2	0.6	0.03
0.1	0.3	1	1.8	1.8	0.3	0.01
0.03	0.01	0.01	0.07	0.06	0	0

CR53-10 August 2015

0.14	0.12	0.3	0.5	0.3	0.05	0.02
0.1	0.2	1.1	1.3	1.1	1.5	0.04
0.07	0.4	3.6	4.3	3.6	0.5	0.1
0.03	0.4	3.6	4.4	3.7	0.5	0.2
0.01	0.1	0.9	1.1	1	0.3	0.2
0.02	0.03	0.08	0.1	0.1	0.1	0.1

CR55-5 April 2014

0	0	0.04	0.08	0.09	0.02	0
0.03	0.01	0.3	0.5	0.4	0.1	0.03
0.09	0.1	2.3	4.4	4.1	0.06	0.03
0.01	0.1	2.4	5	5.1	0.7	0.05
0.05	0.02	1.4	4	4	1.6	0.03
0.02	0.1	0.3	0.3	0.08	0.08	0.01

CR55-10 August 2015

0.04	0.1	0.1	0.1	0.1	0.03	0.05
0.08	0.1	1	1.1	1	0.1	0.06
0.2	0.2	3.8	4.7	3.4	0.1	0.04
0.2	0.2	3.6	4.2	2.9	0.1	0.05
0.19	0.14	0.39	0.33	0.37	0	0.04
0.1	0.08	0.08	0.07	0.07	0.04	0.04

Figure 3.13: Changes of the footprints shape and pixel values of CRs. The footprints of the CR53 and CR55 with the corresponding pixel values on the CSK data for the first and last data acquisitions are given.

The function behavior of each estimator of the CR footprint could be an appropriate indicator to understand why some estimators provide more precise results than others for a given CR. Figure 3.14 reports three functions of the used estimators from three template matching categories (i.e., phase-based (PC), feature-based (OC) and cross correlation-based (NCC)) depicted. The NCC response to the CRs corresponding to stable pixels values (i.e., CR53 and CR54) between two data acquisitions is nearly flat, whereas those with highly changing pixel values due to tilting (i.e., CR51 and CR55) have uneven or semi-flat surface. PC response provides a single sharp peak for the nearly fixed CRs (i.e., CR53 and CR54) and multiple sharp peaks for the tilted CRs (i.e., CR51 and CR55). OC, as a feature-based method, seeks for a distinctive feature (the CRs footprint) using a pre-defined descriptor (i.e., OIOG). The results show that PC and OC outperform NCC and OC is relatively superior to PC.

Despite reliability and simplicity of CC-based methods, such as Normalized CC (NCC), several downsides have been reported [64,65] . In this study, we noticed that the NCC accuracy of offset estimation is sensitive to noise and limited to the data pixel size. In addition, changing scale, rotation or shearing of image features lead to decrease the correlation coefficient. Some drawbacks of CC-based matching related to the geometrical changes could also be mitigated using the generalized versions of CC-based methods [66,67,68].

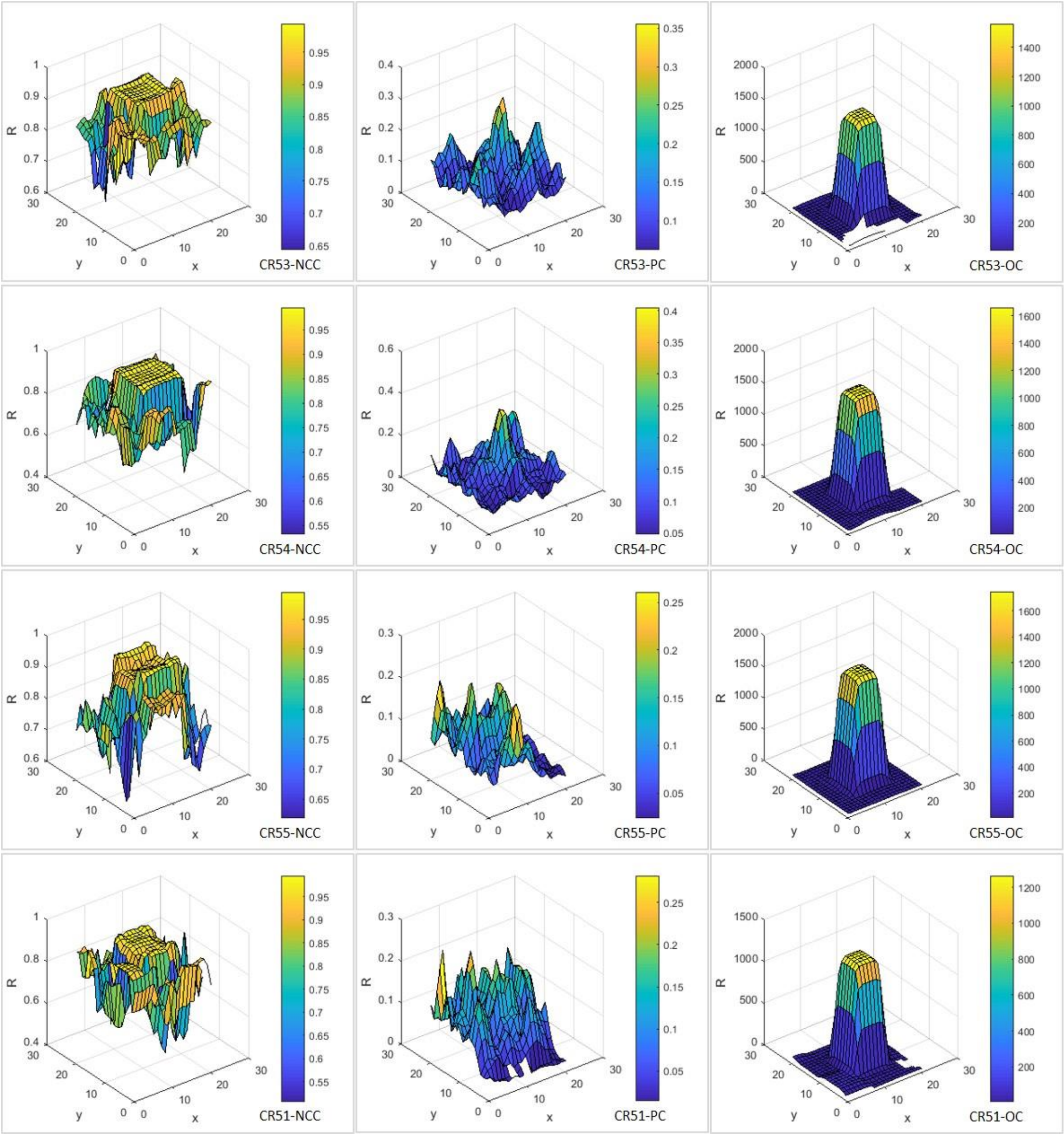

Figure 3.14: Estimator function trends. Behavior of the estimator functions (i.e., NCC, PC and OC) at the CR51, 53, 54 and 55 positions. Since the range of R or SNR values of OC were small, for better visualization the values have been multiplied by 1000.

3.8.4 Offset tracking (potential of the feature-based matching algorithms)

For CR53, CR54 and CR56 that are slightly tilted (small changes in pixel values and shape) comparing to CR51 and CR55 (drastic changes in pixel values and shape) by the landslide movement, feature-based matching results outperformed the area-based ones. This means that the feature-based matching algorithms (as invariant detectors/descriptors to feature deformation) managed to cope with some degrees of the distortion caused by CR tilting. While in the case of drastic changes in pixel values (e.g., CR51 and CR55), they were not able to remain invariant to the pixel value variations.

The comparison of the area and feature-based results in Table 3.11 show that the PC from the area-based and OC from feature-based categories provided better results than feature-based algorithms (see SP_{xy} indexes). HARRIS and MEIGEN detectors generally provided more accurate results than BRISK and FAST, whereas FAST had the worst performance among the all corner-based detectors. In cases of CR54, CR51 and CR55, the HARRIS and EIGEN results were identical when combined with the SURF descriptor. This means that in case of high pixel value changes, the detector and descriptor combination does not effect on the results.

To evaluate the performance of the feature-based matching algorithms, some evaluation metrics have been proposed. Ref. [118] defined the 1-accuracy and recall values of each image to assess the matching performance. The 1-accuracy and recall refer to the number of false matches relative to the total number of matches and the number of correctly matched regions with respect to the number of corresponding regions between two images of the same scene, respectively. According to [119], five different metrics are proposed to evaluate the detector and descriptor performance: putative match ratio, accuracy, matching score, recall and entropy. Since we used only one pair of the SAR images and the intended features on the images were only 16 CRs, we compared the achieved offsets with GPS measurements as Ground Control Point (GCP) to validate the performance of each algorithm. More information concerning a quantitative and qualitative comparison of the area and feature-based matching can be found in [120], while feature-based matching algorithms and performance comparison are described in [72,73,69]. A summary of the advantages and disadvantages of both area and feature-based matching are presented in Table 3.12 and Table 3.13.

Finally, the velocity map of the CRs using integration of PSI, MAI, and offset tracking displacements (using the most accurate results derived by the related algorithms) is presented in Figure 14. The minimum 8.8 cm/year and maximum 31.6 m/year velocity rates were derived for CR6 and CR55, respectively, by the PSI and OC techniques. Based on the velocity map provided in Figure 3.15, three different geomorphological zones can be distinguished: (i) Accumulation zone including CRs4, 6, 8, 11; (ii) track zone including CRs13 and 53; and (iii) source zone including CRs23, 25, 28, 49, 57 and 58 [92].

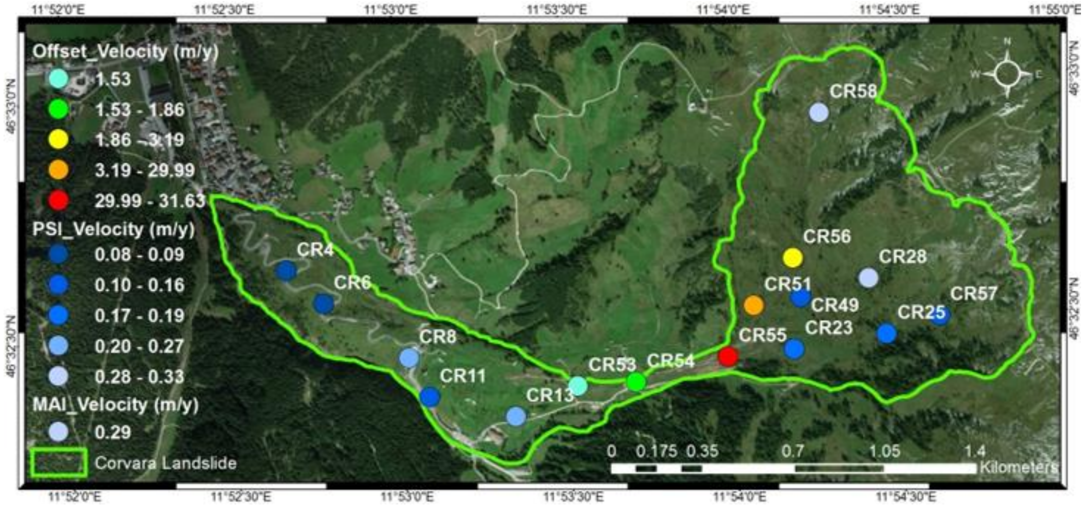

Figure 3.15: Velocity of the CRs derived by PSI, MAI, and Offset tracking-based algorithms. The movement rate of the low velocity CRs derived by PSI, the high velocity CRs by the Offset tracking algorithms (i.e., boded value in Table 10) and CR58 by MAI.

Table 3.10: The offsets and error %P (i.e., P = ($D_{gps} - D_{est}$)/2 × 100) for CR58 (unit in meter). All the offsets obtained by the estimators and GPS measurements were projected to the satellite azimuth direction using **Error! Reference source not found.**.

		InSAR	Area-Based Matching					Feature-Based Matching							
CR No.	GPS	MAI	SC	NCC	MPC	OC	PC	BRISK	HARRIS	MEIGEN	FAST	BRISK_S	HARRIS_S	MEIGEN_S
58	0.34	0.29	0.19	0.2	0.13	0.043	0.2	0.95	0.13	0.17	-	0.91	0.13	0.17
%P		2.5	7.5	7	10.5	14.8	7	30.5	10.5	8.5	-	28.5	10.5	8.5

Table 3.11: SP_{xy} index comparison between area and feature-based matching algorithms. Bolds values indicate higher accuracy achieved by a particular estimator for one specific CR.

CR No.	SP_{xy} Index											
	Area-Based Matching					Feature-Based Matching						
	SC	NCC	MPC	OC	PC	BRISK	HARRIS	MEIGEN	FAST	BRISK_S	HARRIS_S	MEIGEN_S
53	55	70	55	100	30	19	51	29	-	77	51	29
54	135	175	65	55	95	122	42	52	382	102	42	52
56	90	90	85	77	90	71	101	81	61	11	101	81
51	50	-	40	55	32	135	44	44	-	265	44	44
55	75	70	55	20	104	160	90	90	200	160	90	90

Table 3.12: Advantages and disadvantages of the area and feature-based matching techniques.

Matching Methods	**Patch or Area-Based**			**Featured-Based**
Image domain	spatial domain		frequency domain	
Techniques	CC	NCC	PC	OC
Accuracy	Up to sub-pixel (by interpolation)	Up to sub-pixel (by interpolation)	Up to sub-pixel (by over sampling)	Up to sub-pixel
Function	Similarity	Similarity	Similarity—FFT	Orientation of intensity and FFT
Advantages	Simple and easy computation	- Invariant to linear brightness and contrast variations - Not too sensitive to translation and small rotation and scale changes	- Less sensitive to frequency dependent noise and varying illumination - Invariant to linear changes in brightness - Invariant to rotation	- Statistically robust - Illumination and scale invariant - Fast
Shortcoming	- Biased by changes in global brightness - Sensitive to intensity changes (varying Illumination)	- Sensitive to rotation, scale changes, different illumination, viewing angle and temporal changes - Flatness of peak	- Sensitive to spatial dependent noise and illumination - conditions	- More sensitive to local structural than intensity information

Table 3.13: Advantages and disadvantages of the feature-based matching algorithms regarding offset estimation.

Matching Method	**Featured-Based**				
Feature style	Corner-based				Blob-based
Detector	BRISK	HARRIS	MEIGEN	FAST	SURF
Feature type	- Point tracking - Corners - multi-scale detection	- Point tracking - Corners - Single-scale detection	- Point tracking - Corners - Single-scale detection	- Point tracking - Corners - Single-scale detection	- Blob - Multiscale detection
Scale-Rotation	Invariant-Invariant	Variant-Invariant	Variant (scale)	Variant-Invariant	Invariant-Invariant
Descriptor	- Binary-based - Fast but Less accurate (localization)	-	-	-	- Distribution-based - Slower - More accurate (localization)

3.9 Conclusions

Although the Corvara landslide has been the subject of the previous studies [36,39], they have faced with the intrinsic limitations of the techniques used. For example, PSI was not able to estimate the high velocity rate and non-LOS CRs and the differential DEM (UAV-based photogrammetry) derived from two subsequent acquisitions was only able to detect the vertical deformation limited only to the small part of the landslide (i.e., left-down side of CR58) due to the large extend of the landslide. In this research, these limitations have been overcome by using the integration of PSI, MAI, and offset tracking results, allowing the estimation of the displacements of the CRs over the whole part of the landslide.

The PSI results showed that the proper orientation and quality assessment parameters of CRs (i.e., PSLR; ISLR and IRF) have a key role in the noise error reduction. The provided sensitivity analysis model indicated that the uncertainty of the PSI measurements increases by deviating from the displacements azimuth with respect to the LOS azimuth. When displacement is aligned to the satellite azimuth, the displacement estimation is impossible (infinitive Std). Moreover, non-linearity behavior of the CRs motion in natural terrain could propagate some errors in the final extracted displacements when a pre-defined-based model of the PSI technique is used. In such case, non-predefined model methods should be considered.

The MAI result obtained for CR58 demonstrated that MAI provided the best-offset estimation among other offset-based estimators. This means that if displacement is aligned to N–S direction (nearly satellite path), MAI provides the highest accuracy up to 2.5% of the pixel size of CSK data (i.e., 2 m). This result could even be improved in case of having data with a higher coherence. Low coherence or a high coherent target surrounded by low coherent surface (in our case CR surrounded by vegetation) are the limiting factors to use higher multi-looking factors to increase MAI precision.

The accuracy of the amplitude offset tracking technique have been empirically estimated between about 1/10 to 1/30 of the pixel size for typical SAR systems. This accuracy corresponds to 20 cm and 6.6 cm of the pixel size of CSK data (i.e., 2 m) or 10% and 3.3% of the pixel size. The offset accuracy varied in *xy* directions, achieving from 0% of the pixel size (i.e., correct estimation) using a combination of the feature-based algorithms (e.g., MEIGEN_S for y offset of CR51) up to 1% of the pixel size using the phase correlation (e.g., PC for x offset of CR51). According to the results, not only the main objective of the paper was fulfilled (i.e., sub-pixel accuracy of offset estimation) but also a higher accuracy was obtained. The results were obtained when the random changes in pixel values occurred by CR tilting between two data acquisitions (i.e., at the worst-case scenario). Meanwhile, area and feature-based algorithms have been mainly developed to take into account the common geometric distortions (e.g., scale, rotation, and translation). Therefore, in normal conditions (with common distortions), the proposed approaches should provide more accurate and reliable results.

Chapter 4

4. LANDSLIDE MONITORING USING SENTINEL-1 AND GROUND-BASED SENSORS

This chapter [1] *focuses both on evaluating the performance of DInSAR using the SBAS algorithm by changing unwrapping and coherence parameters with Sentinel-1 imagery, and on applying DInSAR together with DGNSS measurements to monitor an active and complex landslide. To this end, 41 Sentinel-1A/B images covering the period from January 2015 to October 2016 were processed by using the SBAS algorithm. Changing in the selection of the coherence thresholds, 2D and 3D unwrapping processes give various results (compared with GPS data) in terms of reliability and accuracy, supporting the understanding of the landslide velocity field. Evolutions of phase changes are analyzed according to the coherence and the monitored ground-based displacements.*

4.1 Introduction

DInSAR has the capability to precisely monitor surface displacements over time (temporal sampling rate up to 6 days for Sentinel-1A/B) with a wide coverage in a labour-saving, time- and cost-efficient manner [14]. Two main categories of advanced DInSAR processing techniques for displacement time-series generation exist: persistent scatterer interferometry (PSI) and small baseline subsets (SBAS) techniques [123][22][124]. Both approaches can be also merged together [24]. Whilst these methods have shown great potential for landslide monitoring and detection [125], some limitations remain, especially in the detection and estimation of significant changes in vegetated terrains [126]. According to [127], a common challenge to be faced in both PSI and SBAS algorithms is the phase unwrapping (PhU) operation that represents the retrieval process of the absolute phase signals from their (measured) modulo-2π restricted components,

---

[1] Part of this chapter appears in:

[147] M. Darvishi *et al.*, “Sentinel-1 and Ground-Based Sensors for Continuous Monitoring of the Corvara Landslide (South Tyrol, Italy),” *Remote Sens.*, vol. 10, no. 11, p. 1781, 2018.

i.e. interferometric fringes. The unwrapping operator estimates an ambiguity that is an integer number of 2π radians in wrapped data. Several approaches have been used to remove this ambiguity and minimize the total length of discontinuities in the unwrapped phase. Branch cut [128], relying on restriction of integration over image to paths with local phase differences within 2π. Minimum Cost Flow (MCF) is a statistical-based approach to optimize flow in each of the arcs that minimize the total cost [129]. Least square-based methods [130] are based on two-dimensional partial differential equation.

Temporal and spatial decorrelation, as well as atmospheric and ionospheric noises are often present in DInSAR-based results [17], [27]. However, the area-wide coverage of SAR data can compensate the low spatial sampling of ground-based data while high temporal sampling rates of ground-based data overcomes the low temporal sampling rates of SAR data. Accordingly, DGNSS and DInSAR could be utilized as complementary methods to fully quantify surface displacement and not only for validation purposes. DGNSS data for instance can reach a precision in the order of millimeters at high temporal sampling rates (depending on the configuration mode) on one single point. The combination of DGNSS and DInSAR estimated displacements (e.g. PSI and DGNSS), derived by using well-known interpolation techniques such as minimum curvature [131], Kriging [132] or least-squares collocation [133], can provide an area-wide displacement map and a 3D displacement map [134]. DGNSS data could also assist to mitigate the atmospheric artifacts and correct water vapor effects from the SAR data [135], [136].

PSI using COSMO-SkyMed data has only been applied successfully to the Corvara landslide to the X-band corner reflectors (CRs) installed there, while SBAS failed to produce a spatial displacement map due to high sensitivity of X- band data to vegetation [90]. The recent availability of C-band data such as S1 data, also characterized by frequent and constant acquisitions, gives a promising opportunity to highlight the feasibility and accuracy of monitoring a complex and vegetated continuously moving landslide applying the SBAS algorithm to S1 data. At this aim, the ground-based and remote sensing data are presented as well as the methodological workflow in the following sections. Afterwards, DInSAR results are analyzed and compared with DGNSS data in order to discuss potentials and limitations of the new S1-mission for a continuous spatial monitoring of complex and vegetated landslides.

4.2 Materials

4.2.1 Data

The remote sensing data consists of 41 S1 scenes covering the period from January 2015 to October 2016 (Table 4.1). S1 imagery are processed by the SBAS algorithm [22] as described in the next section.

Table 4.1: Sentinel-1 data specification. The following acronyms were used in the table: polarization (Pol), incident (Inc), azimuth (track) (Az), revisit time (Rtime), range (Rg), and wavelength (W.L).

Product Type	**Mode**	**Pass**	**Pol.**	**Inc/Az angle**	**Rtime**	**Rg × Az spacing**	**W.L**
S1-A/B	IW	Descending	VV	42°/−165°	12/6 day	3.8 m × 13.8 m	5.6 cm

We were used the rainfall data from the meteorological station located in the North of the landslide (Figure 4.1A) and DGNSS measurements. A DGNSS reference station (Ciampai), operated by the South Tyrolean Positioning Service (STPOS), and delivers the data to correct the measured raw DGNSS data to an accuracy in the millimetre range. Raw data measured during monthly field campaigns is processed with the Leica© Geo Office software. The processing of permanent DGNSS data has recently been operationalized with the Leica© Spider software. The current DGNSS monitoring network was established in 2013 and consists of three permanent DGNSS stations and 13 periodically measured benchmarks (landslide movement destroyed the stations 51 and 55), which are equipped with a Leica GM10 receiver and an AS10 antenna. The 13 benchmarks are surveyed during field visits with DGNSS devices (Leica© GS10 receiver and AS10 antenna) once a month with a measurement time of at least 90 minutes allowing a precision of 1 mm (1 standard deviation). The DGNSS-monitoring network (Figure 4.1A) collects pointwise information about the landslide displacement and can also be used for validation purposes of the results obtained by DInSAR processing. At each DGNSS-surveyed point, both permanently and monthly, a corner reflector with a support system for the DGNSS antenna is installed (Figure 4.1B). The CRs are of different sizes in order to be captured by SAR-sensors of different wavelengths. X-band CRs were installed in 2013 and ground surface displacement s were measured by multi-temporal imagery coming from the Cosmo Sky-Med satellite [90].

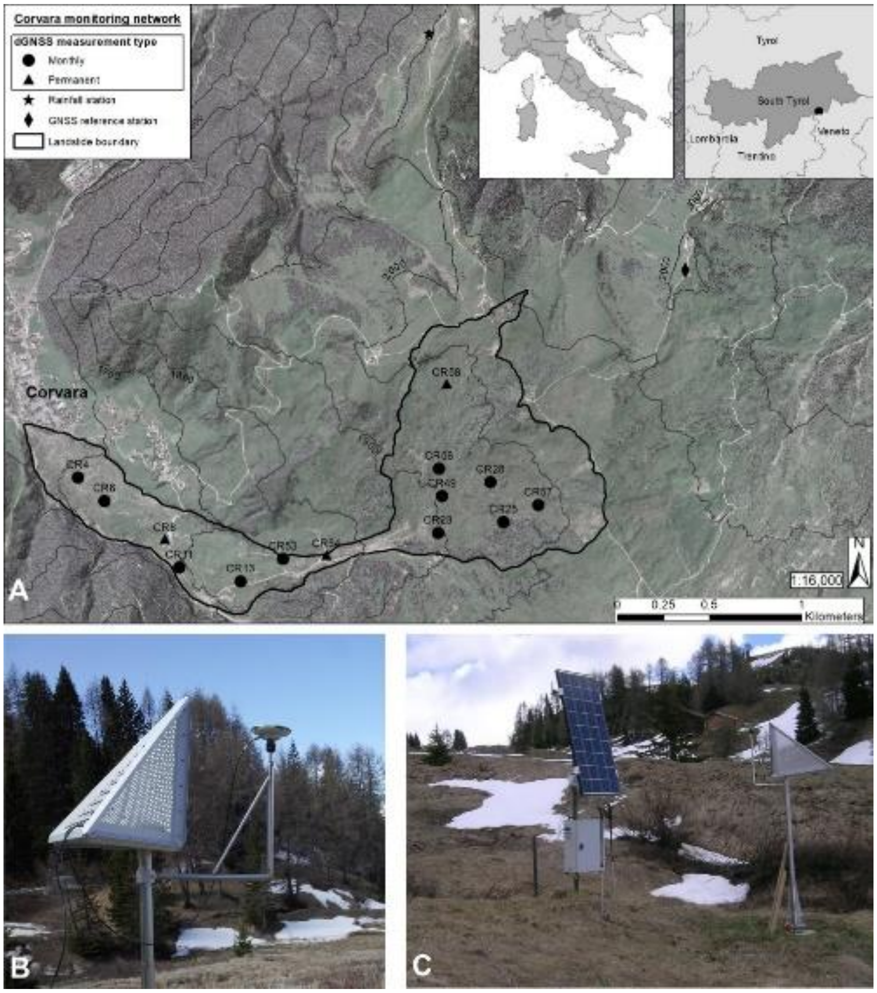

Figure 4.1: Landslide monitoring network location and field impressions: (A) Landslide monitoring network; (B) monthly measurement station consisting of an X-band corner reflector and a support for the DGNSS antenna; (C) permanent DGNSS station, solar panel for power supply, and X-band corner reflector. DGNSS: differential global navigation satellite system.

4.3 Methods

The selected parameters and processing steps carried out with the software SARscape [99] to estimate the quantitative landslide movement are summarized in Figure 4.2. First, the diagram of connections to selected S1 image pairs was created before the generation of the interferograms. It defines the combination of SAR pairs to be processed choosing the appropriate master and slave images, after calculating their normal and temporal baselines.

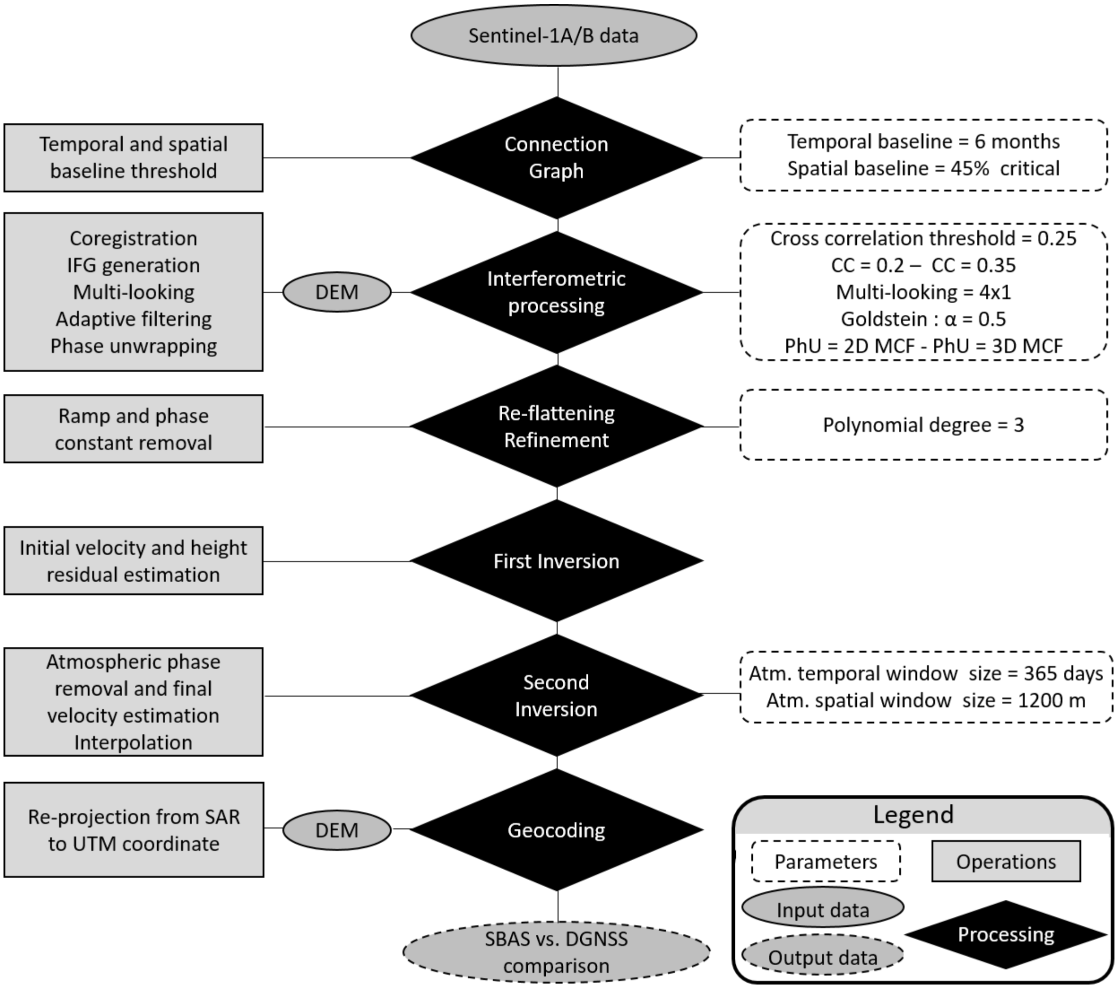

Figure 4.2: Workflow of the Small BAseline Subsets (SBAS) processing for the slope displacement analysis. Atm. and IFG refer to atmospheric and interferograms, respectively. UTM: Universal Transverse Mercator

In the interferometric processing section, coregistration, interferogram generation, multi-looking, filtering, and phase unwrapping were performed successively. The slave images were coregistered with the master using a 2.5-m resolution digital elevation model (DEM) provided by the Autonomous Province of Bolzano. In the coregistration step, (1) a local nonparametric shift estimate is calculated by using DEM and orbital information, (2) a set of windows (64 × 64 in range and 128 × 128 in azimuth) was defined on the master image to compute the cross-correlation function, and (3) the residual parametric shift was estimated and the proper shifts were applied. To increase the signal-to-noise ratio (SNR) of the interferograms (more reliable coherence estimation) and obtain squared pixels, a multi-looking factor of 4 × 1, leading to the pixel size of 13.27 m × 13.8 m, was used. To smoothen the interferograms, the Goldstein filter was applied before the final interferograms' unwrapping. Two coherence thresholds (CC) of 0.2 and 0.35 were used for phase unwrapping (PhU). The 2D PhU is based on the MCF algorithm with a regular grid covering the data extent [46], while the Delaunay MCF (hereafter named 3D

PhU) utilizes a Delaunay triangular network, only considering pixels with coherence values above the unwrapping (CC) set in the unwrapping step. To this end, 3D PhU is performed through two steps: (1) a "temporal" unwrapping operation based on the MCF approach for each arc, connecting neighboring pixels on the perpendicular baseline and time grid ($B_{perp} \times T$), and (2) utilizing the results of the first step to operate a "spatial" unwrapping on each single interferogram on the range and azimuth grid (R×A) [47]. In the 3D PhU, each pixel is unwrapped if its coherence value is above the CC in at least 75% of the pairs in the Delaunay connections, leading to an increase in the robustness and reliability of the unwrapping process. In order to reduce unwrapping error due to the low coherence area, a decomposition level (DL) processing was exploited. The DL operates data multi-looking and under-sampling in an iterative way to unwrap the interferograms at a lower resolution and then reconstruct them back at the original resolution [45]. A third-degree polynomial was applied to the selected 30 reference points to estimate and remove the phase constant and ramp during the refinement and reflattening steps. The reference points were selected outside the actively moving landslide area on highly coherent pixels (i.e., more than 0.8), where unwrapped values showed no residuals and jumps. The selected points were mainly located in the permanent settlement area of Corvara and on the surrounding mountains of the landslide, where no displacement is expected. Then, 15 out of the 30 points (including 12 points over the urban area) were chosen as stable points. Finally, the pixel values were interpolated using a 4th cubic convolution interpolation, considering 16 surrounding pixels with interpolation and mean window sizes of 7 and 3, respectively, to derive an area-wide spatially comprehensive displacement map.

Two steps of inversion were performed in order to estimate the landslide velocity field. In the first inversion step, the SBAS inversion kernel was implemented to retrieve the first estimate of the displacement rate and residual topography ($\Delta\varphi_{topo}$) using a linear model [16]. In the second inversion step, after the initial estimation of the displacement time series, a custom atmospheric filtering was defined and applied to the results of the previous step in order to estimate and remove the atmospheric contribution ($\Delta\varphi_{atm}$). with The filter window sizes of 1200 m and 365 (days) were set to take into account spatial and temporal atmospheric variations, respectively. Finally, the displacement time series and mean displacement map obtained were geocoded according to the UTM reference system.

Finally, the spatial displacement patterns were analyzed and compared to DGNSS data from field observations. Based on the DGNSS time series, 3D displacements were computed and projected in the 1D line of sight (LOS) of the satellite, enabling direct comparison with DInSAR results. The decomposition of the LOS displacement vector described in the East–North–Up reference system is [0.64, 0.17, 0.74], according to a descending S1 incidence angle $\theta_1 = 42.2°$ and a satellite path azimuth $\alpha = -165°$ (counter-clockwise to the North) [48]. As the decomposition LOS vector shows, the InSAR system is more sensitive to the Up component (i.e., 0.74) rather than East one (i.e., 0.64) and presents the least sensitivity to the North component, whereas DGNSS system indicates more sensitivity to the East–North plane rather than the Up component.

$$U_{LOS} = \begin{bmatrix} U_e \\ U_n \\ U_u \end{bmatrix} \begin{bmatrix} -\sin(\theta_1).\cos(\alpha_h) \\ \sin(\theta_1).\sin(\alpha_h) \\ \cos(\theta_1) \end{bmatrix} \tag{4.1}$$

4.4 Results

4.4.1 Sentinel-1 DInSAR Analysis

S1 acquisitions were analysed according to meteorological data and perpendicular baseline values for reducing the temporal decorrelation of the DInSAR results. Area-wide snow cover was observed before January 10, 2015 and between January 15 and May 15, 2016 in the meteorological time series. Figure 4.3A-D presents the S1 images at their particular acquisition date and their connections between each other to create interferometric pairs. The selected acquisitions are displayed as slave datasets (green points) and the master (yellow point). Due to the difficulty retrieving phase information from pixels with coherence values lower than 0.2, the pairs with a mean coherence lower than 0.2 (calculated within the landslide boundary) were removed from the graph presented in Figure 4.3A. Six acquisitions were identified as snowy data including 28 January 2015, 04-28 February 2016, 11-23 March 2016 and 04 April 2016 and the final connection graph is obtained (Figure 4.3C). After applying the mean coherence threshold of 0.2 for discarding the incoherent pairs and removing the snowy acquisitions (end of 2015 and spring 2016), we observed a few connections at this part of the network (red points in the Figure 4.3C), which could potentially lead to phase ambiguity in the phase unwrapping step. To overcome this problem as best as possible with the data available we needed to have more connections with respect to the other part of the network due to the longer temporal baseline caused by removing the snowy data. To this end, we decided in this time interval to lose the constraints (i.e., 0.2 threshold) in order to preserve more connections. Therefore, the connections with a mean coherence value lower than 0.2 (i.e., 0.18 up to 0.2 within the landslide boundary) were used (Figure 4.3C). Delaunay connections for 3D phase unwrapping has shown in Figure 4.3B.

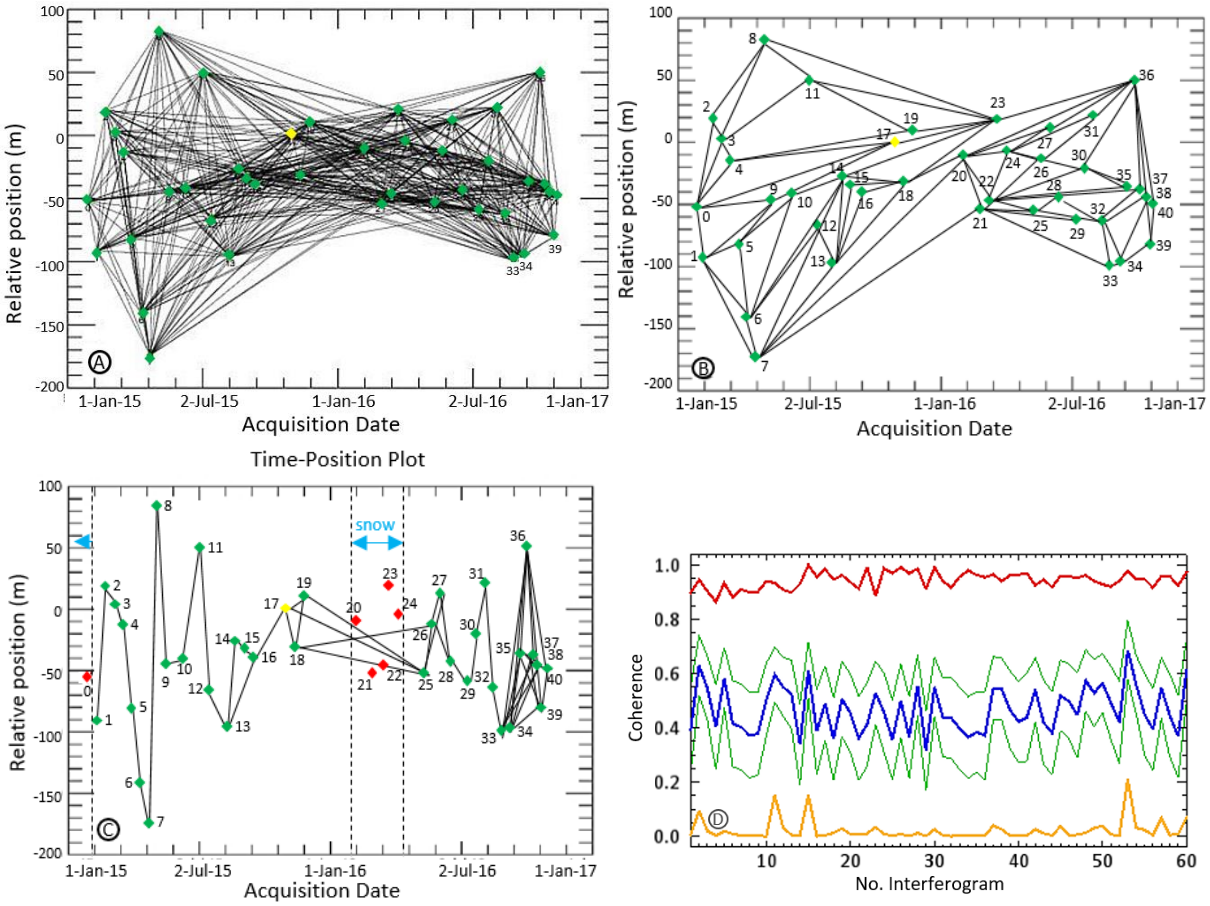

Figure 4.3: S1 SAR acquisition connections. (A) Perpendicular baselines (indicating a maximal spatial baseline of 174 m) between different image acquisitions according to their relative position (570 interferograms; yellow and green points indicate the master and slaves, respectively); (B) Delaunay connections for 3D phase unwrapping; (C) final connection graph after discarding pairs with a mean coherence less than 0.2 (the gray dashed lines present the snow time span, the black lines between acquisitions show the remaining connections, and the red dots indicate the discarded data); and (D) min/max (orange/red colors), mean-Std/mean+Std (green colors), and mean (blue color) coherence (within the landslide boundary) of the remaining pairs (i.e., 60 interferograms) after the graph editing.

The positive effect of using a shorter temporal baseline (6 days obtained by adding the Sentinel-1B data) in increasing the interferogram quality and coherence is observed in Figure 4.4A and B. The low coherence values observed in the Corvara area shows the negative effects of decorrelation caused by vegetation (Figure 4.4C and D) and snow (Figure 4.4E and F).

B).

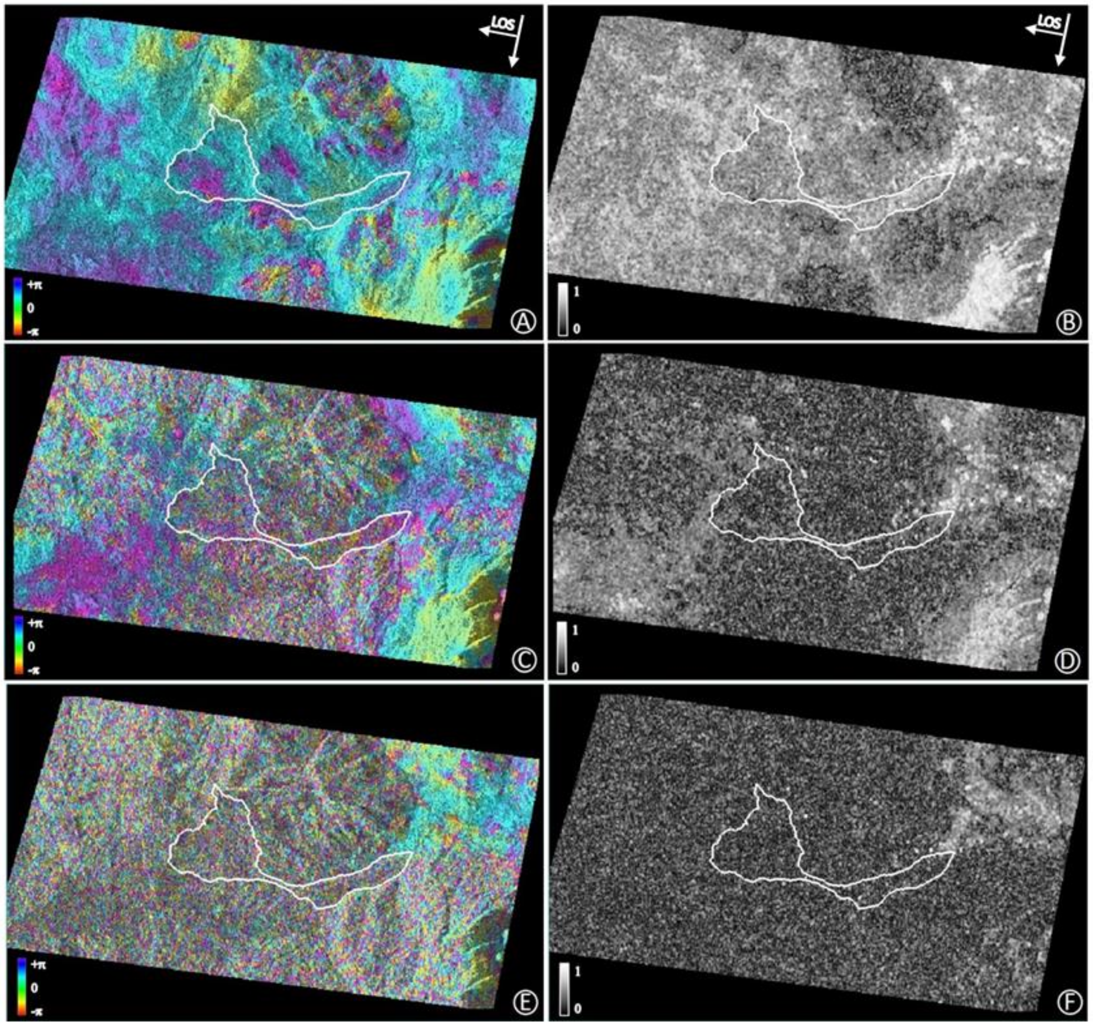

Figure 4.4: The effect of seasonal, temporal baseline, and surface scatterers' decorrelation on phase (left) and coherence (right). (A) Coherent interferogram showing the effect of the short baseline (i.e., 6 days) on the phase and (B) coherence related to the pair of 19–25 Oct 2016. (C) Phase values affected by decorrelation caused by vegetation and (D) coherence related to the pair of 6 June–3 July 2015. (E) Phase values affected by decorrelation caused by snow and (F) coherence related to the pair of 2–28 February 2016. The white polygon shows the boundary of the Corvara landslide. All images are presented in the SAR geometry.

Figure 4.5A and B present the coherence (with a threshold of 0.2) and displacement maps along with the locations of 8 GNSS stations and 30 reference points. The following convention for presenting displacement values is used in Figure 4.5B: i) the negative values refer to an increase of sensor-to-ground distance and ii) the positive values indicate a decrease of sensor-to ground distance. The stations no. 13, 28, 53, 54 and 56 were excluded from SBAS processing because their displacement rate is too high to be quantified using the presented data and SBAS technique. The results show the spatial dispersion of phase and coherence values mainly located on the toe of the landslide and urban areas where no data are represented in black color (Figure 4.5A and B).

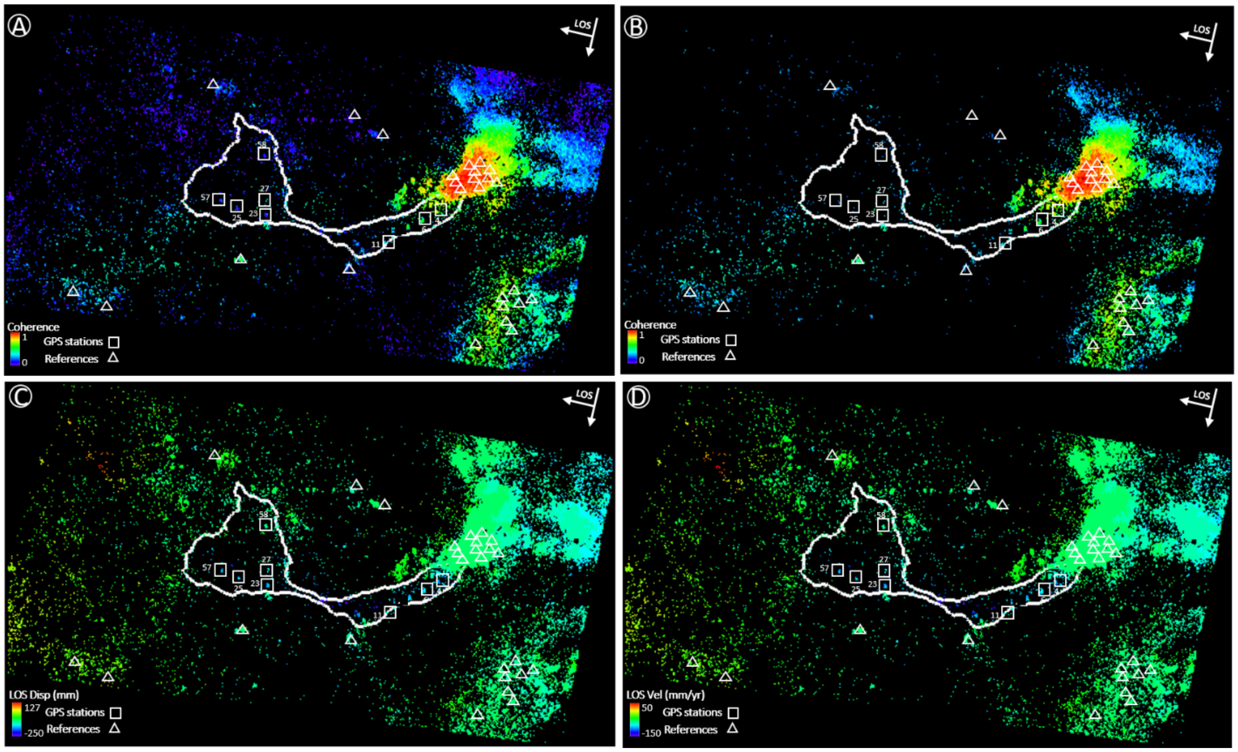

Figure 4.5: Coherence and displacement maps before the geocoding step. (A) Coherence map (threshold of 0.2). (B) Coherence map (threshold of 0.35). The positions of 8 DGNSS stations and 30 reference points selected for the refinement step (ramp and phase constant removal) are presented on the coherence map. (C) Cumulative line of sight (LOS) displacement map and (D) mean LOS velocity map (both created with the coherence threshold of 0.2 and 2D unwrapping method). The locations of 8 DGNSS stations and 30 reference points are presented on the displacement map. The images are presented in the SAR geometry.

Figure 4.6 shows the differences of mean LOS velocities obtained with four combinations of CC and PhU techniques. Spatial displacement patterns are similar at the middle part of the landslide (blue colour) and differ at the depletion areas (eastern part of the landslide in Figure 4.6), depending on the chosen processing parameters. According to negative velocity difference values, the propagation of the displacement flow from East to West is clearly visible in Figure 4.6A-D. Whilst a higher velocity peak (i.e. around 120 mm/year) is obtained with the lower CC and a 3D PhU processing, warm colours are visible on the northern depletion area and very little displacement is observed in the eastern depletion area (Figure 4.6). However, the frequency of negative values (mainly considering western direction displacement) is more pronounced considering a higher CC and a 2D PhU (Figure 4.6A and C). It seems that “more successful” is due to “frequency of negative values”, in reality, the motivation is the agreement with GNSS measurements: “frequency of negative values” is a consequence of that point. The a-b cross-section comparison of interferograms confirms that using 2D PhU (followed tightly by 3D PhU) induced higher frequency of negative values, especially in the eastern depletion area, while considering a higher CC (green line in Figure 4.7).

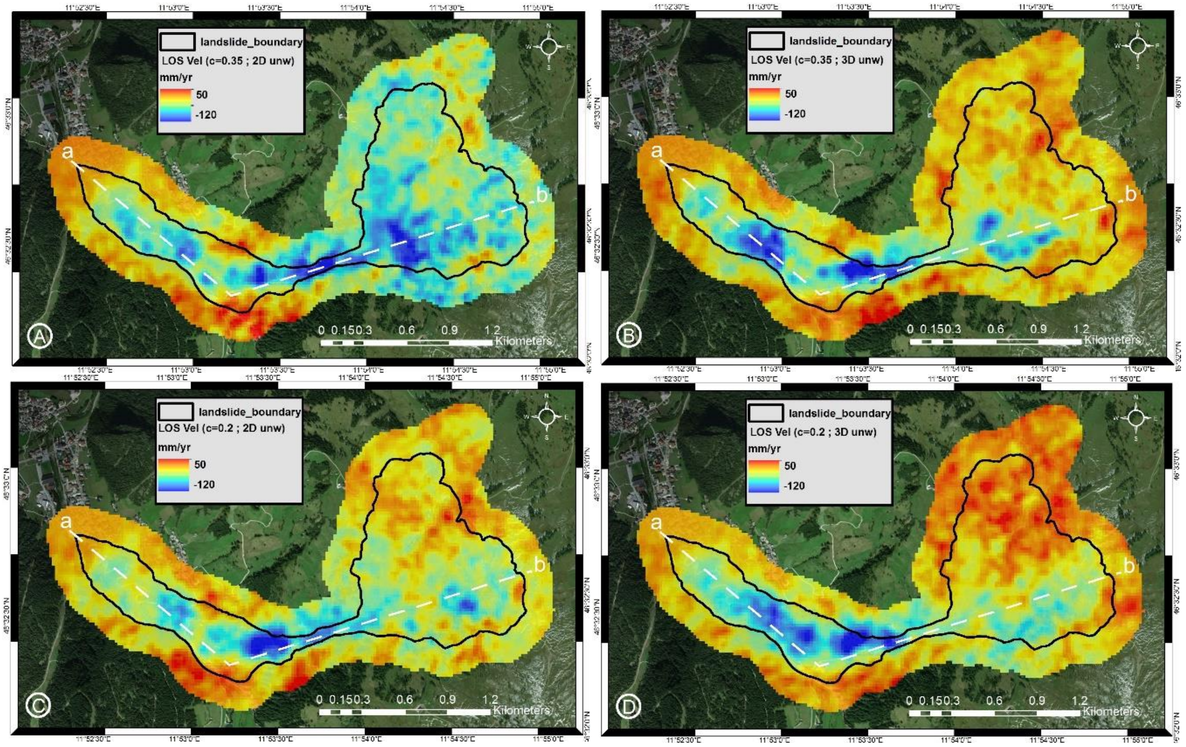

Figure 4.6: Comparison of interpolated SBAS LOS velocity maps (A) with an unwrapping coherence threshold (CC) of 0.35 and 2D PhU, (B) with CC of 0.35 and 3D PhU, (C) with CC of 0.2 and 2D PhU, and (D) with CC of 0.2 and 3D PhU. The spatial interpolation applied to the results of the DInSAR processing chain is meant to spatially preserve the results' continuity, avoiding discontinuities between pixels of low coherence. The figures show the terrain-corrected results in the UTM reference system.

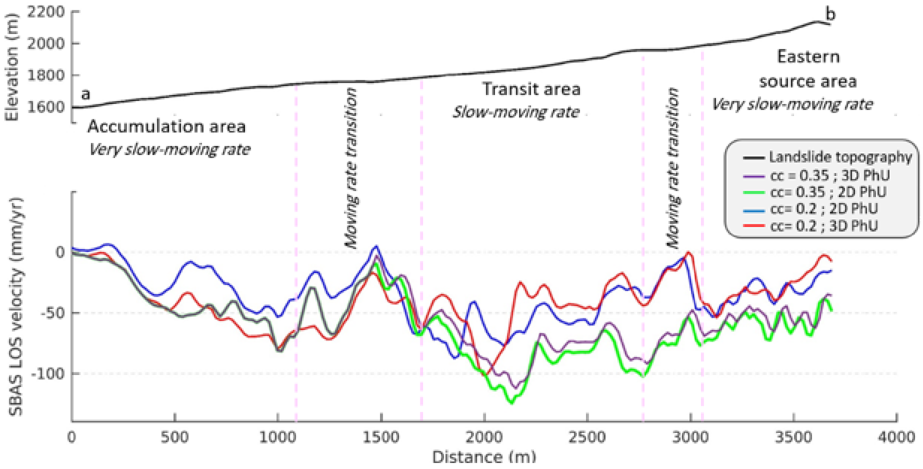

Figure 4.7: Cross-section comparison of DInSAR results and landslide movement rates. CC represents the coherence thresholds and PhU the phase unwrapping process. The topography profile a–b is divided into (1) an accumulation area, (2) a first transition, (3) a transit area, (4) a second transition, and (5) a source area. Since the movement direction of the right side of the landslide, corresponding to the "b" profile, is not aligned to LOS (based on the DGNSS measurements of Figure 8), the SBAS velocity for this part of the landslide was projected to the "b" profile alignment to avoid underestimating the velocity. The green and purple lines overlapped each other at the left part and then separated at the distance of 1500 m.

4.4.2 DGNSS Monitoring Results

Figure 4.8 shows the mean annual horizontal and vertical velocity as well as the azimuth angle of the DGNSS benchmarks on the Corvara landslide. Station number 8 has been disturbed several times between October 2015 and November 2016 and therefore it had to be excluded. Time series of measured 3D displacements at 13 stations from the source, track and accumulation zone are plotted in two different charts (Figure 4.8). The 3D displacements measured in 2015 and 2016 range from 176 mm (at station 6 in the accumulation zone of the landslide) to 4956 mm (at station 56 in the source zone of the landslide).

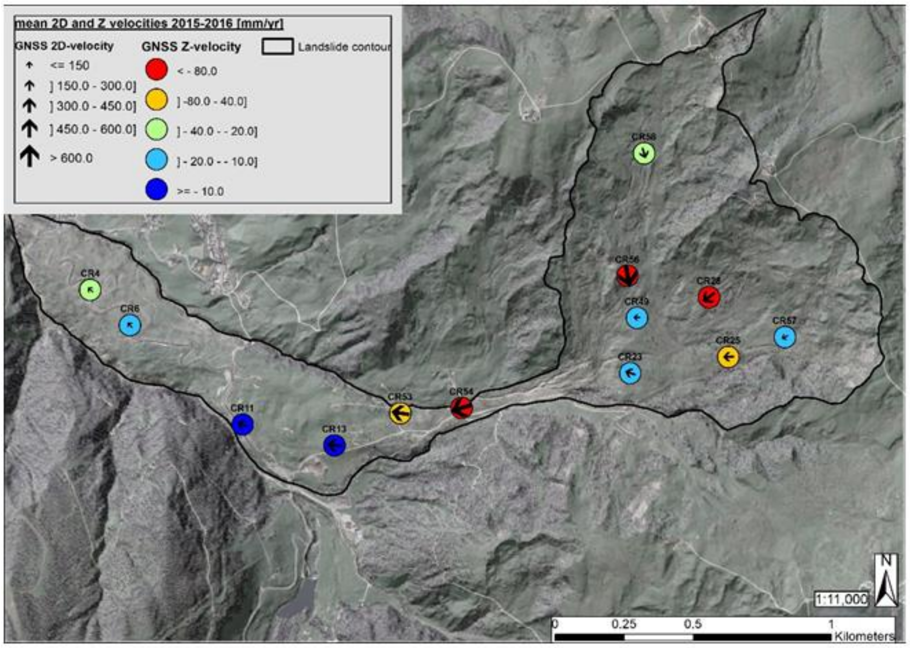

Figure 4.8: Vector direction and velocity rate of DGNSS benchmarks for 2015 and 2016.

For the DGNSS stations in the source zone (23, 28, 49, 56, 57, and 58), a deceleration during winter and an acceleration during spring and summer months can be observed (Figure 4.9). The displacement follows the rainfall rates, which could be explained by the fact that at the upper zone of the landslide, [92] found the groundwater table to be close to the surface. It can be assumed that this favors a quick response of the terrain to rainfall in terms of movement. Regarding the track zone, the movement pattern of the stations 13, 53 and 54 does not follow a seasonal trend but shows a steadier movement behavior.

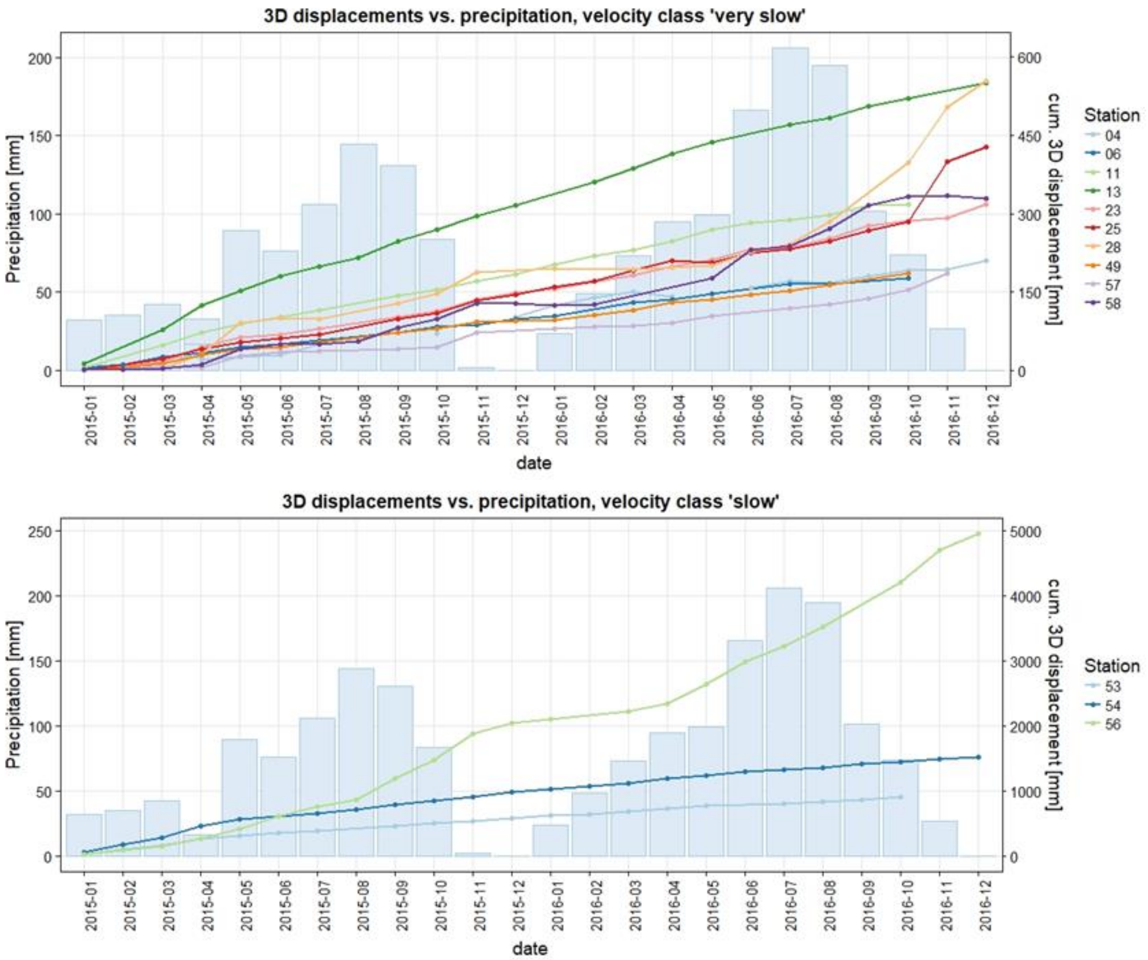

Figure 4.9: Cumulative monthly 3D displacement measured at permanent DGNSS stations (lines) compared with measured mean precipitation (bars).

Figure 4.10 shows a decreasing trend of velocity measured at some benchmarks (e.g. station 54). This might be attributed to the excavation of a drainage channel network, which was initiated in 2014 by the Corvara municipality and repeated on a yearly basis. However, more detailed surveys would be necessary to provide empirical evidence on the effectiveness of this drainage system. For many stations, with exception of 56, a trend of deceleration can be observed over the shown period. Already [90] noticed that the landslide kinematic intensity has decreased in general.

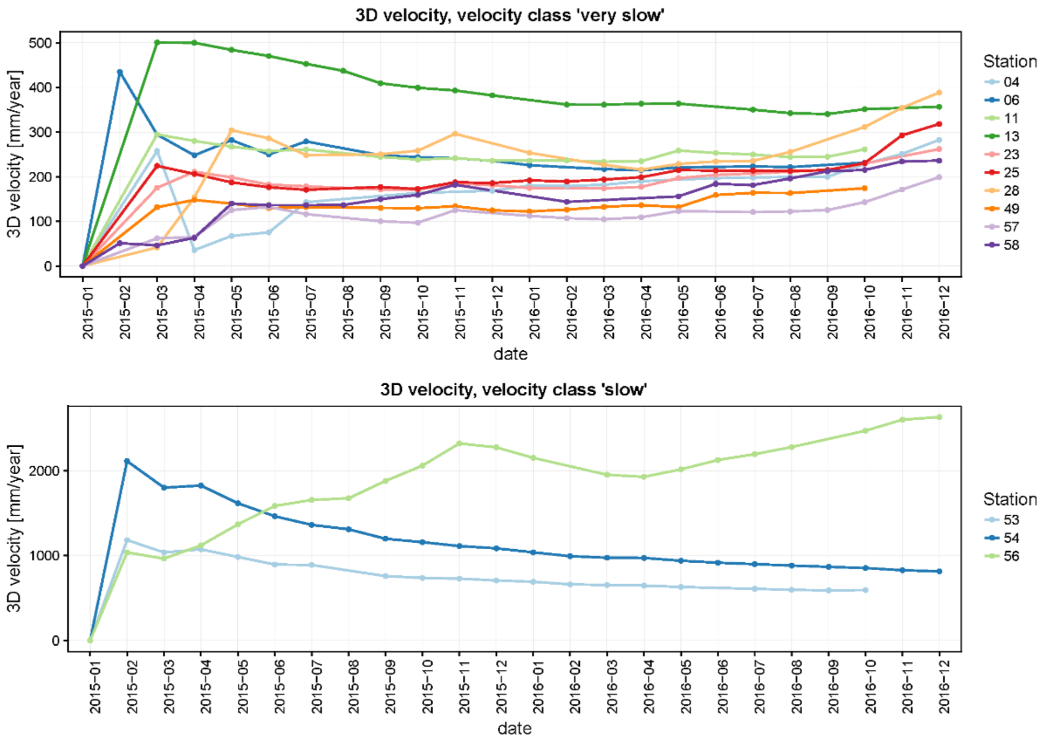

Figure 4.10: 3D displacement velocities between September 2013 and December 2016 at selected DGNSS stations.

4.4.3 DInSAR and DGNSS Results Comparison

As an indication of measurement differences by ground-based instruments and DInSAR, the cumulative displacement of the stations 4 (located at the toe of the landslide) and 57 (located in the eastern depletion area) are represented in Figure 4.11. The CC of 0.35 with 2D and 3D PhU methods was used to create the plots. The frequency and acquisition dates of monthly GNSS and SAR data were not identical. Therefore, the DGNSS measurements were approximated by a linear model to make them comparable with the SBAS results. Such as observed previously, the 2D PhU gives measurements closer to the ground truth (red and green triangles in Figure 4.11).

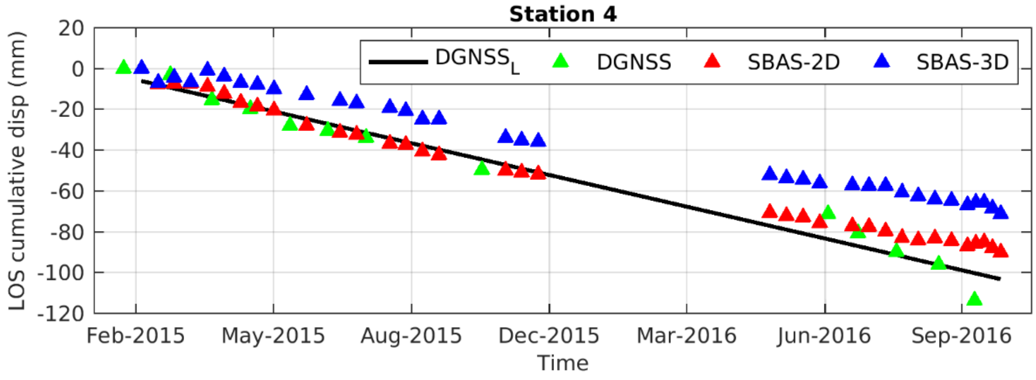

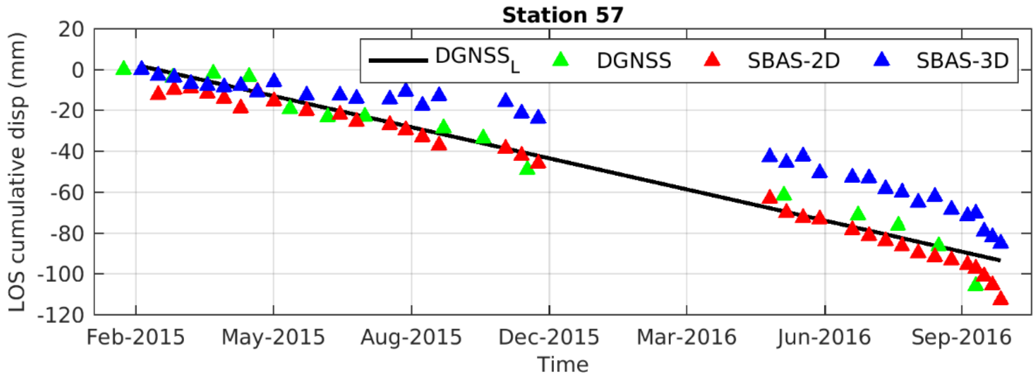

Figure 4.11: Comparison of SBAS and DGNSS time series results. LOS cumulative displacement of the stations 4 and 57 is with a coherence threshold of 0.35. The DGNSS-fitted line (DGNSSL) is indicated in the figure, and the data-free area (i.e., from December 2015 to April 2016) indicates the snow period. SBAS-2D and -3D present the phase unwrapping method applied to the SBAS processing.

The cumulative LOS displacement and the validation plot for the estimated velocity using different coherence thresholds and PhU parameters are presented in Figure 4.12A and B, respectively. SBAS results underestimate the displacements of the stations 4 and 58, estimated the displacements of the stations 6, 49 and 57 with a close agreement and estimated the displacements of the stations 11, 23 and 25 with a relatively low accuracy (Figure 4.12A). Generally, 2D and 3D PhU with the CC of 0.35 outperformed among other setting used, respectively. Compared to other parametric configurations, a 2D unwrapping in higher coherence areas (i.e. blue points in Figure 4.12B) represents better the real displacement of 8 selected DGNSS benchmarks according to measurement accuracy while located closer to the 1:1 line.

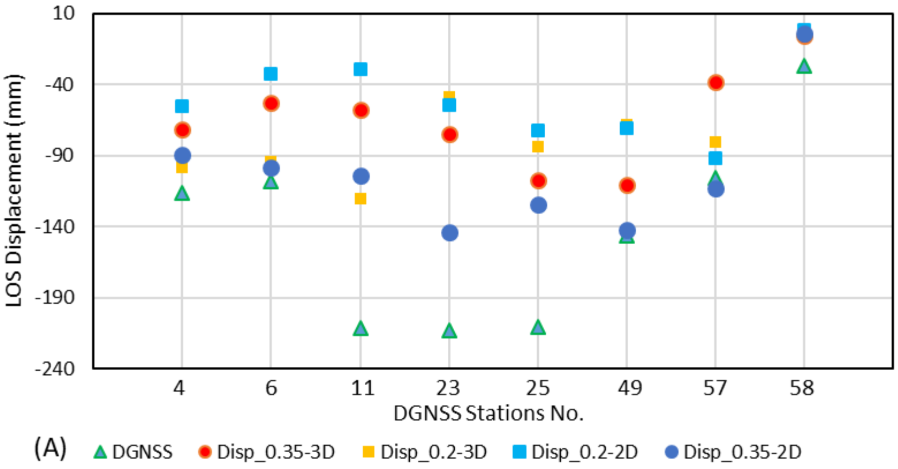

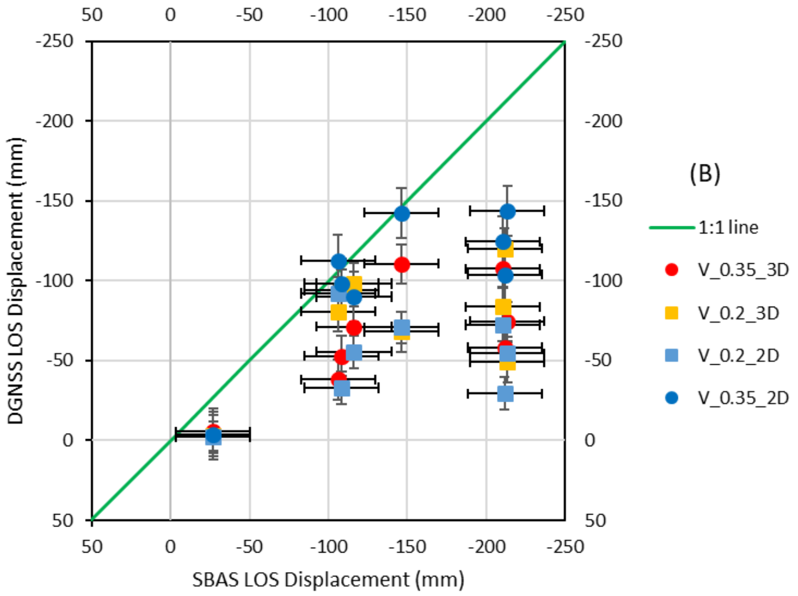

Figure 4.12: Comparison of SBAS and DGNSS time series results. LOS cumulative displacement of the station 4 and 57 with a coherence threshold of 0.35. The DGNSS-fitted line (DGNSSL) indicated in the figure and the data-free area (i.e., from December 2015 to April 2016) indicates the snow period. 2D and 3D present the phase unwrapping method applied to the SBAS processing.

The comparison between DGNSS and SBAS displacement values projected in the LOS direction is presented in Table 2. The RMSE value is maximal (i.e. equal to 9) when considering a CC of 0.2 and 2D PhU and minimal (i.e. of 6.1) when considering a CC of 0.35 and 2D PhU. The RMSE value of 3D PhU with CC =0.2 (i.e., 7.8 mm) is lower than 3D PhU with CC =0.35 (i.e., 7.9 mm). This implies that from the PhU method point of view, 2D PhU generally outperformed 3D PhU, where a higher coherence threshold was used, while 3D PhU nearly provided an identical result for both CC threshold thresholds with a relative superior of CC=0.2. This means that 2D PhU is a coherence-sensitive operator (refer to quality of pixel phase information) and 3D PhU is a pixel-dependent operator (refer to quantity of pixel numbers), where the number of pixels is masked by setting the lower coherence threshold.

Table 4.2: Comparison of DGNSS and SBAS LOS Displacement (D) in mm. RMSE value shows accuracy of each unwrapping methods with the different coherence threshold.

CR No.	**DGNSS**	**DSBAS (0.35; 3D)**	**DSBAS (0.2;3D)**	**DSBAS (0.2;2D)**	**DSBAS (0.35;2D)**
4M	-116.1	-71.24	-98.25	-55.52	-89.88
6H	-108.3	-52.87	-94.09	-32.79	-98.18
11H	-211.5	-57.92	-120.14	-29.3	-103.75
23	-213.4	-74.49	-49.08	-54.44	-143.7
25	-210.3	-107.44	-83.58	-72.22	-124.35
49H	-146.2	-110.57	-68.13	-70.65	-142.5
57M	-105.9	-38.04	-80.71	-92.02	-112.74
58H	-27.1	-5.45	30.5	22.28	-49.17
RMSE		7.9	7.8	9.0	6.1

4.5 Discussion

DGNSS measurements show different mean velocities in (i) the area of depletion (e.g. 174-2633 mm/yr) with acceleration phases observed in late summer/fall 2015 and spring 2016, (ii) the track zone (e.g. 356-814 mm/yr) with a relatively constant displacement behavior and (iii) the accumulation zone (e.g. 231-261 mm/yr) with an acceleration phase during the first half of 2016. This variation of the landslide displacement in relation to snowmelt, precipitation and groundwater conditions should be investigated more in depth.

The application of 2D PhU provided results closer to the ground truth measurements while 3D PhU has proven to avoid phase jumps [127]. Hooper and Zebker [137] also used a stepwise 3D PhU algorithm finding reasonable results, whereas for cases without multiple cycle of phase discontinuities (or jumps), no improvement was measured with 3D PhU. In this research, many pairs in the connection graph were discarded (Figure 4.3) due to the low coherence found in the landslide area (e.g. Figure 4.4F). Therefore, the 3D PhU, including temporal information to help unwrapping in low coherent interferogram areas, was not beneficial due to the low redundancy of the connection graph. Hence, the standard 2D unwrapping with a coherence threshold of 0.35 leads to fewer pixels but to a more reliable pixel selection. A resulting lower effect of the eventual phase jumps leads to measurements closer to the ground truth.

The RMSE values indicate a low accuracy in several points and SBAS results affected by the considerable errors, leading to an overall underestimation and a failure to detect fast moving areas. Several factors led to propagating the error into the results, which could considerably affect the precision of the GNSS measurements and accuracy of the SBAS results. These error sources can be expressed as three following categories: i) DGNSS–related error, ii) non-LOS landslide displacement and iii) atmospheric artifact. As the DGNSS antenna was mounted on the metal bar of the CR structure, slight changes results from the landslide movement led to an antenna tilting within the span time of our study. Since the Phase Center Variation (PCV) of GNSS antenna is calculated in the vertical position; any deviations from the vertical position of the antenna induce a bias in the measurement leading to a low precision. This bias could manifest itself as a higher discrepancy (low accuracy) between SBAS and GNSS results (i.e. lower accuracy or higher RMSE values). This could be explained the low accuracy obtained from SBAS results (e.g., stations 4, 11, 23 and 25).

The second error source is related to the SAR system geometry in relation to the real displacement field. The SBAS displacement has been estimated along the LOS of the satellite, while the direction of the landslide movement of depletion areas (in the Eastern and Northern parts) is not aligned to the LOS. Therefore, only a fraction of the occurred displacement is retrieved by SAR system (e.g., stations 23 and 25). In particular, North-South oriented movements of the North-Eastern part of the landslide are barely detectable by DInSAR technique (e.g., station 58). Due to the complexity of the motion pattern, Multi Aperture Interferometry (MAI) techniques could be an alternative method to extract nearly North-South movements to be integrated to the LOS-based results [138].

Another important error source propagated in SBAS results is the phase delay caused by the atmosphere that often affects the displacement signal. Indeed, the spatial and temporal variations of atmospheric properties over the case study cannot be precisely known by the temporal and spatial window sizes of the high and low pass filter in the SBAS processing. Therefore, the delay cannot be fully estimated and removed from interferograms by filtering approach, especially in high topographic region like Alpine, whereas the turbulent and stratified components of atmosphere are constantly changed in time and space. In such circumstances, some sophisticated methods for atmospheric correction can be used such as phase-based (e.g., linear model) and using auxiliary weather data such as Moderate Resolution Imaging Spectroradiometer (MODIS) and ERA data provided by ECMWF (European Center for Medium-Range Weather Forecasts) to mitigate the atmospheric artifacts.

4.6 Conclusions

Multi-temporal SBAS using Sentinel-1 imagery works relatively well for recognizing recent moving areas even if decorrelation might be high, mostly due to vegetation and changing meteorological conditions in mountainous environments. The combination of a coherence threshold of 0.35 and 2D PhU gives results closer to the ground-truth measurements with maximal velocities of around 115 mm/yr. Therefore, using 2D PhU seems to minimize the total length of discontinuities in the unwrapped phase for this landslide site. However, no reliable SAR velocities were detectable on south-facing slopes because the displacement orientation is nearly perpendicular to the LOS direction.

During the period investigated, it was not possible to completely exploit both S1A and B, while S1B was not operational yet (at the data processing time). Further analyses are ongoing combining both SBAS and PSI with complete Sentinel-1A/B time series in order to reduce decorrelation occurring over time. New artificial 1-m edge CRs were installed on the landslide in late summer 2017. Despite an initial backscattering signal of 6.9 dB and monthly field campaigns to verify their orientations, their unavoidable tilting seems spoils their systematic recognition over time what makes challenging further PSI processing. Integration of proximal data covering parts for the landslide with remote sensing data are also tested for representing the complex changing slope kinematics assessment in (near) real time.

Chapter 5

5. INSAR ATMOSPHERIC CORRECTION USING PHASE AND WEATHER-BASED MODELS

The aim of this chapter [1] *is to evaluate the performance of four numerical weather models (i.e., ERA-Interim, ERA5, MERRA2 and WRF) and two phase-based techniques (i.e., linear and power law) to estimate phase delay using Sentinel-1A/B data acquired over the Corvara landslide located in the Alps. Eighteen Sentinel-1A/B images in descending orbit and Interferometric Wide swath (IW) mode covering a time period from July 22 to November 1 2017 at the same acquisition time (5:18 A.M. UTC) were collected over the Corvara landslide. The displacement map has been generated using the PSI technique. Then, the GPS data and the GACOS product are used to validate the results. In the end, two indicators metrics; phase std reduction and correlation between phase and InSAR estimated tropospheric delay, were used to determine the performance and robustness of each model*

5.1 Introduction

Tropospheric variation in time and space of water vapor, pressure and temperature causes a phase delay [17]. Spatio-temporal variations of only 20% in relative humidity lead to 10 cm errors and variations in pressure, temperature, and relative humidity in the lower part of the troposphere (< 5 km) could potentially induce up to 15–20 cm interferometric phase delay [17][139][44].

This phase delay could reach approximately several centimeters and often affects the deformation signal [15]. This additional contribution in interferogram results from a turbulent component affected by troposphere dynamics (also called wet delay) and stratification or a long-wavelength component induced by the lower atmosphere parameters such as pressure,

---

[1] Part of this chapter appears in:

[148] M. Darvishi, G. Cuozzo, L. Bruzzone, F. Nilfouroushan, “Performance evaluation of phase and weather-based models in atmospheric correction with Sentinel-1data: Corvara landslide in the Alps,” *IEEE Journal of Selected Topics in Applied Earth Observations and Remote Sensing*, 2018. (under review)

temperature, and relative humidity (also called dry delay) [15][140]. Many studies have been developed to mitigate the negative effects of the turbulent component as random component in space and time in interferograms by applying the temporal and spatial filtering [105][22][106] to time series of SAR data.

In this study, we use phase-based models, including linear and non-linear (power law) models, NWM models including ERA-Interim, ERA5, MERRA2 and WRF, multi-spectral data (MODIS) and GPS data to estimate phase delay on Sentinel-1A/B data and evaluate the performance of them. Three steps are carried out: 1) cross-comparison between the ZTD, ZWD and TWD derived by GPS with its counterparts obtained by NWM-based models, 2) cross-comparison between the InSAR tropospheric phase delays estimated by phase and NWM-based models in a regional scale and 3) cross-comparison between the GPS stations velocity and the velocity corrected by the phase and NWM-based models in a local scale (i.e., the active Corvara landslide in Italy). In addition to the GPS data, we used the GACOS product as reference to cross validate the results in all steps.

5.2 Dataset

Eighteen Sentinel-1A/B images in descending orbit and Interferometric Wide swath (IW) mode covering from July 22 to November 1 in 2017 at the same acquisition time (5:18 A.M. UTC) were collected over the Corvara landslide. Due to the course resolution of weather data and in order to have a better understanding of the tropospheric turbulent and stratified changes, a larger extent of the study area was selected (i.e., 15×15 km) than the portion of the landslide area only (i.e., 3×1.5 km). Figure 5.1 shows the extent of Sentinel-1 data used for tropospheric correction purpose and the boundary of the Corvara landslide. We used four permanent GPS stations as references for both the tropospheric delay estimation and the results validation. The stations No. 8, 54 and 58 located within the landslide boundary were used to estimate the landslide velocity, while CIAM GPS station was utilized to estimate Zenith Total Delay (ZTD), Zenith Wet Delay (ZWD) and Zenith Hydrostatic Delay (ZHD) components of the troposphere in a 2-hourly time span (herein between 4 and 6 A.M.) (Figure 5.1a, b and d). The characteristics of the weather data used in the tropospheric correction are presented in Table I. NWM models involving Era-Interim and ERA5, GFS data (http://rda.ucar.edu/datasets/ds335.0/) and MERRA-2 data (https://gmao.gsfc.nasa.gov/reanalysis/MERRA-2/) were utilized to compute phase delay through pressure, temperature and relative humidity parameters extracted from the NWM models using (2.19). The ZDT was derived from the GACOS service (http://ceg-research.ncl.ac.uk/v2/gacos/), which relies on the HRES data [46].

The total perceptible water vapor parameter derived from MODIS data was used to estimate the wet component of tropospheric delay. A GPS permanent station (CIAM) of South Tyrolean

POsitioning Service (STPOS) managed by Bolzano/Bozen Province were utilized to retrieve the tropospheric parameters. Table 5.1 summarizes the specifications of the data used in this study. Sounding data providing height profile of atmospheric characteristics such as temperature, pressure and relative humidity were used to estimate refractivity with the power law method. These data were derived from the Rivolto station provided by the Department of Atmospheric Science of the University of Wyoming (http://weather.uwyo.edu/upperair/sounding.html).

5.3 Data Processing and Methodology

5.3.1 SAR data processing

The Sentinel-1A/B interferograms were generated by using the software SNAP v6 (ESA Sentinel Application Platform v6), the Permanent Scatterers Processing (PS) was performed by StaMPS v3.3 (Stanford Method for Persistent Scatterers) [141] and the phase and NWM-model tropospheric corrections were carried out by TRAIN v3 (Toolbox for Reducing Atmospheric InSAR Noise) [47].

In the PS processing, 6 main steps were performed: 1) initial PS pixel selection by setting 0.4 and 3×2 values for the amplitude dispersion index and the range/azimuth patch sizes, respectively; 2) estimation of phase noise value for each candidate PS pixel (filter window size of 32x32 pixels with spatial wavelength of 800 m) using the iterative approach; 3) PS pixel selection based on its noise characteristics; 4) refinement of the previously selected pixels using a standard deviation threshold of 1; 5) correction of spatially-uncorrelated look angle error [141].

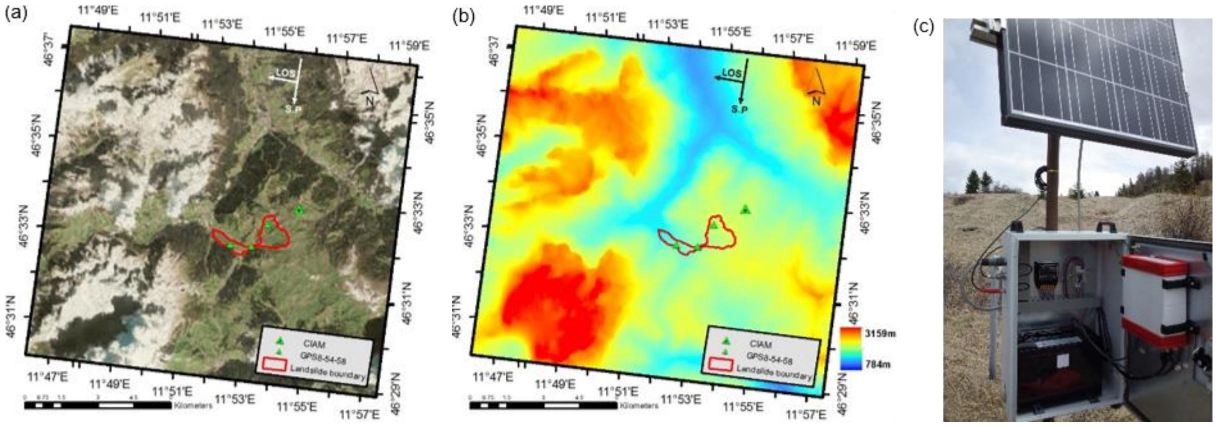

Figure 5.1: Study area and GPS stations. (a) Extent of the Sentine1-A/B image used for data processing and (b) The imaged DEM fom SRTM (30 m) data for the study area. In the both Figs., the extent of the Corvara landslide (with the red boundary), three permenant GPS stations (No. 8, 54 and 58 within the red boundary) and one permanent GPS station belonging to the Bolzano Province (the CIAM located out of the landslide border) are indicated. (c) A photograph showing the CR58 equipments including the battery, GPS receiver and solar panel. The recorded data of each permanent GPS station are transmitted by the mobile network to the servers of the Eurac Institute for Earth Observation.

Table 5.1: Characteristics of GPS, NWM models, sounding and MODIS data

Data/models	Type	Temporal Res.	Spatial Res.	P. lev.	H-delay	W-delay	H+W	Latency
ERA-Interim	weather	6-hourly	79km	37	Yes	Yes	Yes	several months
ERA-5	weather	Hourly	31km	37	Yes	Yes	Yes	near real-time
GACOS (HRES)	weather	6-hourly	9-12km	137	-	-	Yes	near real-time
GFS	weather	3-hourly	5km	37	Yes	Yes	Yes	near real-time
MERRA-2	weather	3-hourly	50km	42	Yes	Yes	Yes	5 months lag
MODIS	spectrometer	daily	1km	-	-	Yes	Yes	60 - 125 minutes
Sounding data	weather	6-hourly	1 station	115	Yes	Yes	Yes	near real time
GPS	pointwise	30 second	4 stations	-	Yes	Yes	Yes	real-time

H and W indicate the hydrostatic and wet components, respectively, while Res. and P. lev. indicate the resolution and pressure level, respectively.

The weather-based models such as ERA-Interim and ERA5 were directly downloaded and the aforementioned parameters were extracted. The GFS data first processed by WRF model using WRFv3 and WPS packages and the parameters of the domain and parent grid ratio were set 2 and 1/5, respectively, leading to nesting a spatial resolution of 5 km [142]. Four weather parameters including temperature (K), pressure levels (P), relative humidity (in %) and geopotential (m) were extracted from all weather-based models to estimate refractivity. Since the hydrostatic components could be calculated up to 25-30 km height to compare the NWM model results with GPS-derived atmospheric parameters, we set 30 km as reference height to estimated refractivity by (2.21). In the case of MODIS data, water vapor infrared band from MOD05_L2 product was used to estimate the wet component of the refractivity. Since the water vapor information in cloudy conditions is not valid, the water vapor infrared bands were masked with the cloud-cover band provided by MODIS data with a probability of 95%. We then applied the threshold of 80% minimum free-cloud coverage to the water vapor infrared band. It turned out that most of MODIS data were rejected under the defined threshold due to the frequent cloud coverage over the study area. This situation did not allow us to go further and estimate interferometric phase delay. Nevertheless, we will present the interferometric phase delay obtained from the non-free cloud MODIS data in the result section.

The same four weather variables were extracted from the sounding data to approximate the parameters of the power law in (2.25). In power law processing, the scaled topography and phase were filtered in different bands using 1D and 2D Fourier band filtering including 9 bands from 500 m to 10 km [43]. As the landslide area is small, we set only one patch to estimate the spatial variable of the power law.

5.3.2 GPS data processing

The CIAM GPS-station data provided by South Tyrolean Positioning Service (STPOS) and corresponding to the Sentinel-1 acquisition days was processed. We processed the data by

GAMIT-GLOBK v10.61 software [143] and used the VMF1 mapping function to estimate tropospheric delay parameters for the time span of 4-6 A.M. corresponding to Sentinel-1 data acquisition time (i.e., 5:18 A.M.). The VMF1 numerical weather model as computed by TU Vienna [144] provides six-hour intervals surface pressure data gridded by MIT in yearly grid files for GAMIT users. The VMF1 mapping function is used to compute the "dry" part of the troposphere ZHD. The ZWD due to water vapor and the local gradient parameters were estimated for CIAM station and for every two hours using GAMIT software. The methodology used in this study is presented in Figure 5.2.

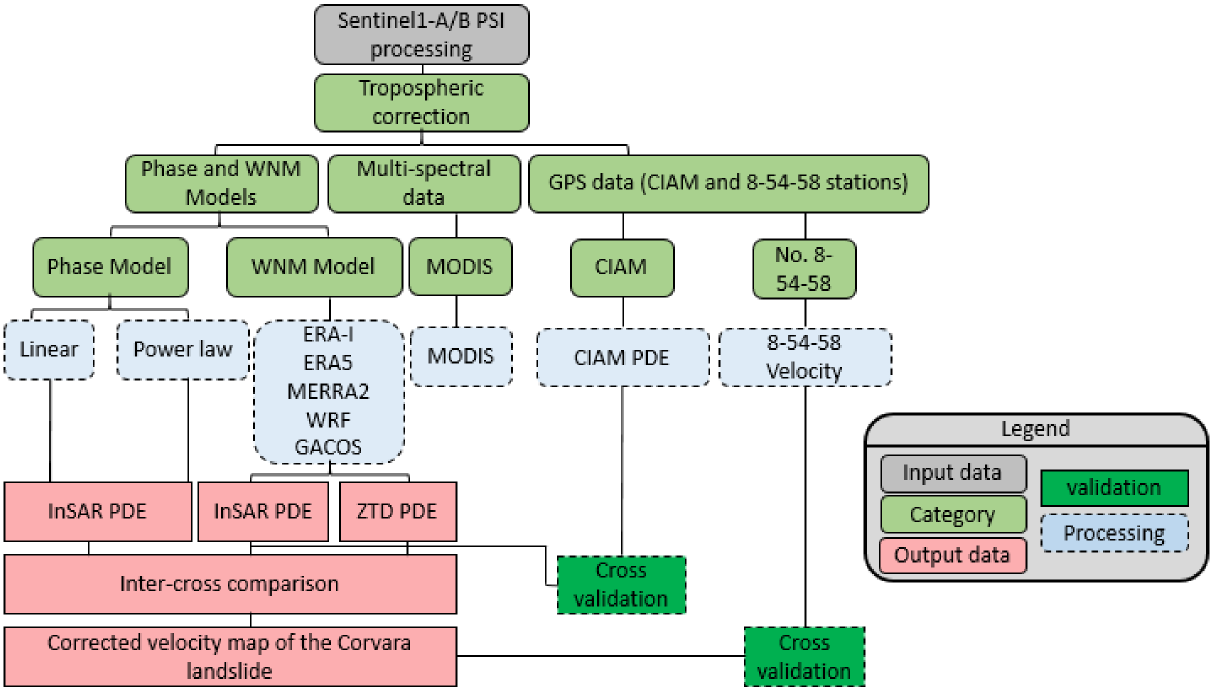

Figure 5.2: Flowchart of the methodology used in the study. PDE refers to Phase Delay Estimation.

5.4 Results

5.4.1 GPS vs. Weather-based model (zenith delay)

In order to evaluate the performance (i.e., accuracy and precision) of NWM models in tropospheric PDE estimation, ZTD, ZHD and ZWD derived by CIAM GPS station were cross-correlated with the same parameters estimated by five NWM models and GACOS result. Since the GACOS provides only ZTD (ZH+ZW) product, hence, only GACOS-ZTD has been compared with ZTD of GPS. Three statistical parameters including: i) root mean square error (rmse), ii) correlation coefficient (R) and iii) standard deviation (std) were used for performance assessment based on the following simple linear models (see (5.4) and Figure 5.3):

$$\text{GPS}_{Z(THW)D} = \text{Slope} \times \text{Weather Models}_{Z(THW)D} + \text{Intercept} \tag{5.4}$$

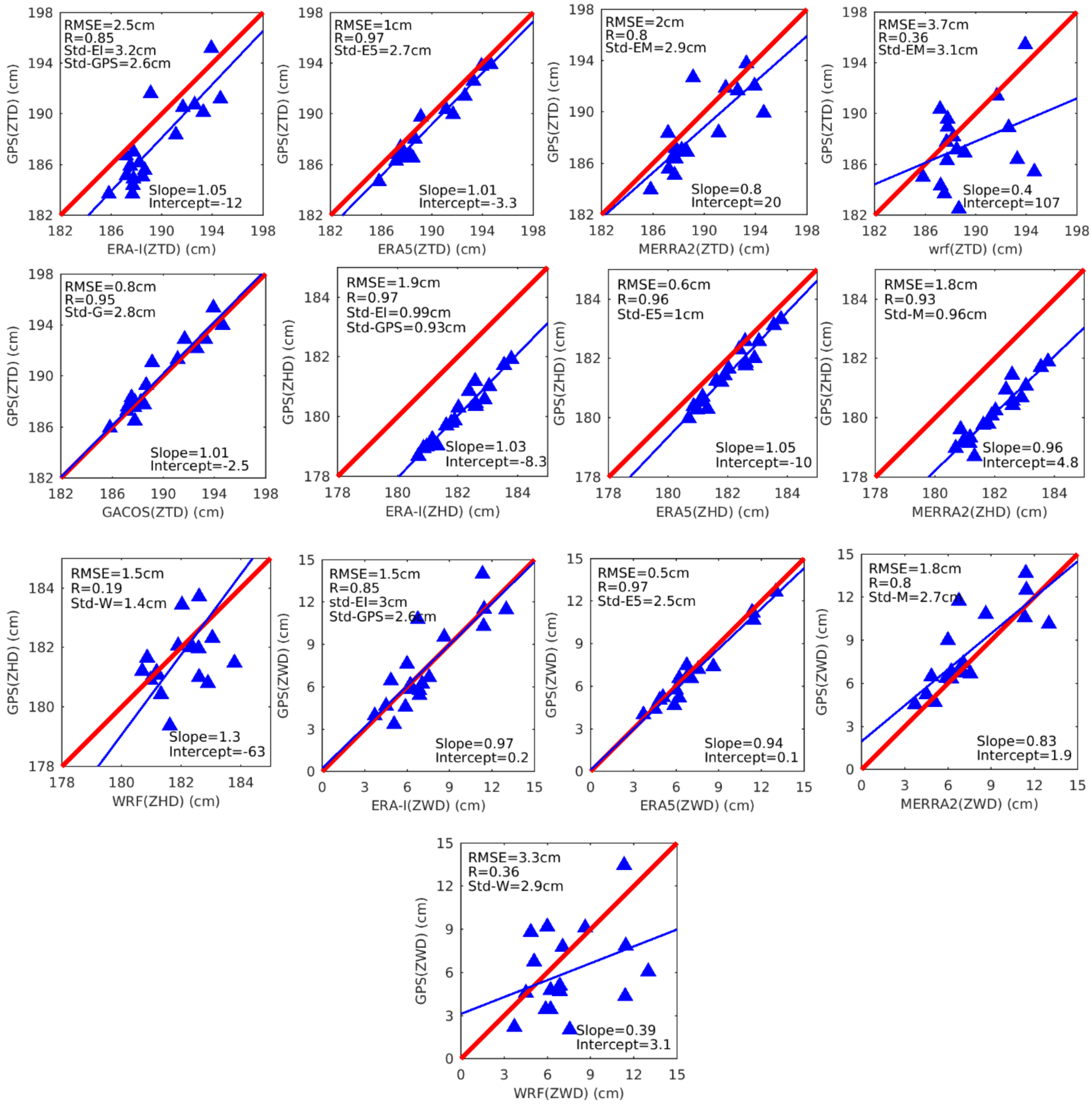

Figure 5.3: The ZTD, ZHD and ZWD parameters of CIAM station vs. ZDT, ZHD and ZWD parameters derived by five NWM models including ERA-Interim (EI), ERA5 (E5), MERRA2 (M), WRF (W) and GACOS (G) (only ZDT). The slope and intercept values (the blue line) of the linear equation and statistical parameters have been estimated for each model. The red line shows the 1:1 line.

In terms of std and rmse parameters of ZTD, ERA5 with the std of 2.8cm and GACOS with the rmse of 0.8cm presented the most precise and accurate results among other NWM models. In terms of std and rmse of ZWD and ZHD parameters, ERA5 generally provided the most precise and accurate results. In all cases, ERA5 presented the highest correlation among other its counterparts.

5.4.2 GPS vs. NWM models (InSAR delay)

To estimate InSAR tropospheric delay, we first projected ZTD on the slant range of SAR geometry by applying the factor of 1/Cosθ, and then applying the factor of -4π/λ to convert from pseudo-range increase to phase delay [15], where θ and λ indicate the incident angle and wavelength, respectively. To achieve the interferometric tropospheric delay the subtraction of tropospheric delay between master and slave acquisition times was used (i.e., $\Delta\varphi_{trop}= \Delta\varphi_{trop}^{slv}$ - $\Delta\varphi_{trop}^{mst}$). This procedure was employed on ZTD derived from the GPS data corresponding to the master and slave dates (Figure 5.4).

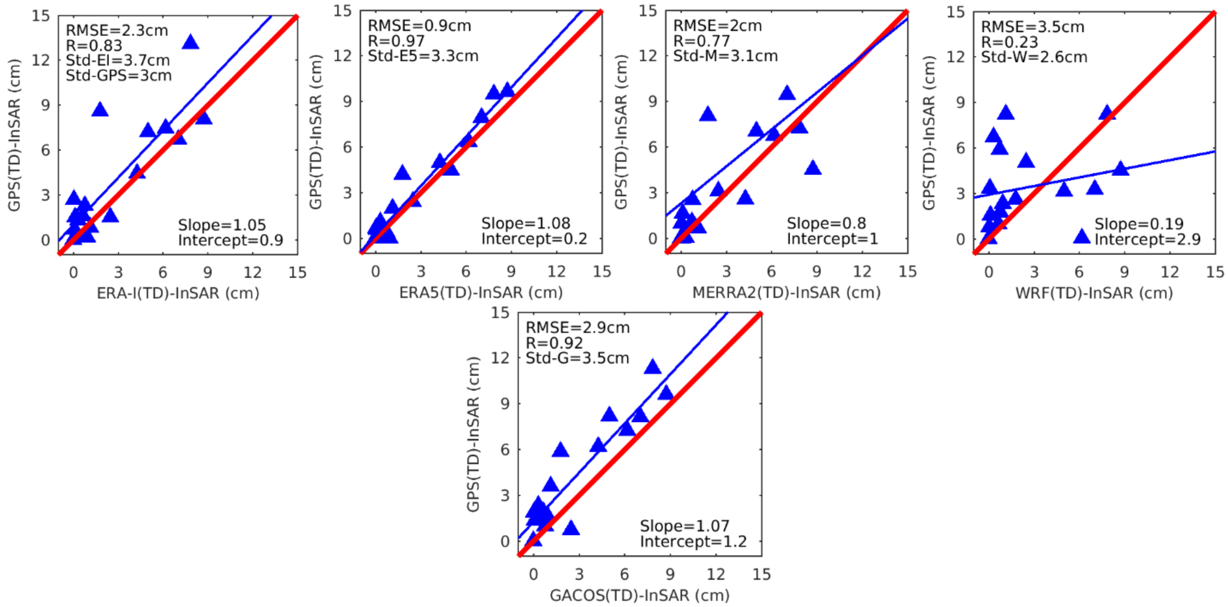

Figure 5.4: Total InSAR Delay (TD-InSAR) vs. GPS (TD-InSAR) for ERA-Interim, ERA5, MERRA2, WRF and GACOS. The TD-InSAR value of WRF model in the interferogram no. 17 appeared as outlier and therefore, it was eliminated from the results.

The map of InSAR tropospheric corrections for 18 interferograms using five NWM models and MODIS data are presented in Figure 5.5. The estimated InSAR tropospheric correction maps for all NWM models generally present a relative qualitative agreement respect to each other and show a high correlation with the elevation in most of the interferograms. Since the wet component obtained by MODIS was under non-free cloud conditions, the related result is not reliable to consider it in the rest of our study.

5.4.3 Phase-based model (linear)

The linear relation between the unwrapped phase and height is plotted in Figure 5.6. The DEM-correlated errors (i.e., correlation between perpendicular baseline and unwrapped phase) were already subtracted from the unwrapped phase. The tropospheric linear delay map estimated using (2.24) is presented in Figure 5.7.

5.4.4 Phase-based model (non-linear)

In the power law model, the power law decay (α_d) and reference height (h_0) parameters were calculated from the sounding data using (2.25) and (2.26) to estimate the interferometric phase delay (see Figure 5.8).

a) Unwrapped phase (U-do)

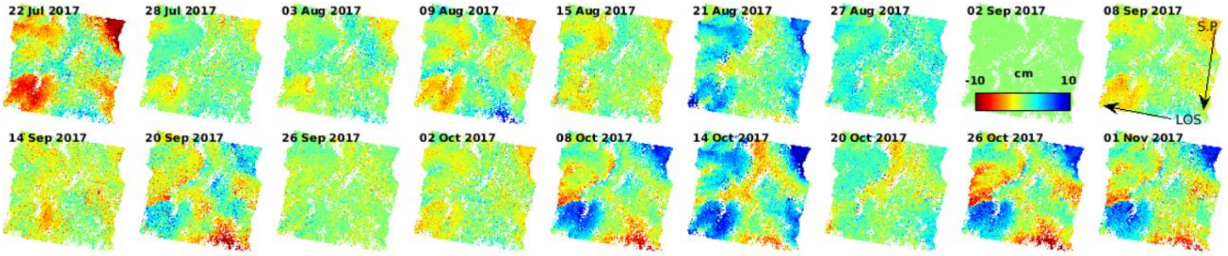

b) Estimated tropospheric delay- ERA-I

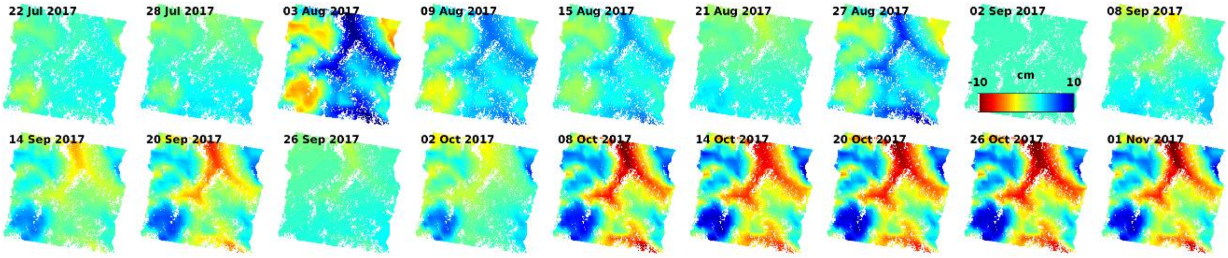

c) Estimated tropospheric delay- ERA5

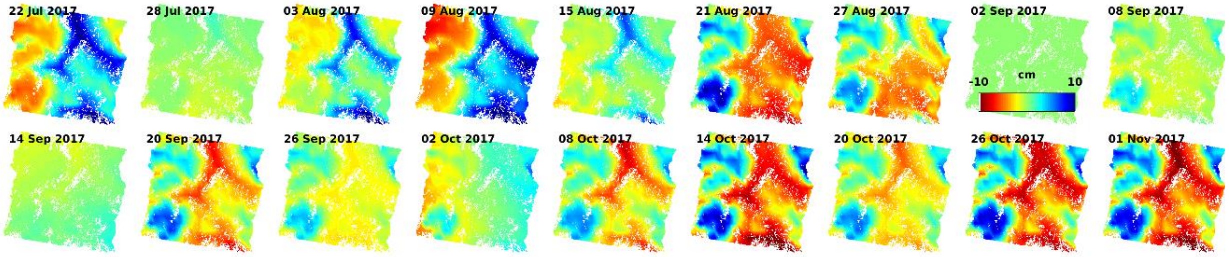

d) Estimated tropospheric delay- MERRA2

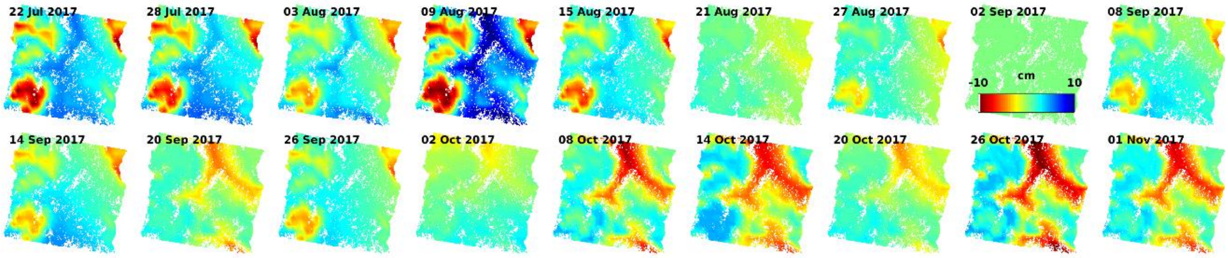

e) Estimated tropospheric delay- WRF

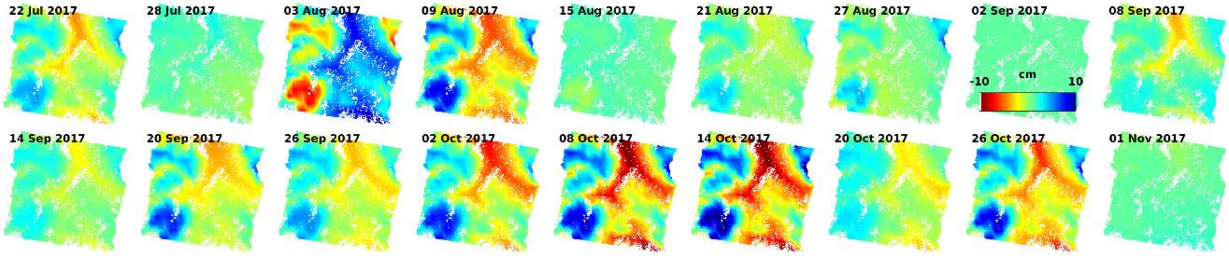

f) Estimated tropospheric delay- GACOS

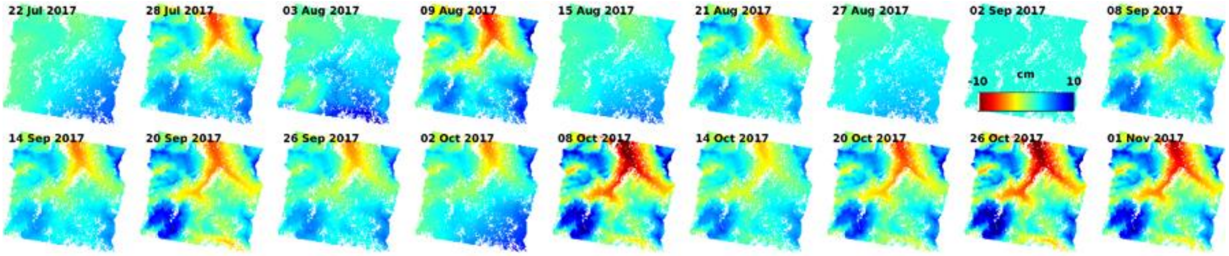

g) Estimated tropospheric delay- MODIS

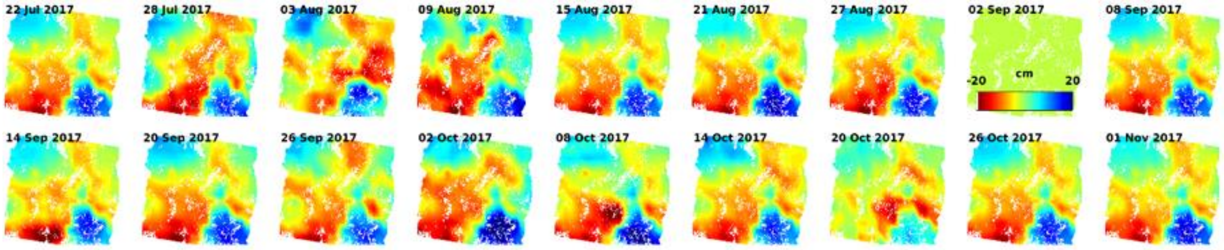

Figure 5.5: Interferometric phase delays of the NWM models and MODIS. The total InSAR tropospheric delays (T=H+W) corresponding to each interferogram of Sentinel-1 data after the DEM and orbital ramp removal (U-do) are shown. The delays derived by MODIS only show the wet component (non-free cloud). The master data (8th interferogram) has no delay (zero). Line Of Sight (LOS) and Satellite Pass (S.P) of Sentinel-1 over the case study are shown in Fig. (a). A same color bar was set for all Figs. to facilitate the comparison, except for the MODIS where the color bar limits went beyond the limits of the others Figs.

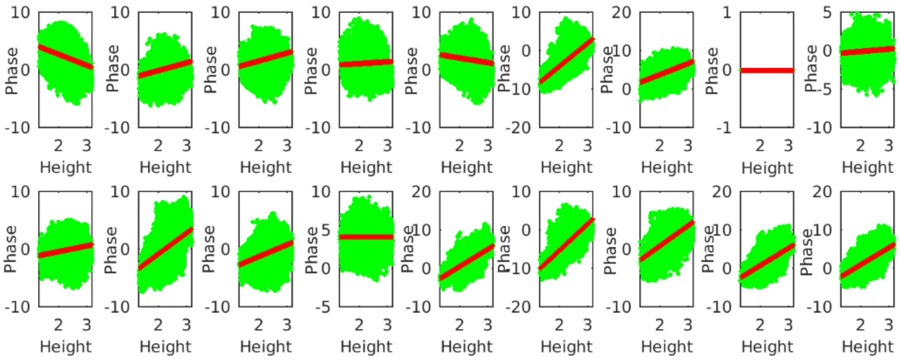

Figure 5.6**:** The linear relation between phase and topography. The relation between height (km) and phase (cm) (green dots), and height and correlated delay estimated from the linear relationship (red line) depicted for each interferogram. The 8th Fig. in the first row indicates the master data.

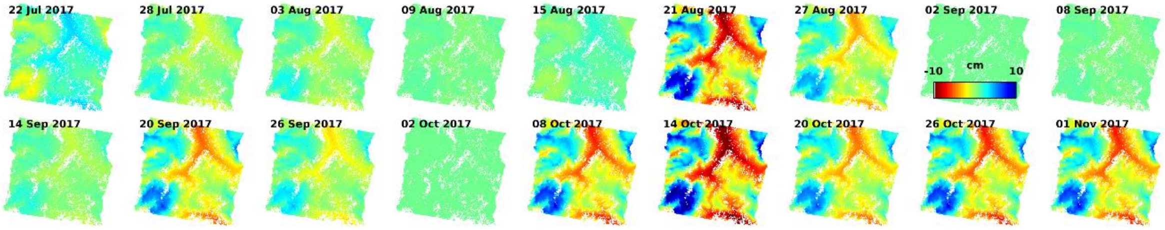

Figure 5.7: Interferometric tropospheric delay estimated based on the linear relation between phase and topography.

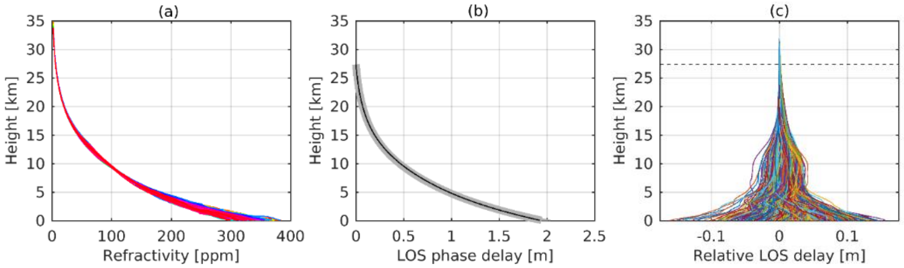

Figure 5.8: Tropospheric-related phase delay parameters computed by the balloon-sounding data for 18 days (00-12 UTC) from January 22 to November 1. (a) Refractivity (wet) component calculated based on (1). (b) LOS phase delay obtained by integrating refractivity (wet+dry) over the LOS signal path up to height of 27.2 km that the phase delay reaches to zero (the solid line refers to mean delay). (c) Relative LOS phase delay presents 400 combinations of the difference between tropospheric delays at two different days to estimate h_0 (dash line). All relative LOS delay converged to zero at height h_0= 27.2 km in which the standard deviations of relative delay are less than 0.05 cm. There is no relative delay between acquisitions above the dash-line (i.e., at 27.2 km).

In the spatial band selection step, a band of 8-9 km was selected as its correction presented the smallest rmse and mean rmse (i.e., 2 rad equals to 0.8cm) compared to the ERA5 phase delay to avoid contaminating tropospheric signal with the deformation signal (the landslide extent of 1.5×3 km) (Figure 5.9). The ERA5 was used here as the reference due to its high accuracy derived among other NWM models. After applying the 9th band (i.e., 8-9km), the tropospheric InSAR phase delay was estimated (Figure 5.10).

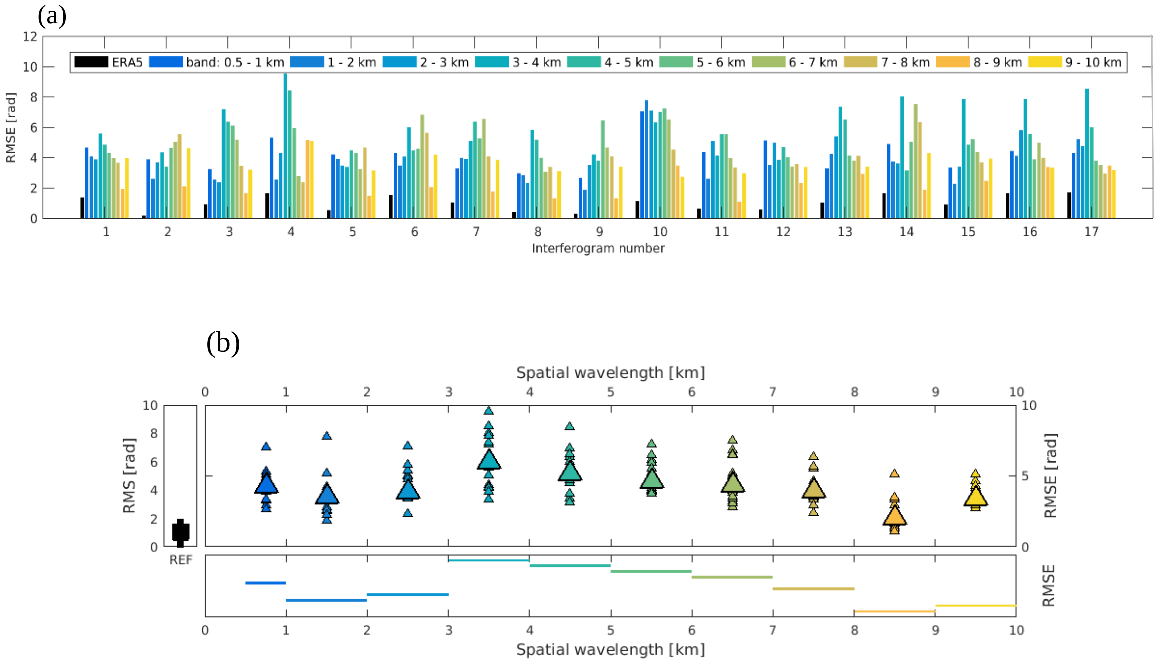

Figure 5.9: Spatial band filter selection for the power law model. (a) rmse of the different bands obtained from all interferograms and (b) mean rmse of the different spatial bands (on the bottom). The ERA5 phase delays were used to calculate the rmse as reference.

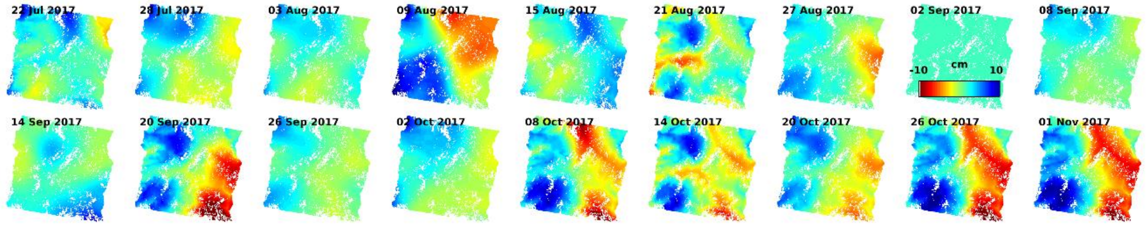

Figure 5.10: Interferometric tropospheric phase delay derived by using the power law model.

The estimated InSAR tropospheric delay maps obtained by power law do not show a good agreement with the other models. This means that the weather parameters used from sounding data do not reflect the real atmospheric conditions over the case study. The reason is probably be related to the distance between balloon-sounding station and our case study (nearly 100km apart). Hence, the power low parameters (i.e., α and h_0) have been updated by estimating the refractivity using the ERA5 model instead.

In order to assess the performance of the models used in InSAR tropospheric correction, we generated the velocity maps of the study area before and after tropospheric correction of the entire scene of the local area (i.e., the landslide extent) (Figure 5.11 and Figure 5.12). According to the velocity maps, some areas especially the residential region (which could considered at approximately zero velocity) in the valley (the blue λ-like-shape region in Figure 2.1b) are completely contaminated by tropospheric artifacts (‘V’ and ‘V-do’ in Figure 5.11). After the tropospheric correction, the velocity values in the aforementioned valley appeared as green color referring to zero displacement. The velocity maps can be visually categorized into three groups in terms of the patterns similarity: 1) ERA-Interim, ERA5 and MERRA2, 2) WRF, GACOS and Linear and 3) power law. To quantify the performance of each model in presence of the known deforming values (determined by the GPS measurements) the velocity map of the Corvara landslide before and after tropospheric correction was investigated. To this end, a magnified view of the velocity map of the Corvara landslide is provided in Figure 5.12.

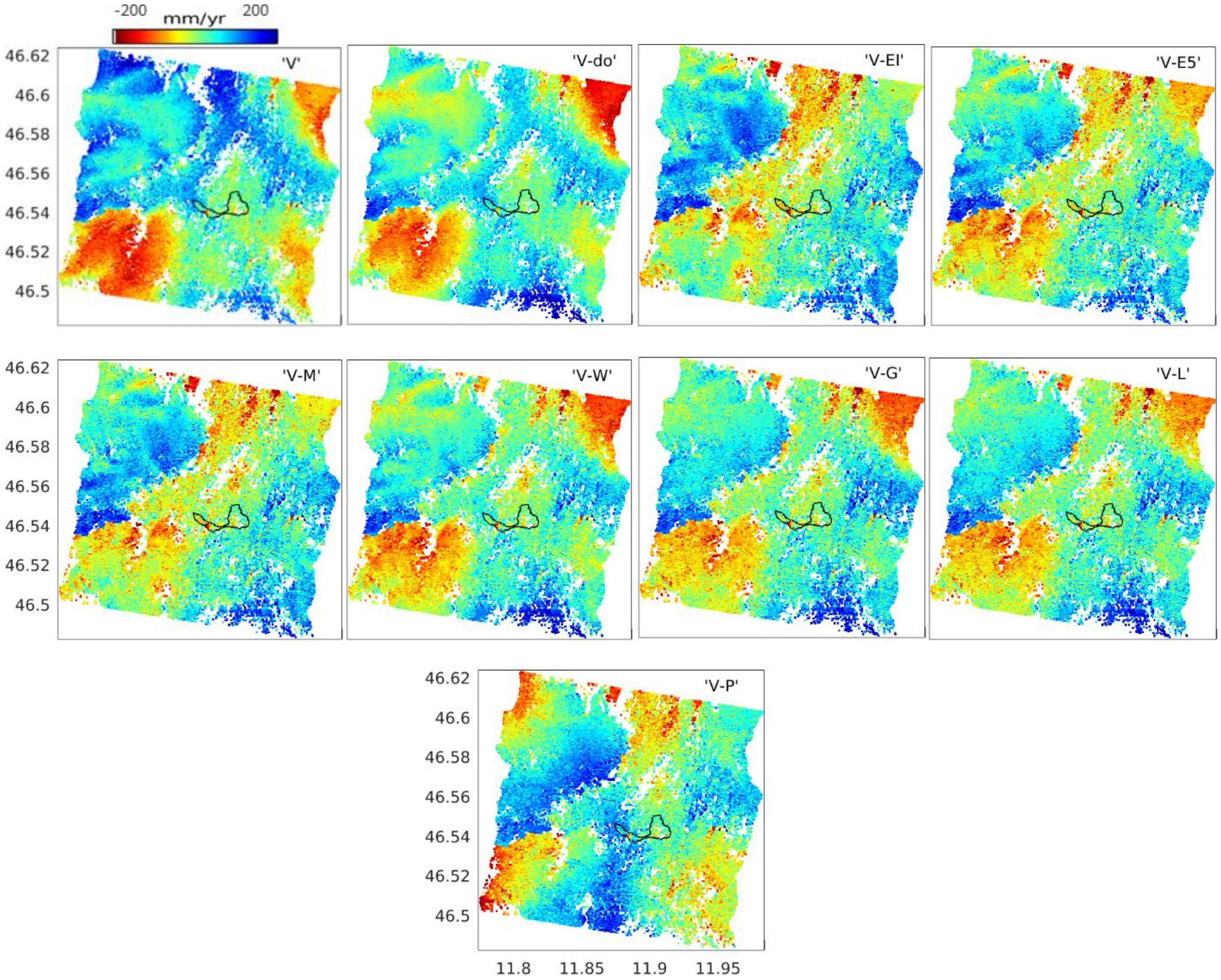

Figure 5.11: Mean LOS Velocity (MLV) maps. The acronyms in the Figs. indicate MLV without tropospheric correction (‘V’), after DEM error and orbital ramp removal (‘V-do’), after tropospheric correction using Entrim-I (‘V-EI’), ERA5 (‘V-E5’), GACOS (‘V-G’), MERRA2 (‘V-M’), WRF (‘V-W’), power law (‘V-P’) and linear (‘V-L’). Negative values refers to a movement away from the satellite and positive values indicate a motion toward the satellite. The black shape in the middle of the scene indicates the Corvara landslide location.

To assess the performance of each model the velocities of two GPS stations (i.e., no. 8 and 54) were compared with the corresponding points in the velocity map of the landslide after tropospheric correction within the same time span (see Figure 5.12).

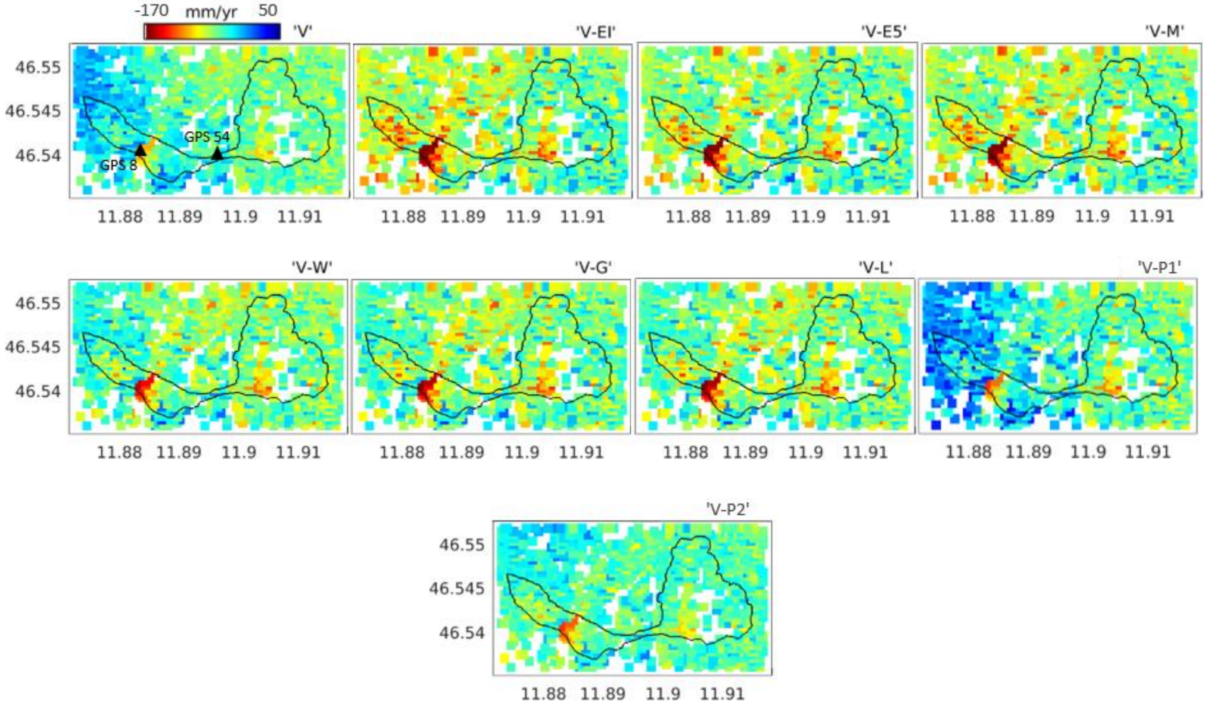

Figure 5.12: Velocity maps before ('V') and after tropospheric correction ('V-Models) for Corvara landslide. Power law parameters in 'V-P1' were approximated by the sounding data and their parameters were updated by the ERA5 model and the power law re-estimated ('V-P2'). The black triangles present the GPS stations in the first Fig.

The main movement direction of the landslide derived by GPS observations in Figure 2.1d can be compared with the movement direction obtained by InSAR in the velocity maps. For instance, the left part of landslide leading to the urban area that must have a near zero velocity (green color) can be used as a visual indicator to evaluate the models performance. In this respect, ERA5, MERRA2 and ERA-Interim indicate the highest agreement with a near zero velocity corresponding the urban area. Since the movement direction of GPS no. 58 is aligned to North-to-South (which is not detectable by the SAR imaging systems), this GPS station was excluded from our validation procedure. The velocity map corrected by the power law (‘V-P1’) presents a relative high disagreement with respect to the other models. Thereby, its parameters were updated using the ERA5 model in (2.26) and the velocity map recreated (‘V-P2’). A significant improvement was obtained especially in the left part of the velocity map. The quantitative values for GPS velocity and the corresponding values in the velocity maps for all the tropospheric correction models are presented in the Table 5.2.

The error values in the 0 show that ERA5 has the lowest error among all models for both GPS stations. The errors values for GPS no. 8 are generally smaller than for GPS no. 54 for all models. This is most probably due to a velocity underestimation caused in the non-LOS motion region corresponding to the GPS station no. 54 (see Figure 2.1).

5.5 Discussion

Although the NWM data generally suffer from a coarse spatial and temporal resolution, a relative good agreement exists between GPS-derived ZTD, ZWD and ZHD and their counterparts obtained by NWM models (Figure 5.3). In the case of ZTD parameter, GACOS and ERA5 exhibited the highest accuracy and precision among other NWMs. The GACOS yielded better accuracy (rmse=0.8 cm) than ERA5 (rmse=1 cm), but ERA5 provided better precision and higher correlation (std=2.7 cm and R=0.97) than GACOS (std=2.8 cm and R=0.95). To have a proper judgment about the GACOS and ERA5 performance, it is required that those have been computed with the same processing parameters. The most important parameter is the reference height (i.e., h) in (2.20), because the refractivity is computed up to that elevation. We set the reference height of 30 km in refractivity processing, but we do not know what reference height has been used in GACOS product. In the case of HTD and WTD parameters, ERA5, ERA-Interim, MERRA2 and WRF provided the highest accuracy, precision and correlation, respectively (see Figure 5.2).
In the estimation of total InSAR phase delay, which refers to temporal changes of refractivity rather than total refractivity (Figure 5.3), ERA5 with an accuracy and correlation of 0.9 cm and 0.97, respectively, and MERRA2 with a precision of 3.1 cm provided the best performance among other NWM models in comparison with GPS measurements (see Figure 5.4).

In order to discover the cause of the different results in ZTD and InSAR-TD estimations among NWM models (which could be potentially attributed to quality and spatio-temporal of the NWM models), the data quality investigation procedure should be performed for all NWM models. To this end, the weather parameters of the NWM models, which were used to estimate the refractivity, should be individually investigated. Temperature (which is the common variable in both hydrostatic and wet components of refractivity) and water vapor as a function of temperature and relative humidity were assessed and compared using (2.19). For instance, Figure 5.13 shows temperature and water vapor of ERA5 model obtained for the lower and upper part of the atmosphere. The lower atmosphere refers to the first pressure level (equal to the height of 205 m) and the upper atmosphere indicates the 37th pressure level (equal to the height of 40700 m). For the temperature parameter, at the upper atmosphere a regular smooth and homogeneous changes from -21° to -9° can be observed (Figure 5.13a), while an irregular sudden and heterogeneous changes from 6° to 35° can be seen at the lower atmosphere (Figure 5.13b). The water vapor presented the same temperature-like pattern for the lower and upper atmosphere

(Figure 5.13c and d). The water vapor estimated using two parameters: 1) water vapor pressure (svp) and 2) relative humidity. The svp calculation is based on the svp for water [145] and svp for ice [146]. Comparison of weather parameter values shows that the most of the delays on InSAR phase mainly occurs at the lower part of troposphere, where the tropospheric dynamics is intensely and frequently variable.

Comparison of the temperature parameter values of the NWM models pointed outed several significant items. The ERA-I and ERA5 exhibited a similar pattern with a difference in spatial resolution at all pressure levels while the temperature patterns of WRF and MERRA2 provided more discrepancy compared to ERA-I and ERA5 (Figure 5.14). ERA-I and ERA5 contained the NaN-pixels-free data, whereas WRF and MERRA2 contained the NaN pixels data at several pressure levels. The number of NaN-pixels in MERRA2 model decreases from pressure level 1 toward pressure level 10 and the pressure levels from 10 to 42 data show lack of NaN-pixels. In WRF, the data mostly contained the NaN-pixels, especially from pressure level 1 to 10 (even in some cases completely NaN-pixels data), the pressure levels between 10 and 27 did not content NaN-pixels and at the pressure levels between 27 and 37 NaN-pixels were observed to some extent randomly (Figure 5.14).

Since interpolation was used to fill out the NaN-pixels, the interpolated pixels increased the uncertainty and impaired the refractivity estimation. This fact indicates the reason for which WRF generally provided a lower accuracy and precision results with respect to other NWM models (Figure 5.3Figure 5.4). Departing from GPS data cross-validation, we utilized two metrics as performance indicators to evaluate the models performance: 1) comparison between phase std of the original interferograms (IFGs) and corrected IFGs using the models (i.e., reduction rate of the IFG phase std), and 2) correlation between IFGs phase and InSAR estimated tropospheric delay. Figure 5.15 depicts the phase std of all IFGs before and after phase correction and NWM-based models including wet, hydrostatic and total delays. The phase std reduction was then calculated for all models and IFGs (Figure 5.15).

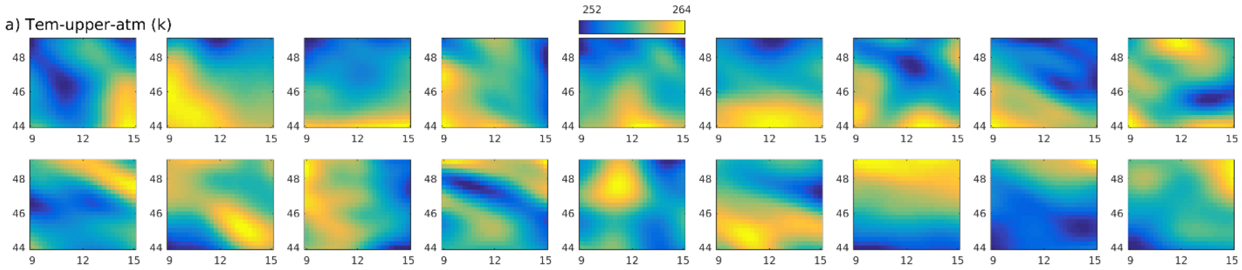

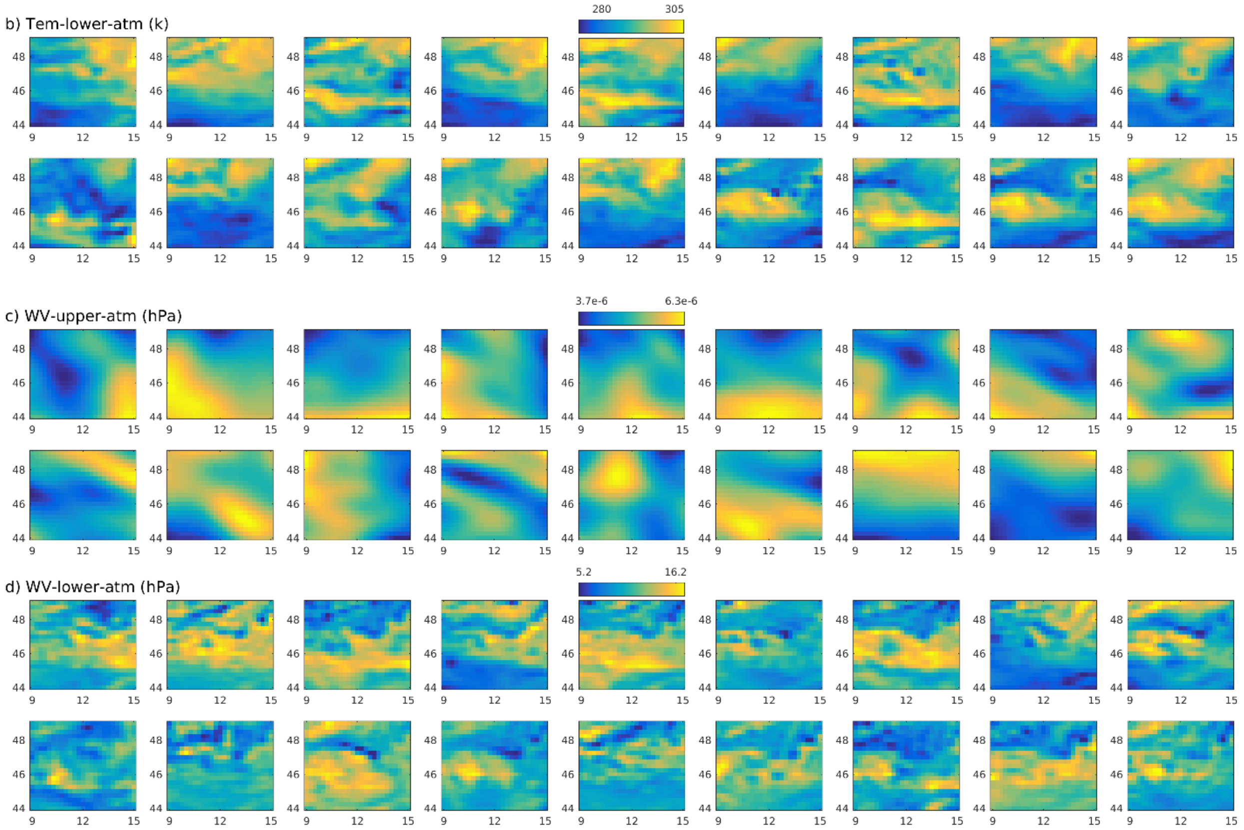

Figure 5.13: The Temperature (T) and Water Vapor (WV) of the ERA5 model. The T and WV parameters corresponding to the extent of each interferogram presented for the lower and upper atmosphere.

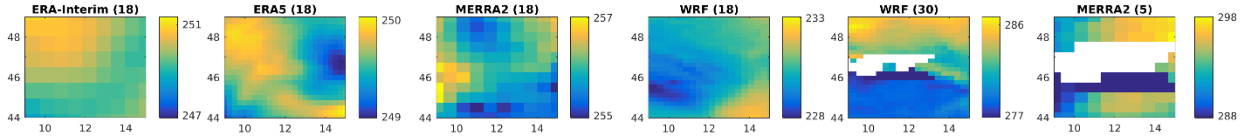

Figure 5.14: Data quality check of the NWM models. Temperature parameter is shown for four NWM models at 18th pressure level (7300 m), WRF at 30th pressure level (23000 m) and MERRA2 at 30th pressure level (1000 m). The white regions in WRF and MERRA2 data are shown the NaN-pixels.

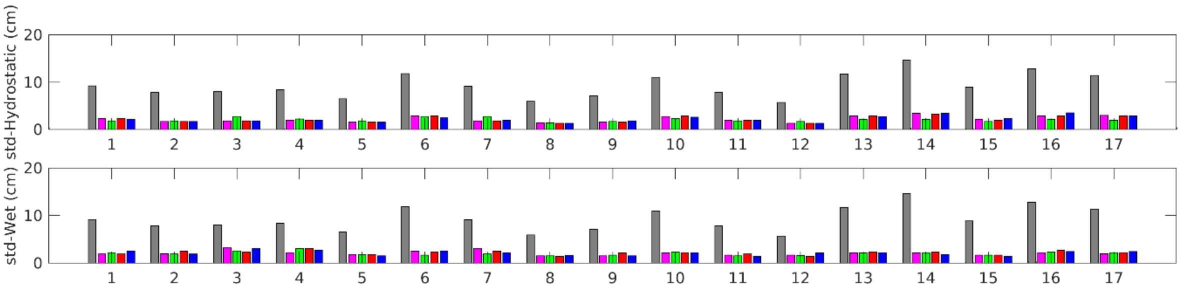

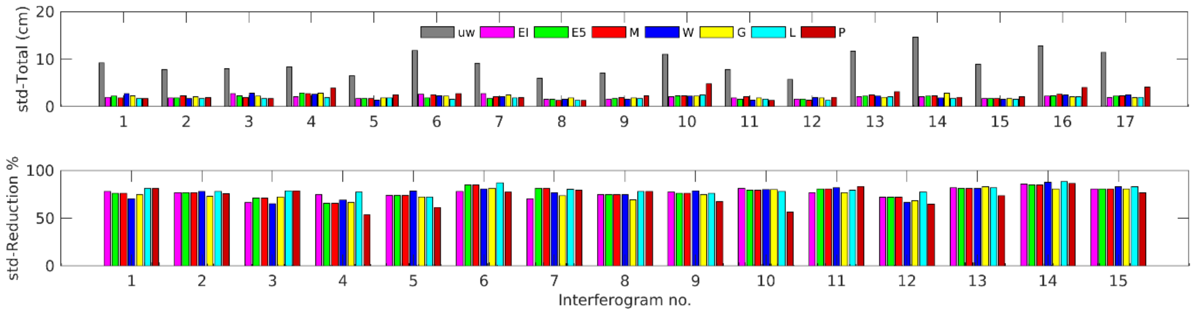

Figure 5.15: The phase standard deviation reduction of wet, hydrostatic and total components after InSAR tropospheric correction for 17 IFGs. In the legend, UW indicates the unwrapped interferograms and the rest refers to the models used in tropospheric correction.

The quantitative values of total phase std reduction for all IFGs are presented in Table 5.22. As the Table shows, ERA5 with 77.7% and linear with 80.2% presented the highest phase std reduction for the phase and NWM-based models, respectively. The phase std reduction results generally agrees with the results of the velocity values presented in Table II except for the linear case.

Table 5.2: Units for Magnetic Properties Velocity cross validation using GPS stations as references points (on the left side of the black solid line). Phase standard deviation reduction (on the right side of the black solid line).

GPS&Models	GPS 8	%Error 8	GPS 54	%Error 54	T-std red. (%)	Models
V_GPS	-155	-	-53	-	77.3	ERA-I
Vel	-113	27	-4	92.4	77.7	ERA5
V_EI	-144	7	-36	32	76.2	GACOS
V_E5	-148	4.5	-41	22.6	76.9	MERRA2
V_M	-145	6.4	-38	28.3	77.1	WRF
V_W	-138	10.9	-31	41.5	80.2	Linear
V_G	-143	7.7	-35	33.9	72.4	Power law
V_L	-143	7.7	-35	33.9	-	-
V_Pl 1	-133	14.1	-23	56.6	-	-
V_Pl 2	-135	12.9	-33	47.1	-	-

Line Of Sight (LOS) Velocity derived by GPS (V_GPS), Velocity before tropospheric correction (Vel) and velocity after tropospheric correction with the phase and NWM -based models (V_Models) corresponding to the GPS stations no. 8 and 54 are provided. The absolute percent error was calculated for all cases. The values were rounded and the unit is in millimeter per year (mm/yr). Total phase standard deviation reduction (T-std red.) of 17 unwrapped IFGs derived after tropospheric correction indicated for the phase and NWM-based models.

The correlation (R) between IFGs Phase and InSAR estimated tropospheric delay is presented in Figure 5.16 as the second metrics of the performance indicator. The correlation values demonstrate how successful each intended model was in capturing tropospheric changes. MERRA2 with correlation of 0.88 and ERA5 with correlation of 0.86 provided the highest correlation coefficients among other models, corresponding to 76.9% and 77.7% in terms of phase std reduction, respectively. Considering the indicator, linear model did not present a high correction whereas for the first indicator it provides the maximum phase std reduction. This fact implies that a single performance indicator is not able to reflect fully the performance of a model in tropospheric corrections. Therefore, the performance of models should be evaluated through several indicator metrics simultaneously.

Generally, the cross-validation results (see Figure 2.1) and two indicator metrics show that ERA5 relatively outperformed other models. ERA5 has the highest temporal resolution among all the NWM models (i.e., hourly), but its spatial resolution ranks in the third place after WRF and HRES-ECMWF (GACOS) (as shown in Table 5.1). As a result, the higher performance of ERA5 implies that the role of temporal variation in tropospheric constituent has more effect on phase delay estimation than the spatial resolution. Since a NWM model with a low temporal resolution has to be interpolated (due to the difference in acquisition time between NWM model and SAR data), hence, this leads to increase uncertainty. EAR5 with the hourly resolution could effectively reduce the uncertainty and increase the accuracy and precision of phase delay estimation.

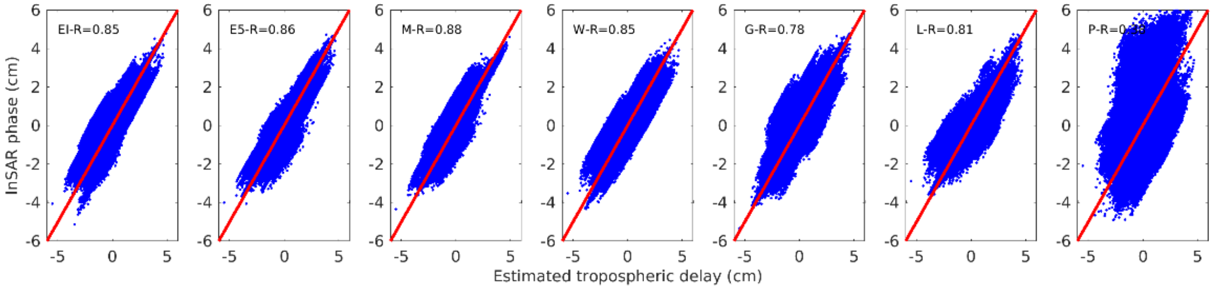

Figure 5.16: Estimated tropospheric delay and elevation versus InSAR phase (unwrapped interferogram). The red line is the 1:1 line.

5.6 Conclusion

In this thesis, we investigated the performance of two main common models in InSAR and ZTD tropospheric correction including phase-based (i.e., linear and power law) and NWM-based (Era-Interim, ERA5, MERA2 and WRF) models. We used GACOS product and GPS data as references to validate the results. The GPS-ZTD cross-validation showed that ERA5 and GACOS have the highest precision (std=2.7cm) and accuracy (rmse=0.8cm) among other NWM models, respectively. The GPS-InSAR cross-validation pointed out that ERA5 and MERRA2 have the highest accuracy (std=0.9cm) and precision (rmse=3.1cm) respectively. In addition to that, two indicators metrics, phase std reduction and correlation between phase and InSAR estimated tropospheric delay, were used to determine the performance and robustness of each model. Both indicators confirmed that ERA5 generally and relatively outperformed other models.

6. CONCLUSION

The complex nature of Corvara landslide displacements (i.e. N-S and E-W direction), which are partially along of LOS, covered with dense vegetation and contaminated by atmospheric artifacts have made difficult to investigate by conventional InSAR techniques. In addition, lack of enough natural permanent scaterers on the landslide is another main obstacle to use advanced DInSAR technique such as PSI. In such circumstance, taking a synergistic hybrid approach (i.e. integration of PSI, SBAS, MAI and OT results) and mitigating the atmospheric artifacts using phase and NW models allow us to produce an accurate displacement map of the Corvara landslide.

The experimental results of chapter 3 leads us to draw the conclusion that the feature-based matching algorithms outperformed the area-based matching ones, which are usually used for offset estimation in the SAR data domain (e.g., corner reflectors). The modularity of the feature-based algorithms allows us to combine each of corner and blob-based feature detection functions and descriptors. The combination of different algorithms in a hybrid technique leads to benefits from the capability of a given detector/descriptor (e.g., high localization accuracy of SURF descriptor), to compensate the weakness of other one (e.g., less localization accuracy of BRISK descriptor) or vice versa. Upon inspecting the results, the provided survey on the offset tracking techniques shows that a single all-purpose algorithm to be able to extract offsets in all situations does not exist. Each of the different approaches has relative advantages and drawbacks, dependent on data properties, features and application. In summary, although the InSAR-based techniques could provide more precise results, in cases of low coherence, high velocity rate and non-LOS movement they are not applicable. In these conditions, the area and feature-based matching techniques could be used as a robust alternative candidate for offset estimation.

The experimental results of chapter 4 provides the conclusion that 2D PhU yielded results closer to the ground truth measurements (GNSS) and the standard 2D unwrapping with a coherence threshold of 0.35 leads to fewer pixels but to a more reliable pixel selection. The RMSE values indicated a low accuracy in several points and SBAS results affected by the several possible error sources, leading to an overall underestimation and a failure to detect fast moving areas. The main error sources including GPS-related error, non-LOS displacements and atmospheric artifacts led to propagate considerable the errors in our results. The correction of the tilted GPS antenna (due to the landslide movements) will decrease the measurement error and lead to a reduction in RMSE between GPS and SBAS result. In addition to that, using sophisticated atmospheric correction techniques allow us to have more an accurate SBAS results. Finally, the use of Sentinel-A/B will considerably mitigate the negative effect of temporal decorrelation, due to the shorter revisit time of the data acquisition, which manifested itself in the mean coherence value at the end part of the connection graph.

From the experimental results of chapter 5 we can conclude that the high temporal resolution of ERA5 (hourly) seems the main reason for this good performance. The data quality check procedure demonstrated that NaN-pixels in MERRA2 and WRF models, induced a large bias in tropospheric refractivity estimation especially in the WRF model. In the phase-based models part, the linear model presented a higher performance than power law (non-linear model) in both indicators. Although re-estimation of power law parameters using ERA5 data improved the power law's performance, the proper spatial band selection is still a main challenge. In summary, the results illustrate that no single model and indicator metrics are able to fully estimate the phase delay and evaluate the performance model properly. Therefore, a combination of different data/models and the use of a set of indicator metrics should be considered simultaneously.

6.1 Future developments

The latest generations of the high-resolution SAR sensors, such as the ones on board TerraSAR-X and COSMOSkyMed, open interesting perspectives to test and develop more accurate offset tracking methods. Spatial resolutions close to 1 meter can allow detecting more features and to obtain more precise offset measurement. Therefore, the possibility to exploit this data should be investigated for either testing the current techniques and/or developing news one for specific types of land coverage accordingly.

The possibility of acquiring data with different incidence angles and geometry modes (i.e., ascending and descending) may allow us to decrease uncertainty caused by only LOS movement detection in complex cases such the Corvara landslide. Thus, the generation of 3D displacement map using different satellite modes should be addressed.

The Copernicus Sentinel-1A/B mission provides SAR acquisitions with the same configuration over large areas with high temporal and good spatial resolutions. This new generation of satellites, providing open-data products has enhanced the capabilities for continuously studying Earth surface changes especially in-vegetated areas. The short revisit time of Sentinel-1A/B data acquisition (i.e., 6 days since October 2017) provides a promising opportunity to mitigate the temporal decorrelation especially for SBAS technique. Installation of the C-band CR for the Sentinel-1A/B data enable us to use PSI in vegetated natural terrain.

The high potential of new generation of the numerical weather data with a high spatial and temporal resolution should be investigated to develop more robust InSAR atmospheric correction methods. The high quality of weather parameters of the recent numerical weather data is fundamental to develop more accurate physical-based models to estimate InSAR phase delay especially by using a hybrid approach.

New invariant feature and descriptor matching algorithms based on either phase or intensity information of SAR data should be developed for different applications to be resisted against various kind of geometrical distortions and speckle presence in SAR data.

The development of new L-band SAR sensors (e.g. SAOCOM-1A launched in October 2018), could be useful for interferometric applications to vegetated area as the landslides, due to lower sensitivity respect to decorrelation in case of signal with higher wavelength.

List of Publications

International peer-reviewed journals

1. M. Darvishi, R. Schlögel, L. Bruzzone, and G. Cuozzo, "Integration of PSI, MAI, and intensity-based sub-pixel offset tracking results for landslide monitoring with X-band corner reflectors-Italian Alps (Corvara)," *Remote Sens.*, vol. 10, no. 3, 2018.

2. M. Darvishi *et al.*, "Sentinel-1 and Ground-Based Sensors for Continuous Monitoring of the Corvara Landslide (South Tyrol, Italy)," *Remote Sens.*, vol. 10, no. 11, p. 1781, 2018.

3. M. Darvishi, G. Cuozzo, L. Bruzzone, F. Nilfouroushan, "Performance evaluation of phase and weather-based models in atmospheric correction with Sentinel-1data: Corvara landslide in the Alps," *IEEE Journal of Selected Topics in Applied Earth Observations and Remote Sensing*, 2018. (under review)

International peer-reviewed conferences

1. M. Darvishi *et al.*, "3D reconstruction of a large landslide from UAV-based imagery," *IEEE Young Professional Conference in Remote Sensing*, Oberpfaffenhofen (DLR), Germany, 2016.

2. R. Schlögel, B. Thiebes, I. Toschi, T. Zieher, M. Darvishi, and C. Kofler, "Sensor Data Integration for Landslide Monitoring---the LEMONADE Concept," in *Advancing Culture of Living with Landslides: Volume 2 Advances in Landslide Science*, M. Mikos, B. Tiwari, Y. Yin, and K. Sassa, Eds. Cham: Springer International Publishing, 2017, pp. 71–78.

Bibliography

[1] D. Petley, “Global patterns of loss of life from landslides,” *Geology*, vol. 40, no. 10, pp. 927–930, Aug. 2012.

[2] F. Guzzetti and others, “Landslide hazard and risk assessment,” Universitäts-und Landesbibliothek Bonn, 2006.

[3] F. Guzzetti, A. C. Mondini, M. Cardinali, F. Fiorucci, M. Santangelo, and K.-T. Chang, “Landslide inventory maps: {New} tools for an old problem,” *Earth-Science Rev.*, vol. 112, no. 1–2, pp. 42–66, Apr. 2012.

[4] C. J. Van Westen and R. Soeters, “Landslide hazard and risk zonation — why is it still so difficult ?,” pp. 167–184, 2006.

[5] V. De Novellis, R. Castaldo, P. Lollino, M. Manunta, and P. Tizzani, “Advanced three-dimensional finite element modeling of a slow landslide through the exploitation of DInSAR measurements and in situ surveys,” *Remote Sens.*, vol. 8, no. 8, 2016.

[6] F. Calò *et al.*, “Remote Sensing of Environment Enhanced landslide investigations through advanced DInSAR techniques : The Ivancich case study , Assisi , Italy,” *Remote Sens. Environ.*, vol. 142, pp. 69–82, 2014.

[7] C. Tolomei, A. Taramelli, M. Moro, M. Saroli, D. Aringoli, and S. Salvi, “Analysis of the deep-seated gravitational slope deformations over Mt. Frascare (Central Italy) with geomorphological assessment and DInSAR approaches,” *Geomorphology*, vol. 201, pp. 281–292, 2013.

[8] C. E. Rodríguez, J. J. Bommer, and R. J. Chandler, “Earthquake-induced landslides: 1980-1997,” *Soil Dyn. Earthq. Eng.*, vol. 18, no. 5, pp. 325–346, 1999.

[9] R. Torres *et al.*, “GMES Sentinel-1 mission,” *Remote Sens. Environ.*, vol. 120, pp. 9–24, 2012.

[10] A. Rucci, A. Ferretti, A. Monti-Guarnieri, and F. Rocca, “Sentinel 1 SAR interferometry applications: the outlook for sub millimeter measurements,” *Remote Sens. Environ.*, vol. 120, pp. 156–163, May 2012.

[11] K. Dai *et al.*, “Monitoring activity at the Daguangbao mega-landslide (China) using Sentinel-1 TOPS time series interferometry,” *Remote Sens. Environ.*, vol. 186, pp. 501–513, 2016.

[12] M. Manunta *et al.*, “Unsupervised parallel SBAS-DInSAR chain for massive and systematic Sentinel-1 data processing,” *Int. Geosci. Remote Sens. Symp.*, vol. 2016-Novem, pp. 3890–3893, 2016.

[13] C. De Luca *et al.*, “Automatic and Systematic Sentinel-1 SBAS-DInSAR Processing Chain for Deformation Time-series Generation,” *Procedia Comput. Sci.*, vol. 100, pp. 1176–1180, 2016.

[14] R. Tomás *et al.*, “Radar interferometry techniques for the study of ground subsidence phenomena: A review of practical issues through cases in Spain,” *Environ. Earth Sci.*, vol. 71, no. 1, 2014.

[15] R. F. Hanssen, *Radar interferometry: data interpretation and error analysis*, vol. 2. Springer Science & Business Media, 2001.

[16] D. C. Ghiglia and M. D. Pritt, *Two-dimensional phase unwrapping: theory, algorithms, and*

software, vol. 4. Wiley New York, 1998.

[17] H. Zebker, P. Rosen, and S. Hensley, “Atmospheric effects in interferometric synthetic aperture radar surface deformation and topographic maps,” *J. Geophys. …*, vol. 102, pp. 7547–7563, 1997.

[18] T. Wright, B. Parsons, and E. Fielding, “Measurement of interseismic strain accumulation across the North Anatolian Fault by satellite radar interferometry,” *Geophys. Res. Lett.*, vol. 28, no. 10, pp. 2117–2120, 2001.

[19] T. J. Wright, B. Parsons, P. C. England, and E. J. Fielding, “InSAR observations of low slip rates on the major faults of western Tibet,” *Science (80-.).*, vol. 305, no. 5681, pp. 236–239, 2004.

[20] A. Ferreti, C. Prati, and F. Rocca, “Nonlinear subsidence rate estimation using permanent scatterers in differential SAR interferometry,” *IEEE Trans. Geosci. Remote Sens.*, vol. 38, no. 5, pp. 2202–2212, 2000.

[21] B. M. Kampes, *Radar Interferometry*, vol. 12. 2006.

[22] P. Berardino, G. Fornaro, R. Lanari, and E. Sansosti, “A new algorithm for surface deformation monitoring based on small baseline differential SAR interferograms,” *IEEE Trans. Geosci. Remote Sens.*, vol. 40, no. 11, pp. 2375–2383, Nov. 2002.

[23] O. Mora, J. J. Mallorqui, and A. Broquetas, “Linear and nonlinear terrain deformation maps from a reduced set of interferometric SAR images,” *IEEE Trans. Geosci. Remote Sens.*, vol. 41, no. 10, pp. 2243–2253, 2003.

[24] A. Hooper, “A multi-temporal InSAR method incorporating both persistent scatterer and small baseline approaches,” *Geophys. Res. Lett.*, vol. 35, no. 16, p. L16302, Aug. 2008.

[25] S. Liu, “Satellite radar interferometry: estimation of atmospheric delay,” TU Delft, Delft University of Technology, 2012.

[26] J. A. Richards, *Remote Sensing with Imaging Radar*. Berlin, Heidelberg: Springer Berlin Heidelberg, 2009.

[27] H. A. Zebker and J. Villasenor, “Decorrelation in interferometric radar echoes,” *IEEE Trans. Geosci. Remote Sens.*, vol. 30, no. 5, pp. 950–959, 1992.

[28] A. Ferretti, C. Prati, and F. Rocca, “Permanent scatterers in SAR interferometry,” vol. 39, no. 1, pp. 8–20, 2001.

[29] A. J. Hooper, “Persistent Scatterer Radar Interferometry For Crustal Deformation Studies and Modeling of Volcanic deformation,” *Dep. Geophys.*, vol. Ph.D., no. May, p. 124, 2006.

[30] C. Colesanti, A. Ferretti, R. Locatelli, and G. Savio, “Multi-platform permanent scatterers analysis: first results,” in *2003 2nd GRSS/ISPRS Joint Workshop on Remote Sensing and Data Fusion over Urban Areas*, 2003, pp. 52–56.

[31] R. E. Huschke and others, “Glossary of meteorology,” 1959.

[32] R. Goldstein, “Atmospheric limitations to repeat-track radar interferometry,” *Geophys. Res. Lett.*, vol. 22, no. 18, pp. 2517–2520, 1995.

[33] D. Massonnet and K. L. Feigl, “Radar interferometry and its application to changes in the Earth’s surface,” *RMassonnet, D., K. L. Feigl. 1998. Radar Interferom. its Appl. to Chang.*

Earth's surface. Rev. Geophys. 36 441. doi10.1029/97RG03139.eviews Geophys., vol. 36, no. 4, p. 441, 1998.

[34] J. Saastamoinen, "Introduction to practical computation of astronomical refraction," *Bull. Géodésique*, vol. 106, no. 1, pp. 383–397, 1972.

[35] M. Bevis, S. Businger, T. A. Herring, C. Rocken, R. A. Anthes, and R. H. Ware, "Remote Sensing of Atmospheric Water Vapor Using The Global Positioning System," *J. Geophys. Res.*, vol. 97, no. D14, p. 15.

[36] F. Beauducel, P. Briole, and J.-L. Froger, "Volcano-wide fringes in ERS synthetic aperture radar interferograms of Etna (1992-1998): Deformation or tropospheric effect?," *J. Geophys. Res. Solid Earth*, vol. 105, no. B7, pp. 16391–16402, 2000.

[37] R. Jolivet, R. Grandin, C. Lasserre, M. P. Doin, and G. Peltzer, "Systematic InSAR tropospheric phase delay corrections from global meteorological reanalysis data," *Geophys. Res. Lett.*, vol. 38, no. 17, pp. 1–6, 2011.

[38] Z. Li, E. J. Fielding, P. Cross, and R. Preusker, "Advanced InSAR atmospheric correction: MERIS/MODIS combination and stacked water vapour models," *Int. J. Remote Sens.*, vol. 30, no. 13, pp. 3343–3363.

[39] Z. Li, J.-P. Muller, P. Cross, and E. J. Fielding, "Interferometric synthetic aperture radar (InSAR) atmospheric correction: GPS, Moderate Resolution Imaging Spectroradiometer (MODIS), and InSAR integration," *J. Geophys. Res. Solid Earth*, vol. 110, no. B3, 2005.

[40] E. K. Smith and S. Weintraub, "The Constants in the Equation for Atmospheric Refractive Index at Radio Frequencies," *Proc. IRE*, vol. 41, no. 8, pp. 1035–1037, 1953.

[41] M. P. Doin, C. Lasserre, G. Peltzer, O. Cavalié, and C. Doubre, "Corrections of stratified tropospheric delays in SAR interferometry: Validation with global atmospheric models," *J. Appl. Geophys.*, vol. 69, no. 1, pp. 35–50, 2009.

[42] C. W. Wicks, D. Dzurisin, S. Ingebritsen, W. Thatcher, Z. Lu, and J. Iverson, "Magmatic activity beneath the quiescent Three Sisters volcanic center, central Oregon Cascade Range, USA," *Geophys. Res. Lett.*, vol. 29, no. 7, pp. 2–5, 2002.

[43] D. P. S. Bekaert, A. Hooper, and T. J. Wright, "A spatially variable power law tropospheric correction technique for InSAR data," *J. Geophys. Res. Solid Earth*, vol. 120, no. 2, pp. 1345–1356, 2015.

[44] D. P. S. Bekaert, A. Hooper, and T. J. Wright, "Journal of Geophysical Research : Solid Earth Reassessing the 2006 Guerrero slow-slip event , Mexico :," *J. Geophys. Res. B Solid Earth*, pp. 1357–1375, 2015.

[45] R. Jolivet *et al.*, "Improving InSAR geodesy using Global Atmospheric Models," *J. Geophys. Res. Solid Earth*, vol. 119, no. 3, pp. 2324–2341, 2014.

[46] C. Yu, Z. Li, and N. T. Penna, "Interferometric synthetic aperture radar atmospheric correction using a GPS-based iterative tropospheric decomposition model," *Remote Sens. Environ.*, vol. 204, no. March 2017, pp. 109–121, 2018.

[47] D. P. S. Bekaert, R. J. Walters, T. J. Wright, A. J. Hooper, and D. J. Parker, "Statistical comparison of InSAR tropospheric correction techniques," *Remote Sens. Environ.*, vol. 170, pp. 40–47, 2015.

[48] J. Jung, D. J. Kim, and S. E. Park, “Correction of atmospheric phase screen in time series InSAR using WRF model for monitoring volcanic activities,” *IEEE Trans. Geosci. Remote Sens.*, vol. 52, no. 5, pp. 2678–2689, 2014.

[49] Z. W. Li *et al.*, “Correcting atmospheric effects on InSAR with MERIS water vapour data and elevation-dependent interpolation model,” *Geophys. J. Int.*, vol. 189, no. 2, pp. 898–910, 2012.

[50] S. Williams, Y. Bock, P. Fang, and H. Cecil, “Aperture Radar Products,” *Network*, no. 98, pp. 51–67, 1998.

[51] P. W. Webley, R. M. Bingley, A. H. Dodson, G. Wadge, S. J. Waugh, and I. N. James, “Atmospheric water vapour correction to InSAR surface motion measurements on mountains: Results from a dense GPS network on Mount Etna,” *Phys. Chem. Earth*, vol. 27, no. 4–5, pp. 363–370, 2002.

[52] F. Onn and H. A. Zebker, “Correction for interferometric synthetic aperture radar atmospheric phase artifacts using time series of zenith wet delay observations from a GPS network,” *J. Geophys. Res. Solid Earth*, vol. 111, no. 9, pp. 1–16, 2006.

[53] Y. N. N. Lin, M. Simons, E. A. Hetland, P. Muse, and C. Dicaprio, “A multiscale approach to estimating topographically correlated propagation delays in radar interferograms,” *Geochemistry, Geophys. Geosystems*, vol. 11, no. 9, pp. 1–17, 2010.

[54] J. R. Elliott, J. Biggs, B. Parsons, and T. J. Wright, “InSAR slip rate determination on the Altyn Tagh Fault, northern Tibet, in the presence of topographically correlated atmospheric delays,” *Geophys. Res. Lett.*, vol. 35, no. 12, pp. 1–5, 2008.

[55] B.-C. Gao and Y. J. Kaufman, “Water vapor retrievals using Moderate Resolution Imaging Spectroradiometer (MODIS) near-infrared channels,” *J. Geophys. Res. Atmos.*, vol. 108, no. D13, p. n/a-n/a, 2003.

[56] Z. Li, J.-P. Muller, and P. Cross, “Comparison of precipitable water vapor derived from radiosonde, GPS, and Moderate-Resolution Imaging Spectroradiometer measurements,” *J. Geophys. Res. Atmos.*, vol. 108, no. D20, 2003.

[57] S. N. Madsen, H. A. Zebker, and J. Martin, “Topographic mapping using radar interferometry: processing techniques,” *IEEE Trans. Geosci. Remote Sens.*, vol. 31, no. 1, pp. 246–256, Jan. 1993.

[58] R. Scheiber and A. Moreira, “Coregistration of interferometric SAR images using spectral diversity,” *IEEE Trans. Geosci. Remote Sens.*, vol. 38, no. 5 I, pp. 2179–2191, 2000.

[59] J. G. Van Oostveen, “Optimized Extraction of InSAR derived Along-Track Deformation during Glacial Surges - towards a better understanding of the Dyngjujökull glacier in surge state,” *Delft Univ. Technol.*, no. January, p. 137, 2014.

[60] R. Bamler and M. Eineder, “Split band interferometry versus absolute ranging with wideband SAR systems,” *IGARSS 2004. 2004 IEEE Int. Geosci. Remote Sens. Symp.*, vol. 2, no. C, pp. 980–984, 2004.

[61] N. B. D. Bechor and H. A. Zebker, “Measuring two-dimensional movements using a single InSAR pair,” *Geophys. Res. Lett.*, vol. 33, no. 16, pp. 1–5, 2006.

[62] H. S. Jung and W. J. Lee, “An improvement of the performance of multiple aperture SAR,” *IEEE Trans. Geosci. Remote Sens.*, vol. 53, no. 9, pp. 4952–4960, 2015.

[63] H. S. Jung, J. S. Won, and S. W. Kim, “An improvement of the performance of multiple-aperture SAR interferometry (MAI),” *IEEE Trans. Geosci. Remote Sens.*, vol. 47, no. 8, pp. 2859–2869, 2009.

[64] R. Bamler, “Interferometric stereo radargrammetry: absolute height determination from ERS-ENVISAT interferograms,” *IGARSS 2000. IEEE 2000 Int. Geosci. Remote Sens. Symp. Tak. Pulse Planet Role Remote Sens. Manag. Environ. Proc. (Cat. No.00CH37120)*, vol. 2, pp. 742–745, 2000.

[65] R. Bamler and M. Eineder, “Accuracy of differential shift estimation by correlation and split-bandwidth interferometry for wideband and Delta-k SAR systems,” *IEEE Geosci. Remote Sens. Lett.*, vol. 2, no. 2, pp. 151–155, 2005.

[66] F. De Zan, “Accuracy of incoherent speckle tracking for circular gaussian signals,” *IEEE Geosci. Remote Sens. Lett.*, vol. 11, no. 1, pp. 264–267, 2014.

[67] N. Roma, J. Santos-Victor, and J. Tomé, “A Comparative Analysis of Cross-Correlation Matching Algorithms Using a Pyramidal Resolution Approach,” *Empirical Evaluation Methods in Computer Vision*. pp. 117–142, 2012.

[68] E. Grossman and J. Santos-Victor, “Performance Evaluation of Optical Flow Estimators: Assessment of a New Affine Flow Method,” *Rob. Auton. Syst.*, vol. 21, no. 1, pp. 69–82, 1997.

[69] A. J. H. Hii, C. E. Hann, J. G. Chase, and E. E. W. Van Houten, “Fast normalized cross correlation for motion tracking using basis functions,” *Comput. Methods Programs Biomed.*, vol. 82, no. 2, pp. 144–156, 2006.

[70] C. D. Kuglin, “The phase correlation image alignment methed,” in *Proc. Int. Conference Cybernetics Society*, 1975, pp. 163–165.

[71] N. Van Puymbroeck, R. Michel, R. Binet, J.-P. Avouac, and J. Taboury, “Measuring earthquakes from optical satellite images,” *Appl. Opt.*, vol. 39, no. 20, pp. 3486–3494, 2000.

[72] M. J. F. Martínez, E. G. Merino, E. G. Sánchez, J. E. G. Sánchez, A. M. Del Rey, and G. R. Sánchez, “Advances in Microbial Ecology,” *Lect. Notes Comput. Sci. (including Subser. Lect. Notes Artif. Intell. Lect. Notes Bioinformatics)*, vol. 7629, no. PART 1, pp. 458–468, 2013.

[73] S. Leprince, S. Barbot, F. Ayoub, and J. P. Avouac, “Automatic, Precise, Ortho-rectification and Coregistration for satellite Image Correlation, Application to Ground Deformation Measurement,” *IEEE J. Geosci. Rem. Sens.*, vol. 45, no. 6, pp. 1529–1558, 2007.

[74] A. J. Fitch, A. Kadyrov, W. J. Christmas, and J. Kittler, “Orientation Correlation,” *Procedings Br. Mach. Vis. Conf. 2002*, pp. 133–142, 2002.

[75] S. Leutenegger, M. Chli, and R. Y. Siegwart, “BRISK: Binary Robust invariant scalable keypoints,” in *2011 International Conference on Computer Vision*, 2011, pp. 2548–2555.

[76] J. Shi and C. Tomasi, “Good features to track,” in *1994 Proceedings of IEEE Conference on Computer Vision and Pattern Recognition*, 1994, pp. 593–600.

[77] J. Shi and C. Tomasi, “Good features to track,” 1993.

[78] M. Ó. Fríl, E. Jones, M. Glavin, and C. Hughes, “Comparison of Feature Detection Methods for an Automotive Camera System,” *Nucleus*, no. 1, 2007.

[79] C. Harris and M. Stephens, “A Combined Corner and Edge Detector,” *Procedings Alvey Vis. Conf. 1988*, pp. 23.1-23.6, 1988.

[80] A. Alahi, R. Ortiz, and P. Vandergheynst, “FREAK: Fast retina keypoint,” *Proc. IEEE Comput. Soc. Conf. Comput. Vis. Pattern Recognit.*, pp. 510–517, 2012.

[81] E. Rosten and T. Drummond, “Fusing points and lines for high performance tracking,” *Proc. IEEE Int. Conf. Comput. Vis.*, vol. II, pp. 1508–1515, 2005.

[82] E. Rosten and T. Drummond, “Machine learning for high-speed corner detection,” *Lect. Notes Comput. Sci. (including Subser. Lect. Notes Artif. Intell. Lect. Notes Bioinformatics)*, vol. 3951 LNCS, pp. 430–443, 2006.

[83] H. Bay, T. Tuytelaars, and L. Van Gool, “SURF: Speeded up robust features,” *Lect. Notes Comput. Sci. (including Subser. Lect. Notes Artif. Intell. Lect. Notes Bioinformatics)*, vol. 3951 LNCS, pp. 404–417, 2006.

[84] C. Werner *et al.*, “Complimentary measurement of geophysical deformation using repeat-pass SAR,” *Proc. Geosci. Remote Sens. Symp. IGARSS ’01*, vol. 00, no. C, pp. 3255–3258, 2001.

[85] I. Biederman, “Visual Object Recognition,” *An Invit. to Cogn. Sci. 2nd Ed.*, pp. 121–165, 1995.

[86] S. Keypoints and D. G. Lowe, “Distinctive Image Features from,” *Int. J. Comput. Vis.*, vol. 60, no. 2, pp. 91–110, 2004.

[87] F. Dellinger, J. Delon, Y. Gousseau, J. Michel, and F. Tupin, “SAR-SIFT : A SIFT-Like Algorithm for SAR Images,” vol. 53, no. 1, pp. 453–466, 2015.

[88] W. Ma, Z. Wen, Y. Wu, L. Jiao, and S. Member, “Remote Sensing Image Registration With Modified SIFT and Enhanced FeatureMatching,” *IEEE Geosci. Remote Sens. Lett.*, vol. 14, no. 1, pp. 3–7, 2017.

[89] A. Corsini, A. Pasuto, and M. Soldati, “Geomorphological investigation and management of the Corvara landslide (Dolomites, Italy),” *JGU Trans.*, vol. 20, no. 3, pp. 169–186, 1999.

[90] R. Schlögel *et al.*, “Multi-Temporal X-Band Radar Interferometry Using Corner Reflectors: Application and Validation at the Corvara Landslide (Dolomites, Italy),” *Remote Sens.*, vol. 9, no. 7, p. 739, 2017.

[91] S. Sterlacchini, S. Frigerio, P. Giacomelli, and M. Brambilla, “Landslide risk analysis: A multi-disciplinary methodological approach,” *Nat. Hazards Earth Syst. Sci.*, vol. 7, no. 6, pp. 657–675, 2007.

[92] A. Corsini, A. Pasuto, M. Soldati, and A. Zannoni, “Field monitoring of the Corvara landslide (Dolomites, Italy) and its relevance for hazard assessment,” *Geomorphology*, vol. 66, no. 1–4, pp. 149–165, Mar. 2005.

[93] B. Thiebes, E. Tomelleri, A. Mejia-aguilar, R. Schlögel, and M. Darvishi, “UAV-based landslide deformation monitoring – first results from Corvara landslide,” 2016, vol. 18, no. January, p. 12115.

[94] R. Schlögel, B. Thiebes, I. Toschi, T. Zieher, M. Darvishi, and C. Kofler, “Sensor Data Integration for Landslide Monitoring---the LEMONADE Concept,” in *Advancing Culture of Living with Landslides: Volume 2 Advances in Landslide Science*, M. Mikos, B. Tiwari, Y. Yin, and K. Sassa, Eds. Cham: Springer International Publishing, 2017, pp. 71–78.

[95] F. Bovenga, A. Refice, and G. Pasquariello, “Corner reflector deployment for X-band SAR interferometry to monitor the landslide of Carlantino, Daunia Region (Italy),” in *EGU General Assembly Conference Abstracts*, 2012.

[96] C. Colesanti, A. Ferretti, C. Prati, and F. Rocca, “Monitoring landslides and tectonic motions with the Permanent Scatterers Technique,” *Eng. Geol.*, vol. 68, no. 1–2, pp. 3–14, 2003.

[97] D. Massonnet and K. L. Feigl, “Radar interferometry and its application to changes in the Earth’s surface,” *Rev. Geophys.*, vol. 36, no. 4, pp. 441–500, 1998.

[98] U. Spagnolini, “2-D phase unwrapping and instantaneous frequency estimation,” *IEEE Trans. Geosci. Remote Sens.*, vol. 33, no. 3, 1995.

[99] SARMAP, “SARScape: Technical description.,” Switzerland, 2012.

[100] A. Messerli and A. Grinsted, “Image georectification and feature tracking toolbox: ImGRAFT,” *Geosci. Instrumentation, Methods Data Syst.*, vol. 4, no. 1, pp. 23–34, 2015.

[101] F. Ayoub, S. Leprince, and J. P. Avouac, “Co-registration and correlation of aerial photographs for ground deformation measurements,” *ISPRS J. Photogramm. Remote Sens.*, vol. 64, no. 6, pp. 551–560, 2009.

[102] A. Kääb and M. Vollmer, “Surface geometry, thickness change and flow fields on creeping mountain permafrost: Automatic extraction by digital image analysis,” *Permafr. Periglac. Process.*, vol. 11, no. August, pp. 315–326, 2000.

[103] T. Heid and A. Kääb, “Evaluation of existing image matching methods for deriving glacier surface displacements globally from optical satellite imagery,” *Remote Sens. Environ.*, vol. 118, pp. 339–355, 2012.

[104] MATLAB*, version 9.1.0 (R2016b)*. Natick, Massachusetts: The MathWorks Inc., 2016.

[105] A. Ferretti, C. Prati, F. Rocca, and I. Politecnico, “Permanent scatterers in SAR interferometry,” *Geosci. Remote Sensing, IEEE Trans.*, vol. 39, no. 1, pp. 1528–1530, 1999.

[106] A. Hooper, P. Segall, and H. Zebker, “Persistent scatterer interferometric synthetic aperture radar for crustal deformation analysis, with application to Volcán Alcedo, Galápagos,” *J. Geophys. Res. Solid Earth*, vol. 112, no. 7, pp. 1–21, 2007.

[107] M. a Fischler and R. C. Bolles, “Random sample consensus: a paradigm for model fitting with applications to image analysis and automated cartography,” *Commun. ACM*, vol. 24, no. 6, pp. 381–395, Jun. 1981.

[108] N. Adam, B. Kampes, and M. Eineder, “Development of a scientific permanent scatterer system: Modifications for mixed ERS/ENVISAT time series,” *Eur. Sp. Agency, (Special Publl. ESA SP*, no. 572, pp. 457–465, 2005.

[109] A. Freeman, “Sar Calibration: An Overview,” *IEEE Trans. Geosci. Remote Sens.*, vol. 30, no. 6, pp. 1107–1121, 1992.

[110] P. Marinkovic, G. Ketelaar, F. Van Leijen, and R. Hanssen, “InSAR quality control: Analysis of five years of corner reflector time series,” *Eur. Sp. Agency, (Special Publ. ESA SP*, no. 649 SP, 2008.

[111] F. J. Van Leijen, *Persistent Scatterer Interferometry based on geodetic estimation theory*. 2014.

[112] H. S. Jung, W. J. Lee, and L. Zhang, “Theoretical accuracy of along-track displacement measurements from multiple-aperture interferometry (MAI),” *Sensors (Switzerland)*, vol. 14, no. 9, pp. 17703–17724, 2014.

[113] J. P. (Industrial L. & M. Lewis, “Fast Normalized Cross-Correlation Template Matching by

Cross-," *Vis. Interface*, vol. 1995, no. 1, pp. 1–7, 1995.

[114] M. Debella-Gilo and A. Kääb, "Sub-pixel precision image matching for measuring surface displacements on mass movements using normalized cross-correlation," *Remote Sens. Environ.*, vol. 115, no. 1, pp. 130–142, 2011.

[115] N. Hanaizumi and S. Fujimur, "An automated method for registration of satellite remote sensing images," in *Geoscience and Remote Sensing Symposium, 1993. IGARSS '93. Better Understanding of Earth Environment., International*, 1993, pp. 1348–1350 vol.3.

[116] R. Berthilsson, "Affine correlation," in *Proceedings. Fourteenth International Conference on Pattern Recognition (Cat. No.98EX170)*, 1998, vol. 2, pp. 1458–1460 vol.2.

[117] A. Simper, "Correcting general band-to-band misregistrations," in *Proceedings of 3rd IEEE International Conference on Image Processing*, 1996, vol. 1, pp. 597–600 vol.2.

[118] K. Mikolajczyk, K. Mikolajczyk, C. Schmid, and C. Schmid, "A performance evaluation of local descriptors," *IEEE Trans. Pattern Anal. Mach. Intell.*, vol. 27, no. 10, pp. 1615–1630, 2005.

[119] J. Heinly, E. Dunn, and J. M. Frahm, "Comparative evaluation of binary features," *Lect. Notes Comput. Sci. (including Subser. Lect. Notes Artif. Intell. Lect. Notes Bioinformatics)*, vol. 7573 LNCS, no. PART 2, pp. 759–773, 2012.

[120] O. Faugeras, P. Fua, and B. Hotz, "Quantitative and qualitative comparison of some area and feature based stereo algorithms," *W. F orstner St …*, vol. 2502, pp. 0–21, 1992.

[121] R. Krishnan and A. R. Anil, "A Survey On Image Matching Methods," vol. 2, no. 1, pp. 58–61, 2016.

[122] T. Tuytelaars and K. Mikolajczyk, "Local Invariant Feature Detectors: A Survey," *Found. Trends® Comput. Graph. Vis.*, vol. 3, no. 3, pp. 177–280, 2007.

[123] A. Ferretti, C. Prati, and F. Rocca, "No Title," *IEEE Trans. Geosci. Remote Sens.*, vol. 39, no. null, p. 8, 2001.

[124] C. Prati, A. Ferretti, and D. Perissin, "Recent advances on surface ground deformation measurement by means of repeated space-borne SAR observations," *J. Geodyn.*, vol. 49, no. 3, pp. 161–170, 2010.

[125] J. Wasowski and F. Bovenga, "Investigating landslides and unstable slopes with satellite Multi Temporal Interferometry : Current issues and future perspectives," *Eng. Geol.*, vol. 174, pp. 103–138, 2014.

[126] C. Colesanti and J. Wasowski, "Investigating landslides with space-borne Synthetic Aperture Radar (SAR) interferometry," *Eng. Geol.*, vol. 88, no. 3–4, pp. 173–199, 2006.

[127] A. Pepe, L. D. Euillades, M. Manunta, and R. Lanari, "New advances of the extended minimum cost flow phase unwrapping algorithm for SBAS-DInSAR analysis at full spatial resolution," *IEEE Trans. Geosci. Remote Sens.*, vol. 49, no. 10 PART 2, pp. 4062–4079, 2011.

[128] R. M. Goldstein, H. A. Zebker, and C. L. Werner, "Satellite radar interferometry: Two-dimensional phase unwrapping," *Radio Sci.*, vol. 23, no. 4, pp. 713–720, 1988.

[129] C. W. Chen and H. A. Zebker, "Two-dimensional phase unwrapping with use of statistical models for cost functions in nonlinear optimization," *JOSA A*, vol. 18, no. 2, pp. 338–351, 2001.

[130] D. C. Ghiglia and L. A. Romero, "Direct phase estimation from phase differences using fast

elliptic partial differential equation solvers," *Opt. Lett.*, vol. 14, no. 20, pp. 1107–1109, 1989.

[131] F. W. David, "A guide to The analysis and display of spatial data." Pregamon, 1992.

[132] N. Cressie, *Statistics for spatial data*. John Wiley & Sons, 2015.

[133] H. Moritz, "Advanced physical geodesy," *Adv. Planet. Geol.*, 1980.

[134] M. Komac, R. Holley, P. Mahapatra, H. van der Marel, and M. Bavec, "Coupling of GPS/GNSS and radar interferometric data for a 3D surface displacement monitoring of landslides," *Landslides*, vol. 12, no. 2, pp. 241–257, 2015.

[135] G. Lollino *et al.*, *Engineering geology for society and territory – Volume 6: Applied geology for major engineering projects*, no. JANUARY 2001. 2015.

[136] C. Xu, H. Wang, L. Ge, C. Yonezawa, and P. Cheng, "InSAR tropospheric delay mitigation by GPS observations: A case study in Tokyo area," *J. Atmos. Solar-Terrestrial Phys.*, vol. 68, no. 6, pp. 629–638, 2006.

[137] A. Hooper and H. A. Zebker, "Phase unwrapping in three dimensions with application to InSAR time series.," *J. Opt. Soc. Am.*, vol. 24, no. 9, pp. 2737–2747, 2007.

[138] M. Darvishi, R. Schlögel, L. Bruzzone, and G. Cuozzo, "Integration of PSI, MAI, and intensity-based sub-pixel offset tracking results for landslide monitoring with X-band corner reflectors-Italian Alps (Corvara)," *Remote Sens.*, vol. 10, no. 3, 2018.

[139] A. Hooper *et al.*, "Importance of horizontal seafloor motion on tsunami height for the 2011 Mw=9.0 Tohoku-Oki earthquake," *Earth Planet. Sci. Lett.*, vol. 361, pp. 469–479, 2013.

[140] G. Gomba, A. Parizzi, F. De Zan, M. Eineder, and R. Bamler, "Toward operational compensation of ionospheric effects in SAR interferograms: The split-spectrum method," *IEEE Trans. Geosci. Remote Sens.*, vol. 54, no. 3, pp. 1446–1461, 2016.

[141] A. Hooper, H. Zebker, P. Segall, and B. Kampes, "A new method for measuring deformation on volcanoes and other natural terrains using InSAR persistent scatterers," *Geophys. Res. Lett.*, vol. 31, no. 23, pp. 1–5, 2004.

[142] W. Shamarock *et al.*, "A description of the advanced research WRF version 3," *Tech. Rep.*, vol. 113, no. June, p. 113, 2008.

[143] T. . Herring, R. W. King, M. A. Floyd, and S. C. McClusky, "GAMIT Reference Manual. GPS Analysis at MIT GLOBK, Release 10.6," no. June, p. 168, 2015.

[144] J. Boehm, B. Werl, and H. Schuh, "Troposphere mapping functions for GPS and very long baseline interferometry from European Centre for Medium-Range Weather Forecasts operational analysis data," *J. Geophys. Res. Solid Earth*, vol. 111, no. 2, pp. 1–9, 2006.

[145] A. L. Buck, "New equations for computing vapor pressure and enhancement factor," *J. Appl. Meteorol.*, vol. 20, no. 12, pp. 1527–1532, 1981.

[146] O. A. Alduchov and R. E. Eskridge, "Improved Magnus form approximation of saturation vapor pressure," *J. Appl. Meteorol.*, vol. 35, no. 4, pp. 601–609, 1996.

[147] M. Darvishi *et al.*, "Sentinel-1 and Ground-Based Sensors for Continuous Monitoring of the Corvara Landslide (South Tyrol, Italy)," *Remote Sens.*, vol. 10, no. 11, p. 1781, 2018.

[148] F. Darvishi, Mehdi and Cuozzo, Giovanni and Bruzzone, Lorenzo and Nilfouroushan,

“Performance evaluation of phase and weather-based models in atmospheric correction with Sentinel-1data: Corvara landslide in the Alps,” *IEEE J. Sel. Top. Appl. Earth Obs. Remote Sens.*, 2018.